2023-09-25

Evaluation of Cold Spray Process for Solid-State Welding

Umer, Muhammad Zia ud din Urf

UNIVERSITY OF CALGARY

Evaluation of Cold Spray Process for Solid-State Welding

by

Muhammad Zia Ud Din Urf Umer

A THESIS

SUBMITTED TO THE FACULTY OF GRADUATE STUDIES

IN PARTIAL FULFILMENT OF THE REQUIREMENTS FOR THE

DEGREE OF MASTER OF SCIENCE

GRADUATE PROGRAM IN MECHANICAL ENGINEERING

CALGARY, ALBERTA

SEPTEMBER, 2023

Abstract

Welding is an important manufacturing process used in various industries, from automotive to aerospace. However, existing welding techniques have certain drawbacks that affect weld integrity and limit their use in joining some temperature-sensitive materials. A significant concern is the heat-affected zone (HAZ), which often becomes softer than its surrounding areas. To address this problem, the expansion of cold spray process—a solid-state layer-by-layer high speed particle deposition process—as an alternative solid-state welding technique is proposed, developed, and evaluated, a process referred to as cold spray welding (CSW).

As a starting point, the origin of softening in a Tungsten inert gas (TIG)-welded AA 6061-T651 plates is first comprehensively investigated using experimental, analytical, and thermodynamic modelling approaches; this is further compared with the CSWed samples to assess its (CSW) potential and current limitations for future optimization. The outcome of this study reveals that the softening effect or HAZ in the TIG-welded sample could extend up to ~40 mm from the weld center. The HAZ further partitions into four regions: HAZ1, HAZ2, HAZ3, and HAZ4, based on peak temperature, hardness, and stable precipitate phases in those regions. While the CSWed samples show several benefits: negligible microstructural alterations, inhibition of phase transformations, and suppression of deleterious HAZ, they exhibit lower tensile strength and impact toughness than TIG-welded counterpart due to the presence of ubiquitous microvoids resulting from inadequate metallurgical bonding in CSWed area. These microvoids act as initiation sites for microcracks. To guide future optimization efforts, a failure mechanism in the CSWed parts is established.

This research underscores the importance of addressing softening effects in welded materials, while also charting a new path to establishing a new unexplored solid-state welding technique that

has the potential to minimize the drawbacks in conventional welding methods. By understanding and overcoming the poor particle-particle/particle-substrate metallurgical bonding, CSW is poised to be an alternative greener solid-state welding technique for applications in various industries.

Preface

This thesis is an original work of the author, and it consists of four chapters. Two of them, Chapters 2 and 3, have already been submitted for publication in peer-reviewed journals; they contribute to the field of materials science and engineering—welding technology, specifically. Due to the adopted manuscript-based format for this thesis, these chapters are copies of submitted manuscripts. Chapter 2 focuses on the re-examination of the softening phenomenon in the fusion-based TIG welding process, and it is submitted for peer-review in a reputable materials science journal as;

> *Muhammad Zia ud din Urf Umer and Ahmed A. Tiamiyu, "X-ray microscopic and thermodynamic model assessments of softening in TIG welded AA 6061-T651," (Under review, first revision submitted).*

Chapter 3 mainly evaluates the cold spray process for solid-state welding, followed by a comparison with the conventional Tungsten inert gas (TIG) welding process and it is submitted for peer-review in a reputable materials science journal as;

> *Muhammad Zia ud din Urf Umer and Ahmed A. Tiamiyu "Evaluation of cold spray process for solid state welding," (Under review).*

It should be noted that there are some duplications of figures between the two manuscripts; specifically, they are Fig. 2.1 (a, b, c) and Fig. 3.1 (b, d, e); Fig. 2.3 (a, c) and Fig. 3.8; and Fig. 2.10 (b, d) and Fig. 3.11 (a, c).

Acknowledgements

I would like to express my utmost gratitude to my supervisor, Dr. Ahmed A. Tiamiyu, for providing me with insightful and encouraging guidance throughout this journey. I am truly grateful for the opportunity he granted me to delve into the fascinating field of metallurgy, welding, and cold spray. His kindness as a human being and his commitment to fostering a learning environment characterized by friendliness and respect have been truly inspiring.

I also extend my thanks to Dr. Gbenga Asala from Red River College, Manitoba, for his support in conducting the cold spray welding experiment and for his guidance throughout the process. I am also grateful for the assistance provided by the Maker Multiplex lab at the University of Calgary in machining the samples used in this thesis. Additionally, I am thankful to Dr. Benedikt Hallgrímsson and Mr. Wei Liu from the Hallgrimsson lab at the University of Calgary for their continuous support in the use of X-ray microscopy machine. I also acknowledge the financial support from the Ron Corle Graduate Scholarship in Pipeline Engineering.

I am grateful to all my teachers who have imparted valuable life lessons to me. Many thanks go to all members of the Material Performance and Processing (MaPP) lab, my classmates, seniors, and friends for their support throughout my journey.

I am deeply grateful to my parents, Muhammad Iqbal, and Saira Iqbal, for their kindness, love, and teachings that have shaped me into a better individual. I would also like to acknowledge my siblings: Afshan Iqbal, Sadaf Iqbal, Imama Iqbal, Zainulabdeen, Muhammed Moin ud din, and Rabia Iqbal. They deserve more praise than words can express. Their continuous support and love have been the driving force behind my progress.

Finally, I want to express my thanks to my beloved country, Pakistan, for providing me with all the resources and education necessary to become an educated individual and enter this program. It has facilitated my pursuit of knowledge and exploration of science.

Dedication

"In the Name of Allah, the most Gracious, the most Merciful"

Most surely in the creation of the heavens and the earth and the alternation of the night and the day, and the ships that run in the sea with that which profits men, and the water that Allah sends down from the cloud, then gives life with it to the earth after its death and spreads in it all (kinds of) animals, and the changing of the winds and the clouds made subservient between the heaven and the earth, there are signs for a people who understand.

(2:164)

And Allah has brought you forth from the wombs of your mothers – you did not know anything –and He gave you hearing and sight and hearts that you may give thanks.

(16:78)

(The Holy Quran)

Table of Contents

List of Tables

List of Figures

Chapter: 1 Introduction and Motivation

To avoid duplication, this chapter only covers relevant literature that is not addressed in the introduction section of Chapters 2 and 3. In addition, Chapter 1 includes the motivation behind this study, the overall and specific objectives of the work, thesis organization, and statement of contribution.

1.1 Background

In applications, where the joining of intricate parts is a major aspect of component design, e.g., oil and gas pipelines, and chemical processing plants under extreme conditions, safe and reliable joints are of utmost importance [1,2]. Welding—a fabrication process involving the fusion of two or more materials at their contacting surfaces—is considered the most dependable joining process for metals using heat, pressure, and chemical reactions, depending on the choice of the welding method [3]. The strength of welded components depends on strong metallurgical bonding between parts, which can be achieved through two main mechanisms: liquid (fusion welding) or diffusion (solid-state welding) [4]. While traditional fusion- and diffusion-based welding processes are widely adopted by industries, they do come with certain limitations that can sometimes restrict their use in some applications. In what follows, the traditional welding techniques and their limitations are outlined.

1.1.1 Traditional welding techniques and their limitations

1.1.1.1 Fusion Welding

The joining of components by fusion welding primarily involves melting the contact surfaces of the components using a suitable heat source [5]. Various fusion-based welding processes are

adopted by industries, such as Tungsten inert gas (TIG) welding, shielded metal arc welding, and gas metal arc welding. In TIG welding, as shown in Fig. 1.1a, a shielding gas is used to protect the

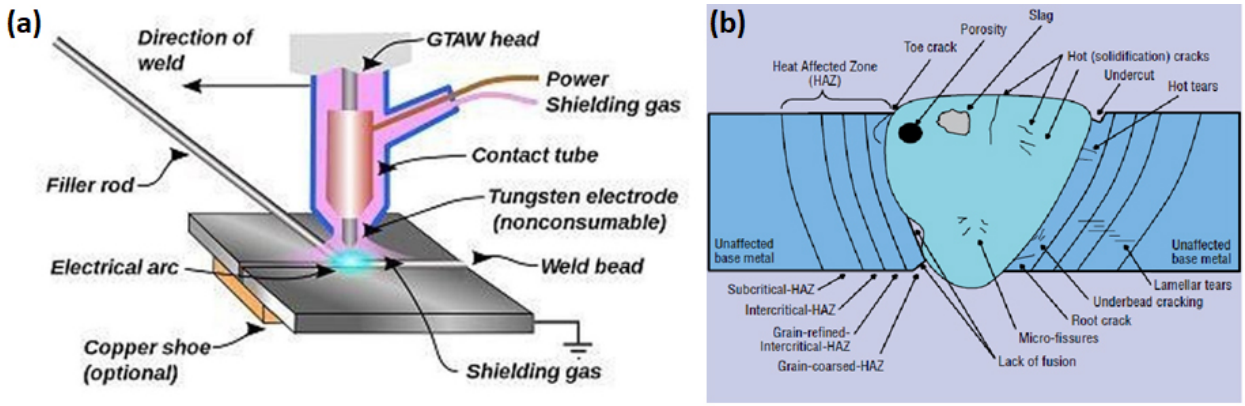

Figure 1.1: Schematics of (a) TIG welding process (reproduce from [6]), (b) common welding defects and different zones in welded components (reproduce from [7])

weld pool from atmospheric gases, a non-consumable tungsten electrode and a filler wire are used to fill the weld gap. However, if the shielding gas does not adequately cover the welding pool, it can lead to the formation of porosity due to interactions with atmospheric gases [8]. Some reported fusion welding defects are solidification cracking, shrinkage porosity, and grain coarsening [5,9], while others are shown in Fig. 1.1b. Moreover, a portion of the heat applied during fusion is dissipated into the surrounding base metal, resulting in the alteration of the microstructure and mechanical properties of the regions adjacent to the fusion boundary (this region is known as the Heat-Affected Zone—HAZ), and sometimes even the weld zone itself, as shown in Fig. 1.1b. The microstructural changes in the HAZ can lead to the deterioration of mechanical properties, either in the form of softening or hardening, depending on the dominant strengthening mechanism of the joined metal system [10,11]. Some highlighted limitations of fusion welding processes are listed below [4,5,12];

- Significant alteration of parent material properties; softening or embrittlement of base material due to high heat input.

- Distortion, residual stresses, and hot cracking, induced by the melting and solidification process.
- Difficulty in joining dissimilar materials.
- Use of combustible or fuel gases that produces harmful fumes.

Despite these limitations, fusion-based welding techniques offer advantages in terms of ease and speed of joint development compared to diffusion-based welding processes [5]. However, diffusion-based approaches become preferable when fusion-based processes are not feasible due to metallurgical incompatibility and significant differences in material physical properties [13].

1.1.1.2 Solid-state Welding

Solid-state welding processes primarily involve joining by the application of pressure and heat, using various mechanisms such as mechanical interlocking, extensive interfacial plastic deformation, diffusion, etc. [5]. Examples of solid-state welding processes include friction stir welding (FSW), ultrasonic welding, forge welding, etc. In FSW process (Fig. 1.2a), for example,

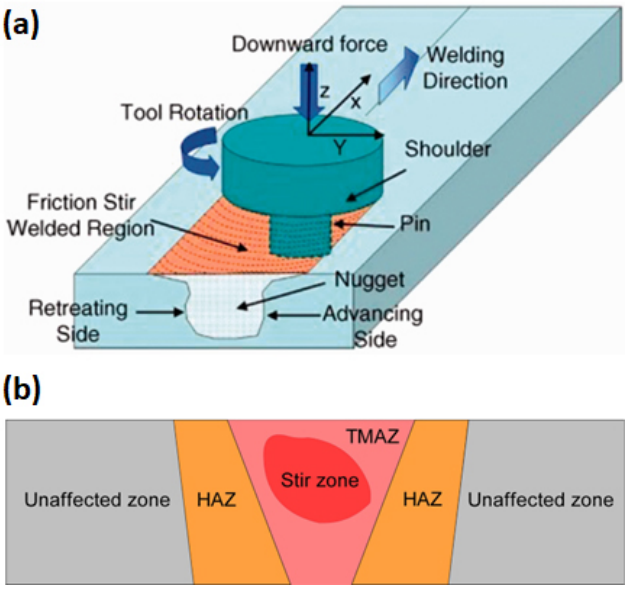

Figure 1.2: Schematic of (a) friction stir welding process (reproduce from [14]) and (b) different zones: stir zone (SZ), Thermo-mechanical affected zone (TMAZ), Heat affected zone (HAZ) and un-affected zone in the welded component (redrawn from [15]).

a non-consumable rotating tool with a specially designed pin and shoulder are inserted into the abutting edges of metal sheets or plates to be joined and traversed along the joint line [16].

During FSW, the non-consumable rotating tool generates frictional heat, leading to intense plastic deformation at elevated temperatures, and eventual development of a weld zone [17]. This results in the joining of materials, but it also causes microstructurally-different zones in the welded component as seen in Fig. 1.2b, similar to the observations in fusion welding processes (Fig. 1.1b). Some other notable limitations of solid-state welding processes are listed below [5,18];

- Applicable to only simple weld geometry.
- Requires expensive equipment and tooling.
- Slow, tedious, and time-consuming
- Requires a very high-quality surface finish.

There is a significant industrial need to develop a new welding process that addresses the limitations of both traditional welding methods. This thesis evaluates a cold spray process that has the potential to meet this need, and in what follows, the cold spray process is briefly reviewed.

1.2 Cold Spray Process

Cold spray (CS) process is a solid-state deposition process where micro-sized particles are accelerated to supersonic speed to adhere to the substrate [19]. Unlike other thermal spray processes, CS does not require high thermal input to melt the powder particles; this helps minimize or eliminate deleterious effects such as oxidation, distortion, residual stresses and phase transformation [20,21]. So far, CS has found application in *in-situ* crack repairs, tribological coatings, antibacterial coatings, and restoration/remanufacturing of engineering components

[22,23]. With the rapid progress of additive manufacturing (AM) technology, CS has also been extended to AM processes [24]. Unlike many fusion-based AM technologies that involve melting and may compromise the final product's properties due to high heat input, CS technology offers a potential solution to these challenges [25].

1.2.1 Cold Spray Set up and Types

In the CS process, high-velocity stream of microparticles is accelerated through a deLaval or converging/diverging nozzle by a compressed driving gas that is maintained at a temperature lower than the melting point of the sprayed particles (Fig. 1.3) [24,26].

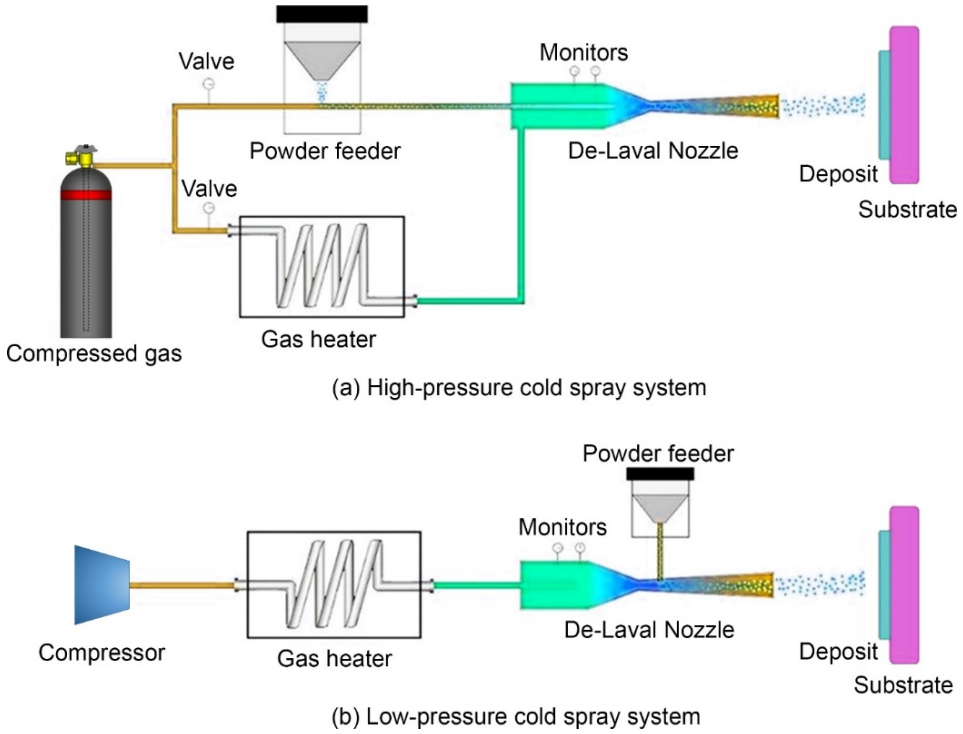

Figure 1.3: Schematic diagram of (a) high-pressure cold spray (HPCS) system, and (b) low-pressure cold spray (LPCS) system, adapted from [25].

The CS process can be categorized into two classes based on the driving gas pressure: High-pressure cold spray (HPCS) and low-pressure cold spray (LPCS) systems. In the HPCS system (Fig. 1.3a), the compressed gas is pressurized to levels greater than 1 MPa. On the other hand, the

LPCS system (Fig. 1.3b) is typically pressurized at levels lower than 1 MPa [27]. HPCS launches particles at velocities ranging from 800 to 1400 m/s, offering high impact and deposition capabilities, while LPCS is limited to particle velocities of 300 to 600 m/s and is suitable for depositing lighter materials [28].

1.2.2 Mechanisms of Bonding, Types of Bonding, and barriers to bonding

The quality of the CS deposit relies on the nature of bonding between particles and the particle-substrate [29]. The high-velocity impact of microparticles leads to large interfacial deformation and localized heat at impact sites [30]. Successful bonding requires a certain amount of impact kinetic energy, which sets on at or above a threshold velocity called the critical velocity (v_{cr}). If the impact velocity falls below v_{cr}, the particles will rebound without bonding. The properties of both the feedstock materials (e.g., oxidation, density, shape, size, and material) and the substrate (e.g., roughness, temperature, hardness, and material) can influence the onset of bonding [31]. Various processing parameters such as driving gas temperature and pressure, nozzle geometries, and powder feeding rate can be tuned to increase the particle impact velocity, and in turn, improve the bonding conditions at the particle-substrate and particle-particle interfaces [32].

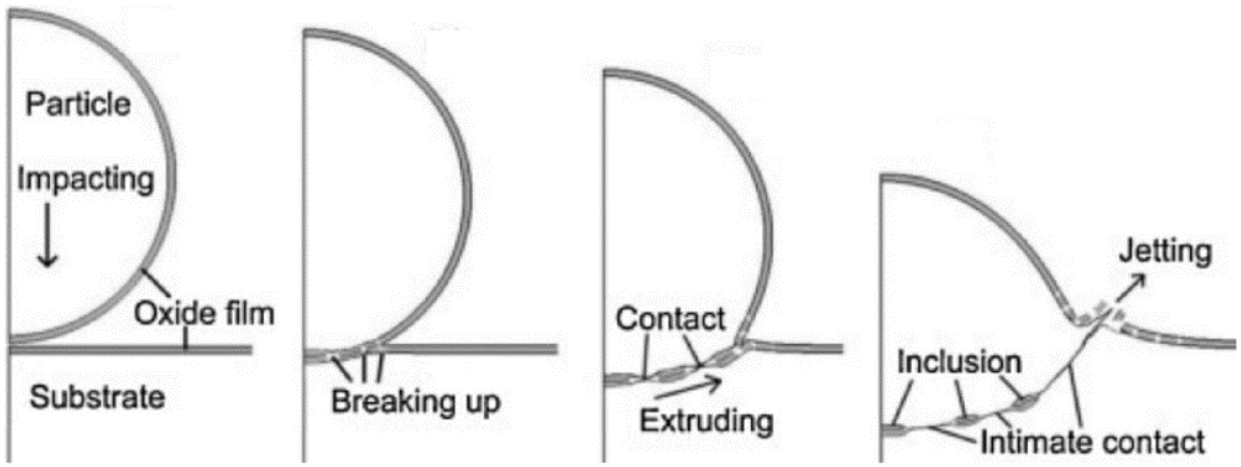

Figure 1.4: Deformation of particle upon impact, and the break-up of oxide films, reproduced from [33].

There are two types of bonding in CS: mechanical interlocking (physical) and metallurgical (chemical) bonding [31]. Mechanical interlocking occurs when particles anchor or embed into the substrate or previously-deposited particles without atomic interactions, while metallurgical bonding involves the establishment of metallic bonding due to chemical interaction at clean metal-to-metal contacts [27]. There are a few proposed mechanisms of metallurgical bonding in the literature [34,35]. The most referenced is the oxide break-up mechanism schematized in Fig. 1.4: as the particle impresses into the substrate, native surface oxides break up to initiate intimate metal-

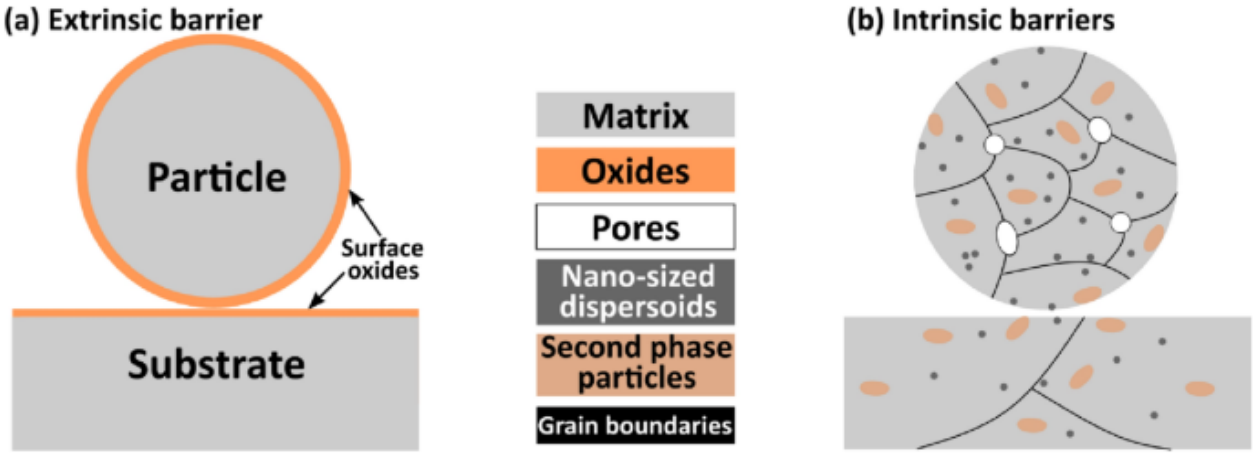

Figure 1.5: Schematic diagrams showing common (a) extrinsic and (b) intrinsic barriers to bonding during cold spray process, reproduced from [27].

metal contact between oxide islands, followed by their (oxides) expulsion out of the contacting interface in the form of *jetting* [36]. In addition to the oxide break up, oxide layer delamination has recently been reported as a dominant energy dissipation mechanism that occurs during this process [35]. Other non-oxide-related mechanisms have since been proposed, some of which include adiabatic shear instability, jetting—outward ejection of material from the particle–substrate interface [27], interfacial melting [37–39], and interface solid-state amorphization [40,41].

Regardless of the mechanism, a crucial requirement for bonding is that *a clean metal-to-metal contact* must be established [42]. As such, there are barriers to achieving these clean contacts, and the impact velocity/kinetic energy of the particles must be high enough to overcome these barriers. Adaan-Nyiak and Tiamiyu [27] classified the hindrance to metal-to-metal contact as *extrinsic* or *intrinsic* barriers. *Extrinsic barriers*, as illustrated in Fig. 1.5a, are external barriers such as surface oxides on contacting surfaces. These oxide layer act as geometrical constraints to extensive particle plasticity [23], increasing the energy required to initiate metal-to-metal contact, which in turn raises the v_{cr} [22]. On the other hand, Fig. 1.5b shows the *intrinsic barriers*, such as micropores, oxide dispersoids, and micron-sized second-phase particles. For instance, Davison et al. [43] observed that the presence of pores in microparticles requires additional energy for pore closure during particle impact process; this therefore, delays the onset of bonding. Both extrinsic and intrinsic barriers will impede the bonding process in CS, as the process-induced energy will first be used to overcome these barriers before metal-to-metal contact can be initiated.

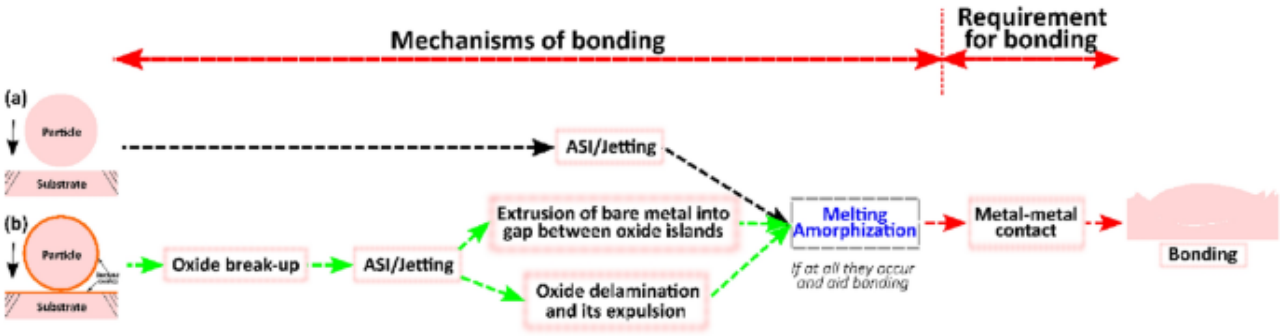

Figure 1.6: Possible sequence of the bonding mechanism in cold spray can be illustrated through two case samples: (a) without an oxide layer and (b) with a native oxide layer, reproduce from [27].

Fig. 1.6 provides an overview of the bonding mechanisms that can set on during CS process, whether or not the contacting surfaces are ladened with native surface oxides. In the oxide-free surface case (Fig. 1.6a), the process-induced kinetic energy is solely consumed by the jetting process of the particle and substrate. However, in the second case where surface oxides are present

(Fig. 1.6b), the particle kinetic energy is used to break-up the oxide layer, initiate ASI/jetting, extrude bare metal, and delaminate oxides to achieve metal-to-metal contact that leads to bonding. This additional energy requirement to remove surface barriers delay the onset of bonding, i.e., raises the v_{cr} needed for bonding to occur. As a result, metal-to-metal contact and bonding occur at a much lower impact velocity in an oxide-free surface case (Fig. 1.6a) than when surface oxides are present (Fig. 1.6b).

1.3 Motivation

Welding is a flexible manufacturing process commonly used to fabricate engineering components, particularly in cases where large structures or complex assemblies are challenging to manufacture using other methods. However, existing welding processes come with certain limitations (highlighted above) that can restrict their applications. Fusion welding, for instance, involves high heat input, leading to issues such as oxidation, porosity, distortion, and heat-affected zones, which can compromise the integrity and service life of welded components. On the other hand, solid-state welding processes require expensive equipment and are often limited to simple geometry. There is therefore an on-going search for a welding process that can effectively join complex geometry materials without introducing unwanted defects or requiring extensive post-processing.

The cold spray process, known for depositing materials at very low temperatures, offers a promising solution to reducing or eradicating post-weld thermal defects. By operating at low temperatures, we postulate that the cold spray process can minimize and eliminate many of these deleterious defects typically induced by the traditional high-temperature welding process. As the use of CS continues to expand in various industries, this thesis tends to explore its potential for solid-state welding, a process hereafter called *cold spray welding* (CSW). This research aims to

harness the advantages of the CS process to overcome the limitations of traditional welding techniques, contribute to advancements in welding technology, and offers an innovative approach to meeting the demands of modern engineering fabrication needs.

1.4 Objectives

The overall goal of the study is to *design* and *develop* the proposed CSW process using AA 6061-T6 as the base metal. The specific objectives are to:

- Re-examine the origin of softening in an existing liquid-state welding technique (TIG-welding). *The manuscript in Chapter 2 solely addresses this objective.*
- Design and develop the proposed CSW process, and compare the mechanical performance of CSWed parts with those of traditional TIG-welded parts, to provide direction for future CSW optimization. *The manuscript in Chapter 3 solely addresses this objective.*

1.5 Thesis Organization

Chapter 1 presents the relevant literature that supports and contextualizes the subsequent chapters, followed by the motivation and objectives of the study. Chapter 2 document findings from a comprehensive re-examination of softening phenomenon in TIG-welded AA 6061-T651 using experimental techniques, analytical modeling, and thermodynamic simulation. The findings in this chapter suggest the need for continuous exploration of new welding techniques that minimize nanostructural changes in the surrounding weld area, particularly in precipitation-hardened alloys. Chapter 3 focuses on evaluating the potential of the CS process for solid-state welding. Additionally, a comparison is made between the results of the cold spray-welded samples and TIG-welded samples to assess the current limitations and potential for future optimization. The study

highlights some benefits of cold spray-welded samples, including minimal microstructural alterations, prevention of phase transformation, and suppression of Heat-Affected Zone (HAZ) effects, which is a significant drawback of the existing welding techniques. Finally, Chapter 4 provides a comprehensive conclusion of the research conducted in this thesis. It also outlines future research directions that can potentially optimize and expand CSW for feasible industrial applications.

Statement of Contribution:

The author of this thesis, Muhammad Zia ud din Urf Umer, is the primary author of all the papers included in this thesis (Chapters 2 and 3). Dr. Ahmed A. Tiamiyu is supervisor of the author's Master of Science program. Their contributions are as follow:

Muhammad Zia ud din Urf Umer: Writing- Original Draft, Conceptualization, Methodology, Formal Analysis, Investigation, Data Curation, Visualization, Validation.

Ahmed A. Tiamiyu: Writing- Reviewing and Editing, Conceptualization, Investigation, Visualization, Validation, Funding acquisition, Supervision.

Chapter: 2 X-ray microscopic and thermodynamic model assessments of softening in TIG welded AA 6061-T651

Abstract

Fusion welding is extensively used for joining structural assemblies, especially those with complex geometries. However, it often results in heat-affected zones (HAZ) that are, in most cases, softer than other regions around and beyond the weld area. Coupling both experiment and thermodynamic modelling—electron microscopy, x-ray microscopy (XRM), and CALculation of PHAse Diagrams (CALPHAD)—we re-examine the origin of softening in tungsten inert gas (TIG)-welded heat-treatable AA 6061-T651 for more comprehensive understanding of its (softening) evolution. This study reveals material softening up to at least 38 mm away from the weld center, and partitioned heat-affected zones—HAZ1, HAZ2, HAZ3, and HAZ4—based on peak temperature, associated hardness, and precipitate phases in these zones. Analytical modeling and thermodynamic simulation predict solid solution and further precipitation of coherent GP zones in HAZ1, while coarsening of pre-existing precipitate occur in HAZ2 (non-coherent/stable β-Mg_2Si), HAZ3 (both semi-coherent/metastable β' and coherent/metastable β") and HAZ4 (coherent/metastable β") phase. These welding-induced transformations—origin of softening—results in non-homogenous hardness in the zones compared to the unaffected base-material (120 HV): HAZ1 to HAZ4 are 66-72, 54-64, 64-94, and 95-106 HV, respectively. Under tensile load, TIG-welded sample fractures at the softest region—HAZ2. Additionally, XRM analysis confirms the presence of porosity in the welded area, and their mobility during plastic deformation, so that the severity of softening has a significant influence on localized fracture than the presence of porosity in the weld area. This work shows that new welding technologies that minimize

nanostructural changes in base materials, especially precipitation-hardened alloys, should be sought.

2.1 Introduction

The design of large components with complex geometries face significant challenges due to the associated high costs of fabrication and logistic difficulties [44]. As a result, the process of assembling and joining parts is often viewed as a more efficient option. To select the appropriate joining process, it is important to consider application service conditions [45]. In applications where safety regulations are more stringent, e.g., chemical plants and pipelines, welding is considered a reliable material joining process [46], and weld strength depends on “strong” metallurgical bonding achieved either by fusion or diffusion process [44]. Fusion welding processes, like tungsten inert gas (TIG) welding and shielded metal arc welding, are widely accepted in industries due to their high production rate and ability to join complex geometries [5]. However, high temperature involvement in fusion welding processes accelerates oxidation, thermal defects, porosity, distortion, induced high stress, and heat affected zone (HAZ)—typically a "weaker” region between the weld and the rest of the adjoining base material [47–50]. HAZs are mainly the concentration point of failure that usually require post-processing treatment of the welded parts. Continuous efforts are necessary to enhance existing welding technologies or devise novel processes that fulfill production quality demands without the need for supplementary post-processing or investment [2].

Among many structural alloys, aluminum alloys are highly sorted by industries due to their lightweight properties (i.e., high strength-to-weight ratio) and excellent corrosion resistance [51–53]. As a result, they find extensive applications in many industrial sectors—automotive and

aerospace—that sort energy-efficiency and poisonous gas emission reduction [13,14]. Aluminum alloys are usually joined by fusion welding processes, and extensive softening in the HAZ, especially in the heat-treatable alloy series, has been reported. Previous studies have been conducted to understand this softening behavior. Vargas et al. [56] studied the thermal transitioning in welded aluminum alloy 6061-T6 (AA 6061-T6): they showed that the increase in welding heat input leads to the transformation of coherent precipitate to semi-coherent metastable phase in HAZ, and in turn, a proportional decrease in hardness and strength of the alloy. Lu et al. [57] investigated the behavior of TIG welded spray formed 7055 aluminum alloy and further partitioned HAZ area into *solid solution* (HAZ1) and *over-aged* (HAZ2 and HAZ3) zones, caused by the dissolution of coherent precipitates and coarsening of the non-coherent precipitates, respectively. There have since been different HAZ partitioning reported in the literature: HAZ1-HAZ2 [58–60], HAZ1-HAZ3 [61,62]. While other welding defects such as cracks and distortion can be improved by modifying the welding process, such HAZ "softening" is an inevitable consequence due to the high heat input during the fusion welding process [63]. As such, researchers are exploring various techniques for joining heat-treatable Al-alloys and other HAZ-prone alloys with minimal softening gradient [62]. Recent work by Cheng et al. [64] reported minimized softening of HAZ in welded heat-treatable Al-alloy by in-situ cooling and post-weld rolling.

The literature so far shows variability in HAZ partitioning, and the non-comprehensive information on the details of HAZ, their temperature ranges, and the corresponding precipitates responsible for softening. We theorize that a comprehensive understanding of the origin of softening in HAZ can be a starting point for designing welding processing pathways that effectively minimize softening gradient and improve weld quality. It is therefore our aim to

specifically re-examine the origin of softening in welded heat-treatable AA 6061-T651; besides grain size, strengthening in this alloy primarily depends on the morphology and coherency of constituent precipitates with the matrix, and their interaction with line defects (dislocations) [51], and they are affected by the thermal cycle around the weld area. We couple both experimental and thermodynamic modelling approaches to understand the softening behavior of the welded aluminum alloy components: scanning electron microscopy (SEM), electron dispersive spectroscopy EDS and x-ray microscopy (XRM) analyses were conducted to assess micro-defect in greater details; CALculation of PHAse Diagrams (CALPHAD)—Thermo-Calc—was used for the thermodynamic and kinetic prediction of precipitates that drives softening; and mechanical tests (hardness, tensile, and impact) were conducted to assess the effect of associated softening behavior on the integrity of welded samples.

2.2 Experimental procedure

2.2.1 Materials and welding process

The TIG welding of AA 6061-T651 plate was investigated in this study. The T651 temper implies that the as-received alloy was solution heat-treated, followed by artificial ageing, and finally stress relief by stretching up to 1.5-3 % [65]. The as-received plate was machined to a dimension: 200 x 55 x 6 mm (length x width x thickness) for each side of the weld coupon, as shown in Fig. 2.1a. A filler wire ER-4043 with a diameter of 1.6 mm was used for the welding process. The chemical composition of both the plate and filler wire is provided in Table 2.1. Prior to welding, a single V-groove with a bevel angle of 35° (included angle: 70°) was machined at the edge of each plate, as shown in Fig. 2.1a. The AA 6061-T651 plate designated for welding underwent preparatory steps which involved brushing with a stainless-steel bristled brush, followed by a thorough wipe-down

using an acetone-soaked cloth. The welding process was manually carried out using argon shielding gas, with a 2 % thoriated non-consumable tungsten electrode. The welding parameters employed are listed in Table 2.2

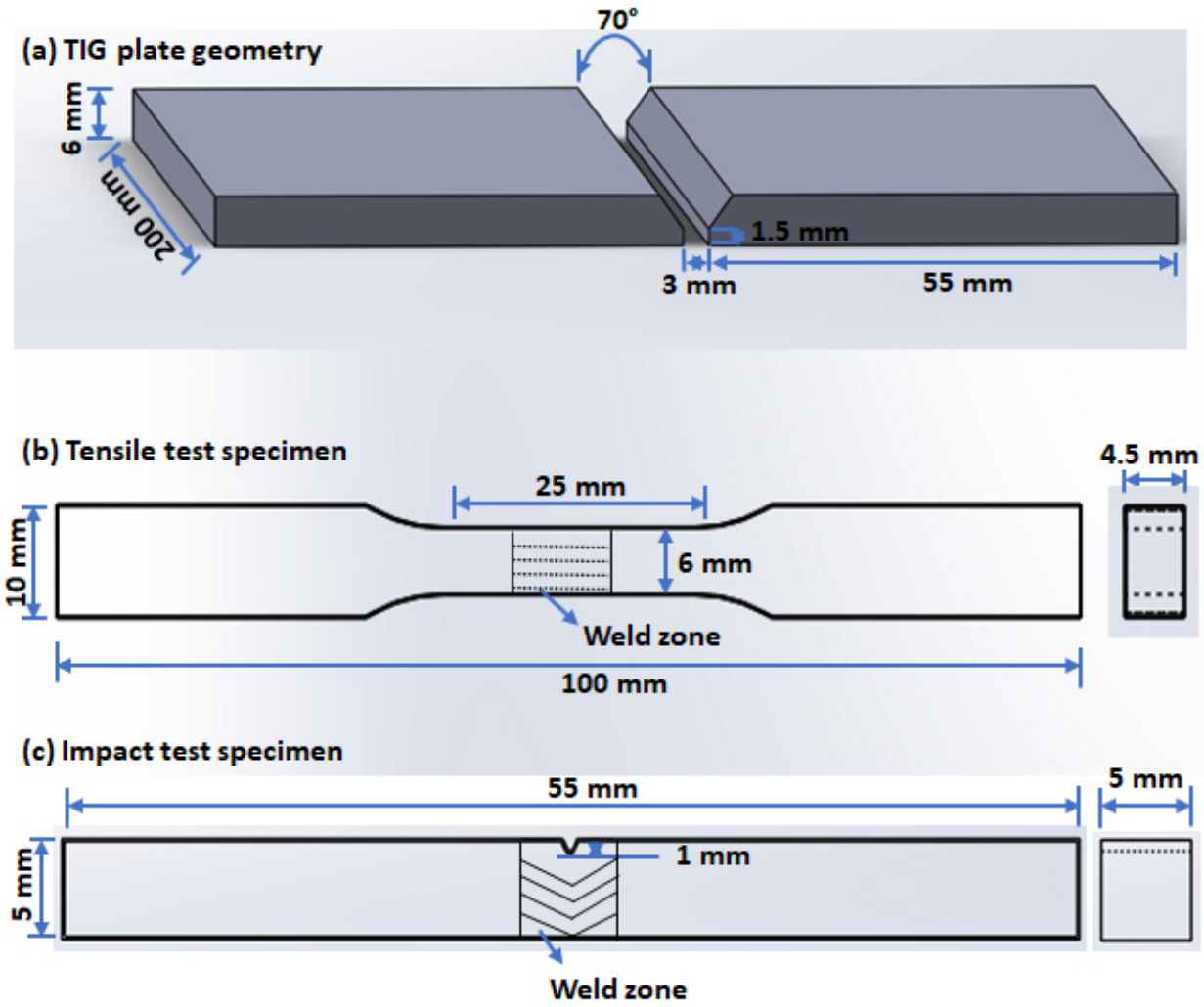

Figure 2.1: Geometry of (a) AA-6061-T651 plate for TIG welding, (b) tensile test specimen, and (c) impact test specimen.

Table 2.1: Chemical composition of Aluminum alloy 6061-T651 and TIG welding filler wire Al-4043.

Element	Si	Mg	Fe	Cu	Mn	Cr	Zn	Ti	Be	Al
AA-6061-T651	0.7	1.0	0.41	0.27	0.12	0.18	0.01	0.02	-	Bal.
AA-4043	5.00	-	0.20	0.03	-	0.09	0.01	-	0.00003	Bal.

Table 2.2: TIG Welding Parameters.

Parameters	Polarity	Current (A)	Voltage (V)	Travel speed ($mm.s^{-1}$)	Argon flow (cfh)
Value	AC	220	15	2.54	18

2.2.2 Microstructural and mechanical characterization

The samples for microstructural analyses were prepared following standard metallography steps described in ASTM E3-11 (2017) [66]. This was followed by 2 hours of vibratory polishing using a BUEHLER VibroMet2 machine, with 0.025 µm colloidal silica as a polishing solution and a vibration amplitude of 20 percent. Samples for SEM and optical microscopy analyses were etched with Keller's reagent for 1 minute. The grain size of the as-received AA 6061-T651 plate is 52 µm ±10, it was measured using an optical microscope (LEICA DM6000M), and determined according to the ASTM E112-13 standard [67]. SEM and energy dispersive spectroscopy (EDS) were conducted using a Bruker Nano GmbH Berlin, Germany instrument coupled with an XFlash 5030 EDS detector. The SEM was operated at 15 keV. It should be noted that EDS analysis was conducted on an unetched mirror-polished samples.

Micro-hardness test was performed according to ASTM E92-17 using a Buehler, Wilson® Tukon™ 1202 automated Vickers hardness tester. The set load was 300 gf, and the residence time was 10 seconds. The horizontal and vertical spacing between indents is 1 mm. For the welded sample, a hardness test was conducted up to 38 mm from the weld center. Tensile tests were carried out on both the as-received and TIG-welded samples (schematized in Fig. 2.1b) using Tinius Olsen model H25KS universal testing machine: the test procedure and sample dimensions were in accordance with ASTM E8/E8M-21 [68]. The tensile test was conducted at a crosshead speed and corresponding strain rate of 1.25 $mm.min^{-1}$ and 0.05 min^{-1} (8.3×10^{-4} s^{-1}), respectively. Using an Amsler Otto Wolpert-Werke GMBH D-6700 impact tester with a capacity of 4J in Charpy mode,

impact test was conducted at a velocity of 3 $m.s^{-1}$ following ASTM E23-18 [69]; sample dimension is shown in Fig. 2.1c. The average values of three tensile and impact test measurements are reported in this manuscript. All mechanical tests were conducted at room temperature.

2.2.3 Thermodynamic modeling

CALPHAD is a computational method used to develop thermodynamic and property databases, which enable the calculation of phase equilibria and other thermodynamic properties of binary and ternary systems to higher-order systems [70]. In this study, Thermo-Calc 2023a was used to perform CALPHAD calculations. The phase diagram module, along with the TCAL8: Al-alloys V8.2 database, was employed to calculate the amount and composition of phases/precipitates. To model precipitation kinetics (precipitate simulations) at the HAZ and weld zone, the non-isothermal simulation was carried out using the precipitation module—TC-PRISMA with Aluminum based alloys database package coupled with thermodynamic database TCAL8: Al-alloys V8.2 and kinetic database MOBAL7: Al-alloys mobility v7.0.

2.2.4 X-ray microscopy assessment

X-ray microscopy (XRM) analysis using Xradia Versa XRM-520 machine was conducted to investigate the porosity, crack, and softening behavior of the base material, TIG-welded samples, before and after testing. The XRM scan was performed using the following parameters: source voltage of 160 kV, current of 62 μA, and power of 10 W. To ensure complete coverage of the entire weld and heat-affected zone (HAZ) regions of the tensile specimen, the XRM scan was conducted with a pixel size of 25.24 μm. Additionally, high-resolution images were obtained with a pixel size of 3.07 μm.

2.3 Result and discussion

2.3.1 Microstructural evolution in TIG-welded samples

The overview of the TIG-welded sample in Fig. 2.2a shows the weld area and its neighboring adjoining region. The welding process induces high heat input that causes microstructural changes in and surrounding weld area [71]. High magnification images in Fig. 2.2 (b, c) show distinct microstructural features: dendritic structure in the weld area, fusion line, and native second-phase particles in HAZ. Usually, aluminum alloys show dendritic structure due to the fast cooling and large solidification temperature ranges, where primary phases are solidified first, in a dendritic or

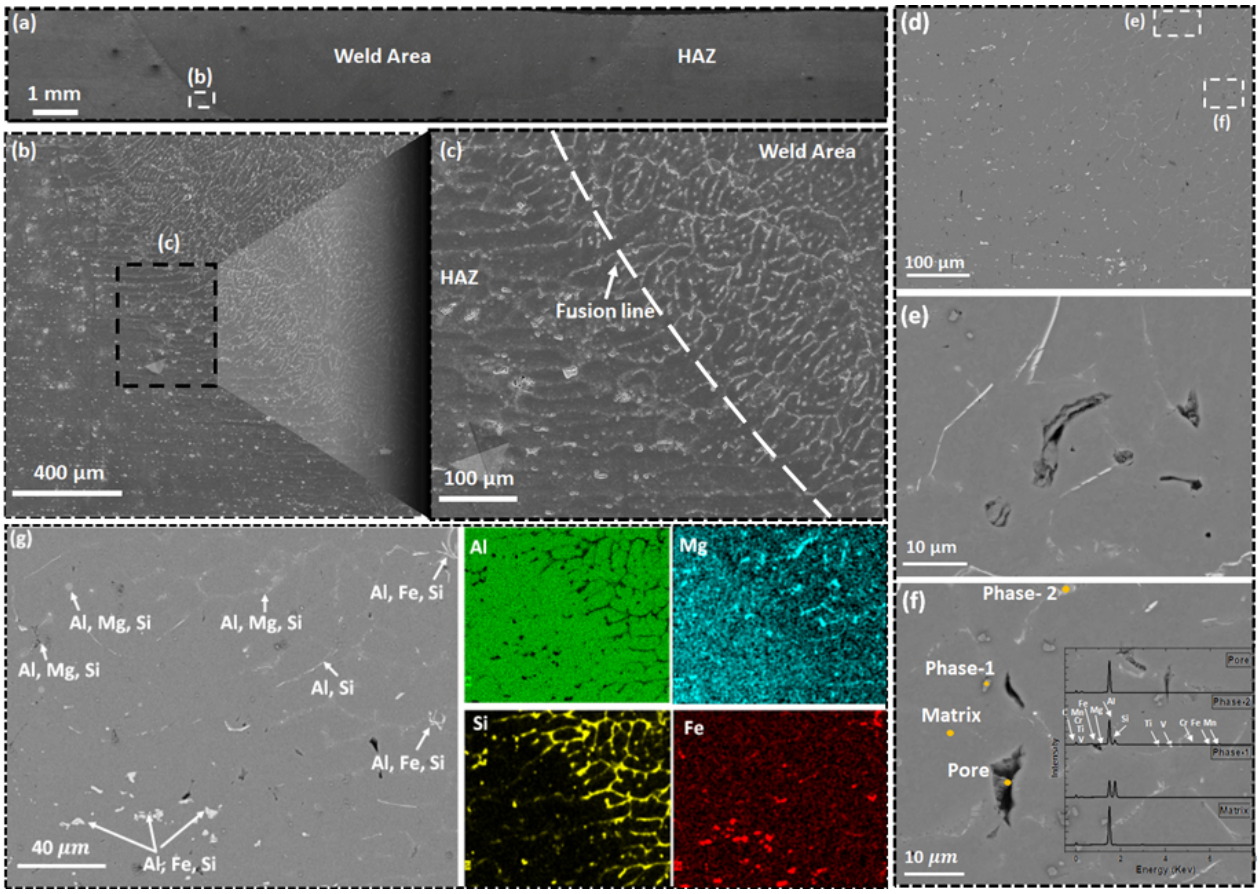

Figure 2.2: SEM images and EDS maps/profiles of TIG-welded AA 6061-T651: (a) overview of the welded sample, (b & c) weld area, fusion line and HAZ, (d-f) porosity in the weld area, and (g) EDS map of the Weld area & HAZ. Inset in (f) is the EDS spectra of the points in the SEM image.

tree-like structure, while the remaining liquid in the material backfills the spaces between dendrites [52,72].

Meanwhile, the fusion line points to where the weld area is fused to the parent material. Fig. 2.2(d-f) shows the coevolution of intermetallic phases mainly at the grain boundaries or interdendritic regions and the presence of pores in the weld area. To delineate dark pore regions in Fig. 2.2 e, f from other microstructural features observed in the weld area, EDS point analyses were conducted. The EDS spectra for α-Al matrix and pores in the inset of Fig. 2.2f shows a similar dominant Al peak; this validates the presence of pores since there is an extension of the α-Al matrix (grey) to the indexed dark pore region. Such micropores are not observed outside the weld area; this can also be discerned in the comparative 3D XRM images of the base "as-received" material and TIG-welded sample shown in Fig. 2.3. The 3D high-resolution image of the base material shows a near-homogenized and porosity-free volume in Fig. 2.3b, while the weld area in the TIG sample shows a significant amount of pores in Fig. 2.3c. The 2D slices of XRM images for the base Fig. 2.3b(i-iii) and weld area Fig. 2.3c(i-iii) at different selected locations further confirms that pores are ubiquitously distributed throughout the entire volume of the weld area.

The high-temperature involvement of the fusion welding process accelerates the tendency for aluminum alloys to trap air and undissolved gases—usually hydrogen—in a molten weld pool; this can lead to micropores formation [8]. The solubility of hydrogen in molten aluminum is approximately 20 times higher than in solid aluminum, and as a result, when aluminum alloys are welded, the weld pool absorbs and dissolves hydrogen from the surrounding arc atmosphere, depending on its partial pressure. Nevertheless, upon solidification, the quantity of hydrogen in the weld pool exceeds the solubility limit, resulting in the formation of porosities [73].

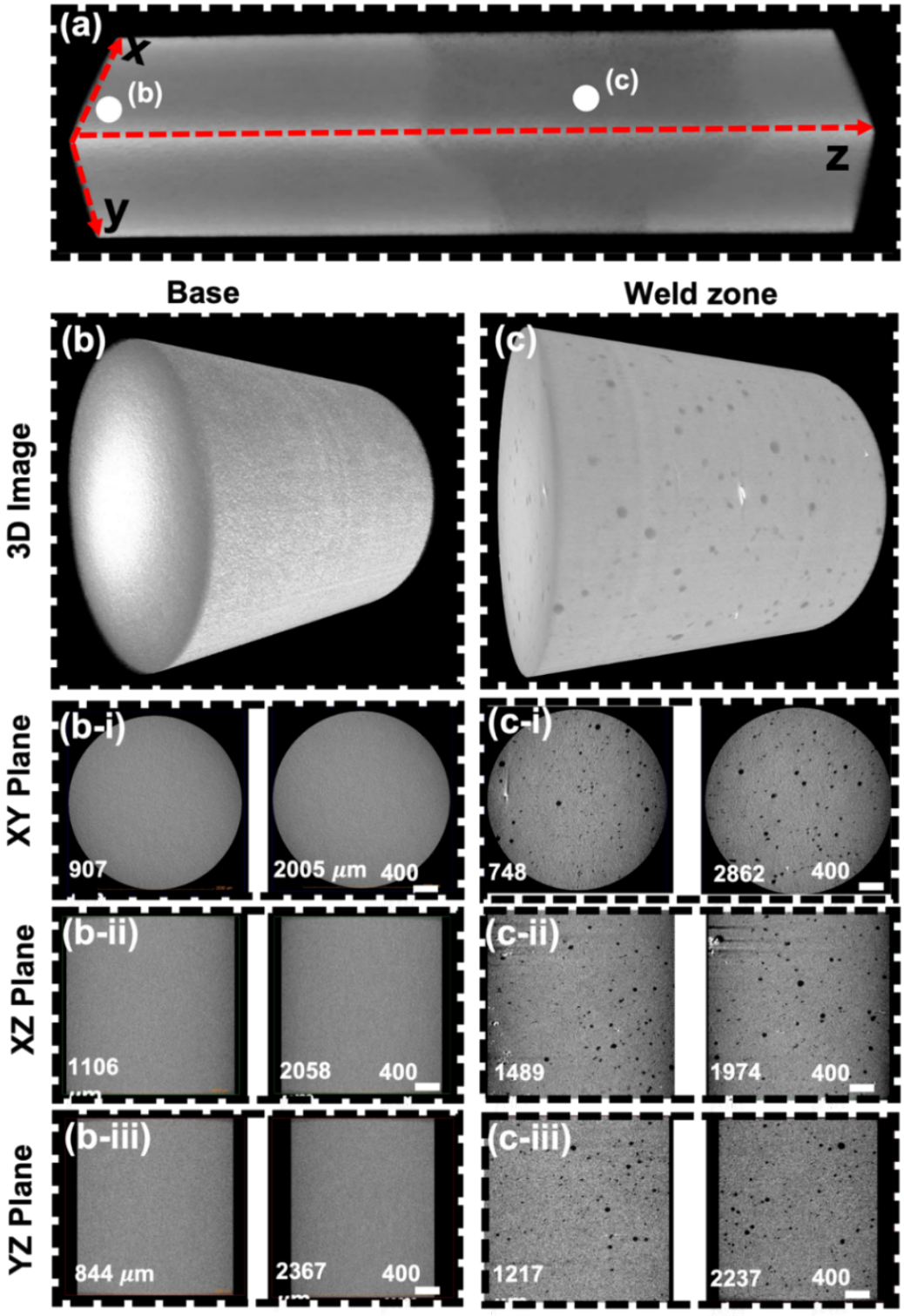

Figure 2.3: (a) Low and (b,c) high resolution XRM images of a TIG-welded sample extended to the base area: (a) overview, (b) 3D image of base material and corresponding 2D slices in XY, XZ & YZ planes, and (c) 3D image of weld zone in TIG-welded sample and corresponding slices in XY, XZ & YZ planes.

The occurrence of weld porosity is heavily influenced by the kinetics of solidification. Previous studies have shown that when the solidification front is dendritic, bubbles get entrapped in the inter-dendritic region [74]. During the solidification of the welding pool, dendritic structures are dominant and as a result, gas porosity is a common defect in the welded area.

Moreso, light metals like aluminum alloys are more prone to absorb gases, and as a result, higher hydrogen solubility accelerates the formation of porosity that are deleterious [75]. An alternate mechanism of pore formation is via the evaporation of magnesium during the fusion welding of 5000 series Al alloys, as reported in Refs. [76,77]; this is hardly the case in the current study, since the filler wire mainly constitutes Al and Si. The effect of heat input on the structural changes depends on the composition of the alloy, the cooling rate, and the heat transmitted to fuse the metal [71]. Many defects formed during melting, remelting, and solidification process. Undoubtedly, any defect present or created during the welding stage could be carried on to the final microstructure and in turn affects its performance [75].

Meanwhile, intermetallic phases 1 and 2 within the weld area in Fig. 2.2f (and inset) are rich in Al and Si as the main constituent elements. The EDS maps of the weld area in Fig 2.2 g also revealed the presence of Al-Si second phase in α-Al matrix and mainly along the grain boundaries. These Al-Si rich regions are the Al-Si eutectic phase in α-Al matrix of a 4000 series aluminum alloy [36]. Although an ER-4043 filler wire mainly constitutes Al and Si (Table 2.1), few Al-Fe-Si and Al-Mg-Si phases can also be discerned within the weld area. Mg and Fe in the weld area could originate from the trace elements of the filler wire or the nearest HAZ area of the AA 6061-T651 plate that constitute mainly Al-Fe-Si and Al-Mg-Si intermetallic phases in Fig. 2.2g. The thermodynamic phase modelling—Thermo-Calc equilibrium solidification diagrams in Fig. 2.4—

for both the base and weld area supports the observed intermetallic phases in the EDS results in Fig. 2.3g. Below the melting point, Thermo-Calc simulation confirms that the stable Al-Fe-Si intermetallic phase in the weld area and surrounding HAZ is a stoichiometric $Al_9Fe_2Si_2$ phase. The $Al_9Fe_2Si_2$ is a transformation of Al_8Fe_2Si that forms at an earlier stage through a peritectic reaction, as reported in Ref. [78] and also shown in Fig. 2.4a. The Themo-Calc simulation also predicts the stable precipitate phase—Mg_2Si-C1 precipitate—in the base AA 6061-T651 that eventually drives softening in HAZ, as it will be discussed later in the subsequent section.

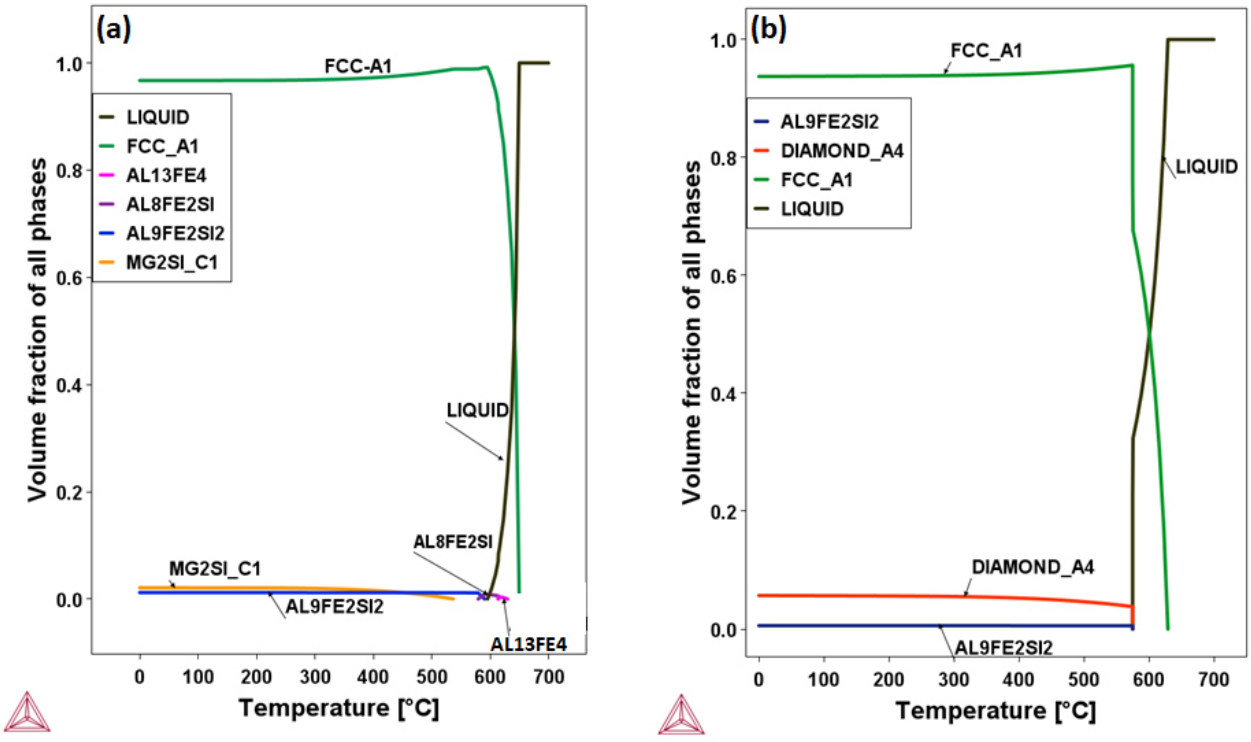

Figure 2.4: Thermo-Calc equilibrium solidification diagrams showing the volume fraction of phases at different temperatures for (a) base material with composition Mg: 1%, Si: 0.70%, Fe: 0.41%, Al: bal., and (b) filler wire with composition Si:5%, Fe:0.20%, Al: bal.

2.3.2 Evolution and evaluation of softening in TIG-welded sample

2.3.2.1 Hardness results and the evolution of softening

The hardness—a measure of material's resistance to surface plastic deformation [79]—results of the TIG-welded AA 6061-T651 sample from the mid-weld region to about 38 mm away is presented in Fig. 2.5. The result shows severe hardness non-uniformity that can be distinctly partitioned into weld zone and HAZ. The variability of hardness within the HAZ further partitions into four zones—HAZ1, HAZ2, HAZ3, and HAZ4, as summarized in Table 2.3. The hardness in the partitioned zones is noticeably lower than the unaffected base material (120 ± 4 HV), suggesting a case of material softening sets on.

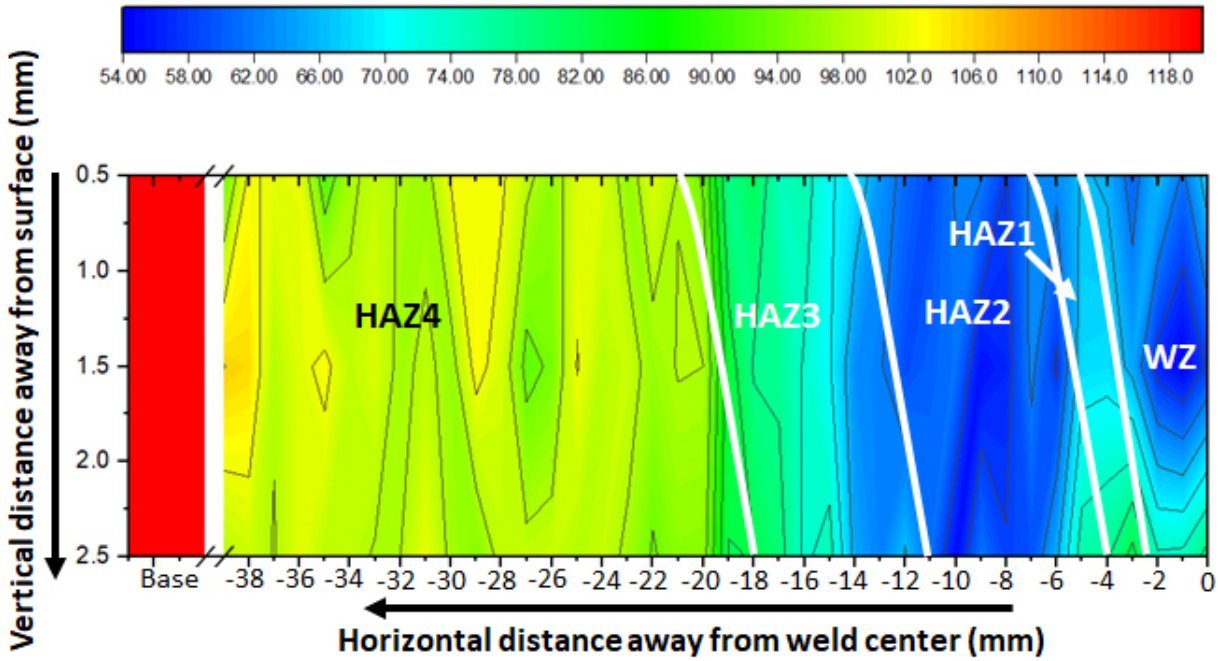

Figure 2.5: Hardness test contour map of TIG-welded sample from weld center up to 38 mm away from it. The hardness value of the unaffected base material is appended for easy comparison. The color legend values are in HV.

We, therefore, estimate the degree of softening—the hardness difference between the base metal and other observed zones [60]—as 51 HV, 61 HV, 41 HV, 19.5 HV, for HAZ1, HAZ2, HAZ3, and HAZ4, respectively. Away from the weld zone, the initial slight rise (HAZ 1), drop (HAZ 2), and

rise again (HAZ 3) in hardness as shown in Fig. 2.5 has been observed by other researchers [51,57,59,62,80]. Although lower hardness in the HAZ is not surprising, recording a lower hardness even up to 38 mm away from the weld center is, more so that there is no discernable microstructural difference between the HAZ and the unaffected base metal, at least, at the scale of the SEM and the XRM (only the presence of pores in the weld area). We, therefore, repeated the hardness test on a new sample from the same welded coupon (results not shown here); the same behavior—lower hardness up to 38 mm away from the weld center—is observed.

Table 2.3: Hardness range, average temperature, and cooling rate for each partitioned HAZs.

Zones	Hardness (HV)	Average Temperature °C	Cooling rate, $^{o}Cs^{-1}$
HAZ1	66-72	525	10.33
HAZ2	54-64	306	1.20
HAZ3	64-94	155	0.16
HAZ4	95-106	79	0.01

It should be noted that AA 6061 is a precipitation-hardened alloy where Al supersaturates with magnesium (Mg) and silicon (Si) elements to form an α-Al matrix. During cooling from temperature above the solvus line where homogeneous solid solution forms, these alloying elements combined to form a β-Mg_2Si precipitate in the α-Al matrix [59]. Besides grain size, strengthening in AA 6061 is primarily dependent on the morphology and coherency of this precipitate [51]. Generally, the precipitation sequence in Al–Mg–Si alloys is shown in Eq. (2.1) [81,82].

$$(SSSS) \rightarrow \text{Cluster/ GP zones} \rightarrow \text{metastable } (\beta'') \rightarrow \text{metastable } (\beta') \rightarrow \text{stable } (\beta) \quad \ldots (2.1)$$

where *SSSS* is super saturated solid solution that contains more solute than it would normally be able to dissolve, resulting in a metastable state and can undergo further precipitation or phase

separation upon further thermal treatment [83]. When aging at a lower temperature range much below the solvus, the formation of solute clusters and/or Guinier-Preston zones (GP zone) first set on. At an extended time, the GP zone gradually transforms to coherent metastable precipitates (β"), semi-coherent metastable precipitate (β'), and an incoherent stable (β), in that order as expressed in Eq. (2.1). While the sequence of precipitates is accompanied by a change in morphology, strengthening contribution also decreases as the precipitate loses coherency with the matrix. These observations beg the question of "to what extent", in terms of distance, should this effect be felt from the weld area? In what follows, we evaluate the softening behavior by examining nanostructrural changes—precipitate nucleation, volume fraction and growth—that possibly set on due to heat input and temperature variation from the weld zone.

2.3.2.2 Temperature variation and thermodynamic prediction of precipitate nucleation, growth, and volume fraction.

Heat-treatable aluminum alloys at their peak-aged state, -T651, are characterized by a significant amount of fine precipitates that are coherent with the α-Al matrix; they offer maximum strengthening because of the significant resistance to slip as dislocations cut through the coherent precipitates [83,84]. During the TIG welding process, high heat input (Q) 1,169 J/mm, calculated by Eq. (2.2) [71,85], raises the temperature of the sample at and around the weld, and as a result, materials is subject to welding-induced ageing.

$$Q = \eta \frac{vA}{W} \quad \ldots (2.2)$$

where, η is welding efficiency 0.90 [71], v is voltage, A is current and W is welding/ travel speed. The heat input and in turn, temperature rise, could impact base materials in two ways: (i) solutionize the alloy system, and (ii) coarsen existing coherent precipitates in peak-aged aluminum

alloys—leading to loss of coherency and potential softening near the weld zone. It is therefore important to determine the actual thermal cycle characteristics, including peak temperature, and cooling rate of the welded joint; this will allow effective correlation of microstructure to material properties and performance [86]. We used the improved Rosenthal model Eq. (2.3) to calculate the peak temperature, T_p, up to 100 mm from the location of the welded center [57]; parameters are defined in Table 2.4.

$$T_p = 0.242\,(Q/\delta)/\rho\,C_p y_\circ \quad \ldots (2.3)$$

Table 2.4: Symbols, definitions, and values of the terms used for analytical modeling [87,88].

Zones	Symbol	Definition, Unit	Value
	T_p	Peak temperature	-
	Δt	Cooling time, s	-
	T'	Cooling rate, °C. s^{-1}	-
	T_0	Ambient temperature, °C	23
	Q	Heat input, J. m^{-1}	1169291
	δ	Plate thickness, m	0.006
	k	Thermal conductivity, W. m^{-1}- $°C^{-1}$	167
	ρ	Density, kgm^{-3}	2700
	C_p	Specific heat capacity, $J.kg^{-1}$ $°C^{-1}$	460
	$y_\circ$	Distance from the point, mm	-
HAZ1	T_1	Starting temperature of HAZ1, °C	590
	T_2	End temperature of HAZ1, °C	400
HAZ2	T_1	Starting temperature of HAZ2, °C	306
	T_2	End temperature of HAZ2, °C	200
HAZ3	T_1	Starting temperature of HAZ3, °C	160
	T_2	End temperature of HAZ3, °C	120
HAZ4	T_1	Starting temperature of HAZ4, °C	79
	T_2	End temperature of HAZ4, °C	60

Fig. 2.6 is the calculated T_p plot at various locations away from the weld zone. It is evident that the region immediately adjacent to the weld area experiences the highest peak temperature, which gradually decreases with increasing distance from the weld center. By considering the observed softening in Fig. 2.5, the calculated T_p for each HAZ is determined, and the average temperature

is provided in Table 2.3. Welding thermal cycle consists of rapid heating to a peak temperature, followed by cooling to ambient temperature [86]. The cooling rate at the weld area, as well as HAZ, greatly results in nanostructural changes, and it is calculated using the Rosenthal analytical solution using Eq. (2.4) [86]:

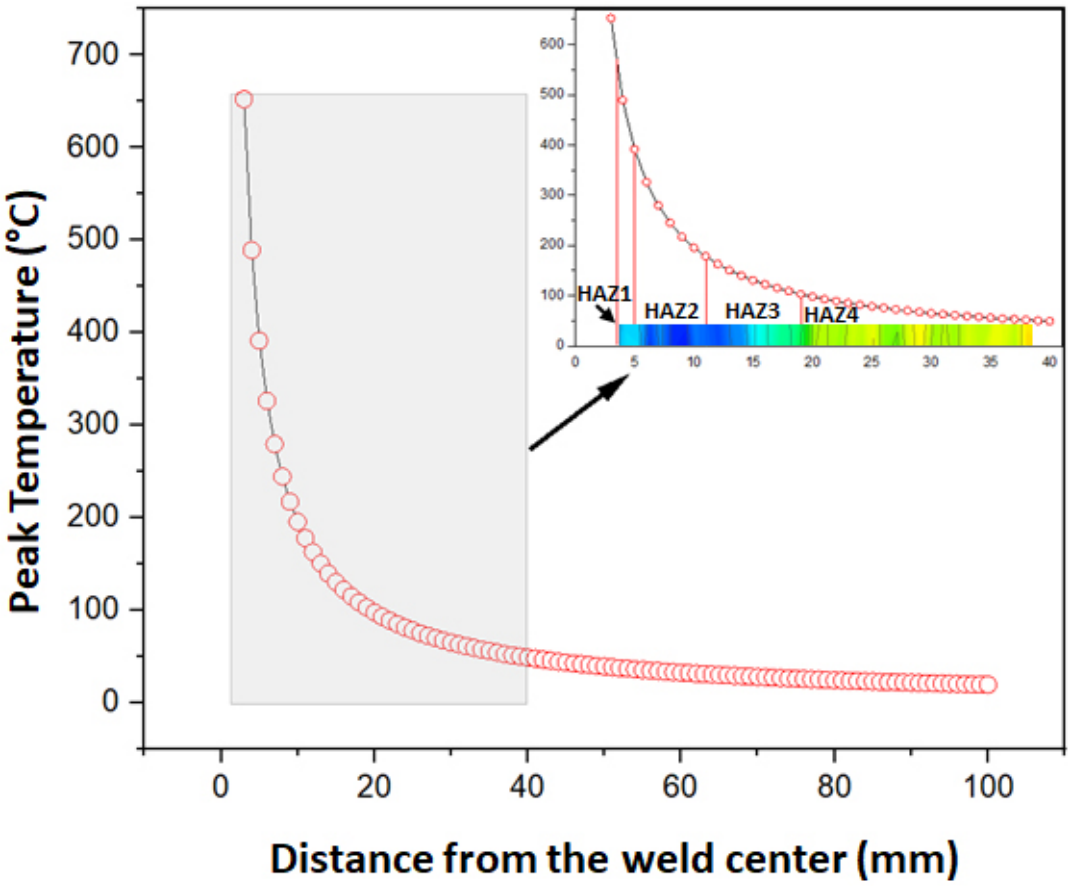

Figure 2.6: Analytical modelling of peak temperature, T_p, at different locations of weld sample.

$$T'_{1-2} = \frac{T_1 - T_2}{\Delta t_{actual}} \quad \ldots (2.4)$$

T_1 and T_2 are defined in Table 2.4, while Δt_{actual} is the actual cooling time calculated by:

$$\Delta t_{actual} = \Delta t_{thick-plate} + F.\left(\Delta t_{thin-plate} - \Delta t_{thick-plate}\right) \quad \ldots (2.5)$$

Δt_{actual} contemplate the cooling time for thick plate Eqs. 2.6, 2.7 (for 3-D heat flow) and thin plate Eqs. 2.8, 2.9 (for 2-D heat flow) following the assumption that the actual thermal situation lies between the two limiting solutions for thick and thin plates; weighing factor, F, taken as 0.6 [86].

$$\Delta t_{1-2} = \frac{Q}{2\pi k\theta 1} \quad \ldots (2.6)$$

$$\frac{1}{\theta_1} = \left[\frac{1}{(T_2 - \mathrm{T}_\circ)} - \frac{1}{(T_1 - T_\circ)}\right] \quad \ldots (2.7)$$

$$\Delta t_{1-2} = \frac{(Q)^2}{4\pi k\rho c d^2 \theta_2} \quad \ldots (2.8)$$

$$\frac{1}{\theta_2} = \left[\frac{1}{(T_2 - T_\circ)^2} - \frac{1}{(T_1 - T_\circ)^2}\right] \quad \ldots (2.9)$$

The cooling rate generated from Eqs. 2.4–2.9 are presented in Table 2.3, and they were also used in the Thermo-Calc software to execute the Precipitation Module-TC PRISMA. The average grain size of 52 μm for AA 6061-T651 was used in this module. Because the temperature rise in HAZ1 was up to the solutionization temperature for the investigated alloy—525 ^{o}C in Table 2.3—simulation was conducted without pre-existing precipitates, whereas the initial radius of pre-existing β''-Mg_2Si precipitates were set to 2 nm with needle-like morphology as reported in AA 6061-T651 [89–91], for HAZ2, HAZ3 and HAZ4.

In HAZ1, cooling rate (10.2 °Cs^{-1}) is significantly lower than those obtained in typical water quenching of a solution heat treatment process (400 °Cs^{-1} [92,93]). Hence, a "pure" supersaturated solid solution α-Al matrix is not expected upon the completion of cooling. This is validated by the thermodynamic simulation of nucleation rate for HAZ1 in Fig. 2.7a: 4.27 x 10^{-29} volume fraction of precipitates start to nucleate after 11 s of cooling at a nucleation rate of 1.51 m^{-3}s^{-1}. The

nucleation rate, accompanied by the increase in volume fraction of precipitates, increases over time until it starts to saturate at ~28 s. These precipitates are attributed to GP zones (typically with radius between 0.5 and 1.5 nm [94]) that contribute to the early stage of hardening; this in-turn, contributes to the slightly higher hardness value recorded in HAZ1.

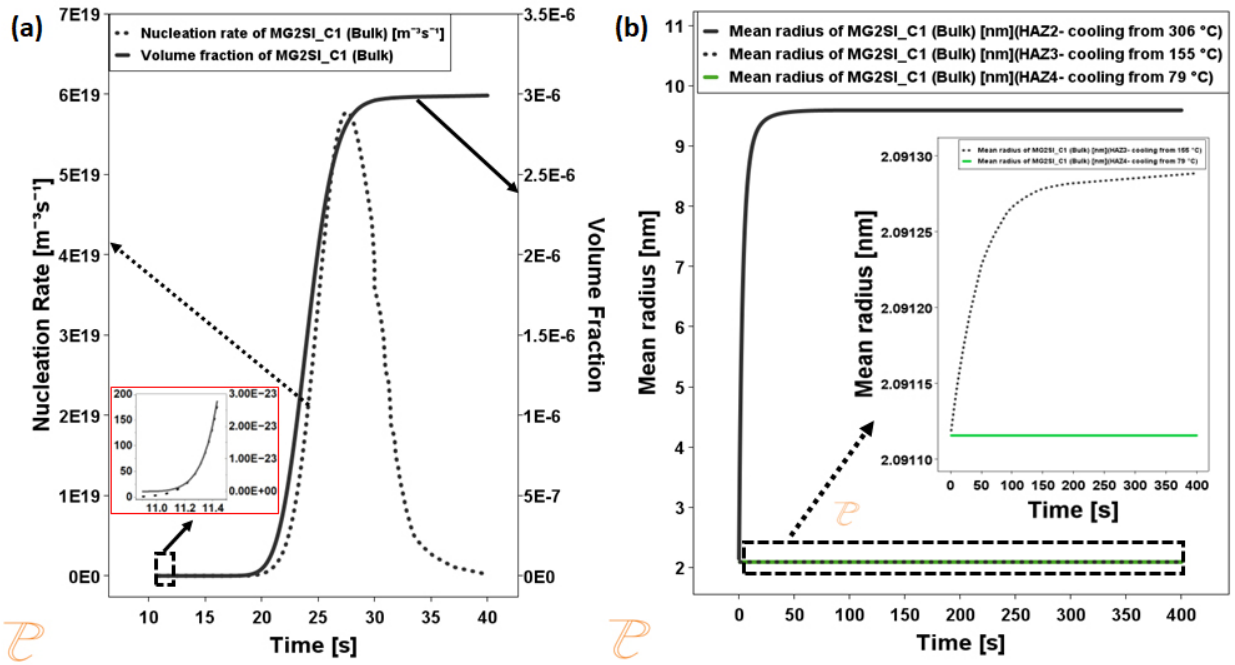

Figure 2.7: Precipitation calculations using the Precipitation module-TC Prisma: (a) nucleation rate and volume fraction of phase in HAZ1, and (b) mean radius for precipitation coarsening in HAZ2, HAZ3, and HAZ4.

Fig. 2.7b shows the growth kinetics of pre-existing precipitates in HAZ2, HAZ3, and HAZ4: it shows that the coarsening of pre-existing β''-Mg_2Si precipitates are more extensive in HAZ2, followed by those in HAZ3 and HAZ4 that show no significant coarsening. In the case of HAZ2, the non-isothermal simulation starts at 306 °C (Table 2.3), and the final precipitate reaches a radius size of 9.5 nm; this is significantly coarser than the reported size of β'-Mg_2Si phase (5 nm in radius [84,91]). This agrees with prior works that the precipitate growth rate depends on temperature and time. With increasing temperature and time, precipitate density decreases while its size increases; this coarsening weakens the alloy's strengthening effect, resulting in a continuous decrease in

microhardness [95]. According to the Orowan mechanism, when precipitates grow to a significant size, dislocations are unable to cut through the particles. Instead, dislocations bow or bulge around the precipitate until loops with opposite dislocation segments form, intersect and annihilate, as in the case of Frank-Read source for dislocation generation [83]. This annihilation allows the dislocation to continue its motion through the crystal lattice [83]. This is the origin of extensive softening in HAZ2—the resistance to slip is low, as dislocations would loop around incoherent precipitates rather than cut through them. We therefore conclude that in HAZ2, the heat input during TIG welding results in the transformation of pre-existing coherent β"-Mg_2Si to coarser stable β phase that is incoherent with the α-Al matrix. Due to the lower temperature rise in HAZ3 compared to HAZ2, coarsening of pre-existing precipitates are less, as shown in Fig. 2.7b; hence significant transformation and departure from pre-existing coherent β"-Mg_2Si is not expected in comparison with HAZ2. Although we present no TEM results in this work, Cai et al. [96] found the evolution of β" in AA 6061 aged at 170 °C (*SSSS→ Cluster/ GP zones→ metastable β″*); this aging temperature is close to that obtained in HAZ3 (155 °C), and as such we predict that at least a *metastable β″→ metastable β′* transformation sets on since *β″* is a starting phase. We therefore rather suggest the coexistence of *β′* and *β″*-phase within the α-Al matrix in HAZ3, as also reported in Ref. [88]. These phases—*β′* and *β″*—are responsible for the higher hardness in HAZ3 (64-94), compared to that recorded in HAZ2 (54-64). Finally, although the hardness value of HAZ4 is lower than the unaffected base material in Fig. 2.5, the growth rate of precipitate in HAZ4 is significantly lower compared to other zones. Hence, precipitates in HAZ4 are untransformed, but rather a slightly coarser variant of the coherent pre-existing *β″*-Mg_2Si precipitate.

As already well established in heat-treatable alloys, coherent precipitates in peak aged state contribute highly to strengthening. However, when the coherent precipitate coarsens—over-aged

condition, they become semi-coherent metastable or non-coherent stable phases that in turn deteriorate strength of the heat-treatable Al-alloys [89,97]. Where the welded material is already in a peak aged condition, coarsening of the precipitates due to heat input can occur in regions away

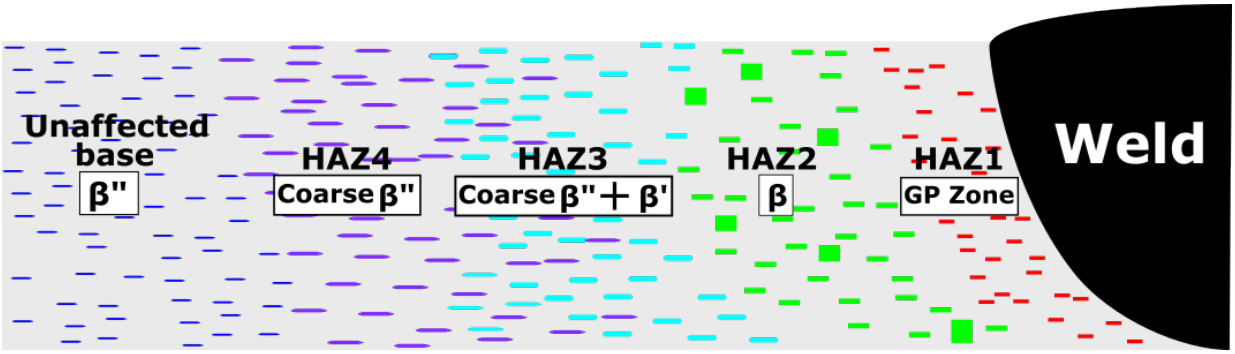

Figure 2.8: A schematic diagram showing unaffected base material and partitioned HAZ and their associated dominant precipitate phases.

from the weld zone, thereby leading to the softening [82]. A schematic diagram that summarizes the observation in this work is shown in Fig. 2.8: while HAZ1 solutionize and precipitates GP zones, HAZ2 experiences significant coarsening of pre-existing β''-Mg_2Si precipitate, the degree of which decreases in HAZ3 and HAZ4. Since heat input and temperature rise drives intrinsic nanostructural changes that lead to softening, we note that the variability in the number of partitioned HAZ (four in our case) compared to others in the literature (HAZ 1-2 [58–60], HAZ 1-3 [61,62]) This variability can be due to several factors, including the base material (an heat-treatable alloy would be more prone to variable HAZ zones than a non- heat-treatable alloy), plate thickness, welding process, power input, welding speed, and even the expertise of the welder [62,98,99].

2.3.3 Tensile and impact behavior of the as-received and TIG-welded samples

In the previous section, microstructural changes and in turn, the development of softening induced by the welding thermal cycle are established. To evaluate the behavior of the welded sample under

uniaxial load and impact (in comparison with the as-received sample), tensile and impact testing was conducted. A typical true stress-true strain curve in Fig. 2.9a shows that both the as-received and the TIG welded sample exhibited continuous yielding.

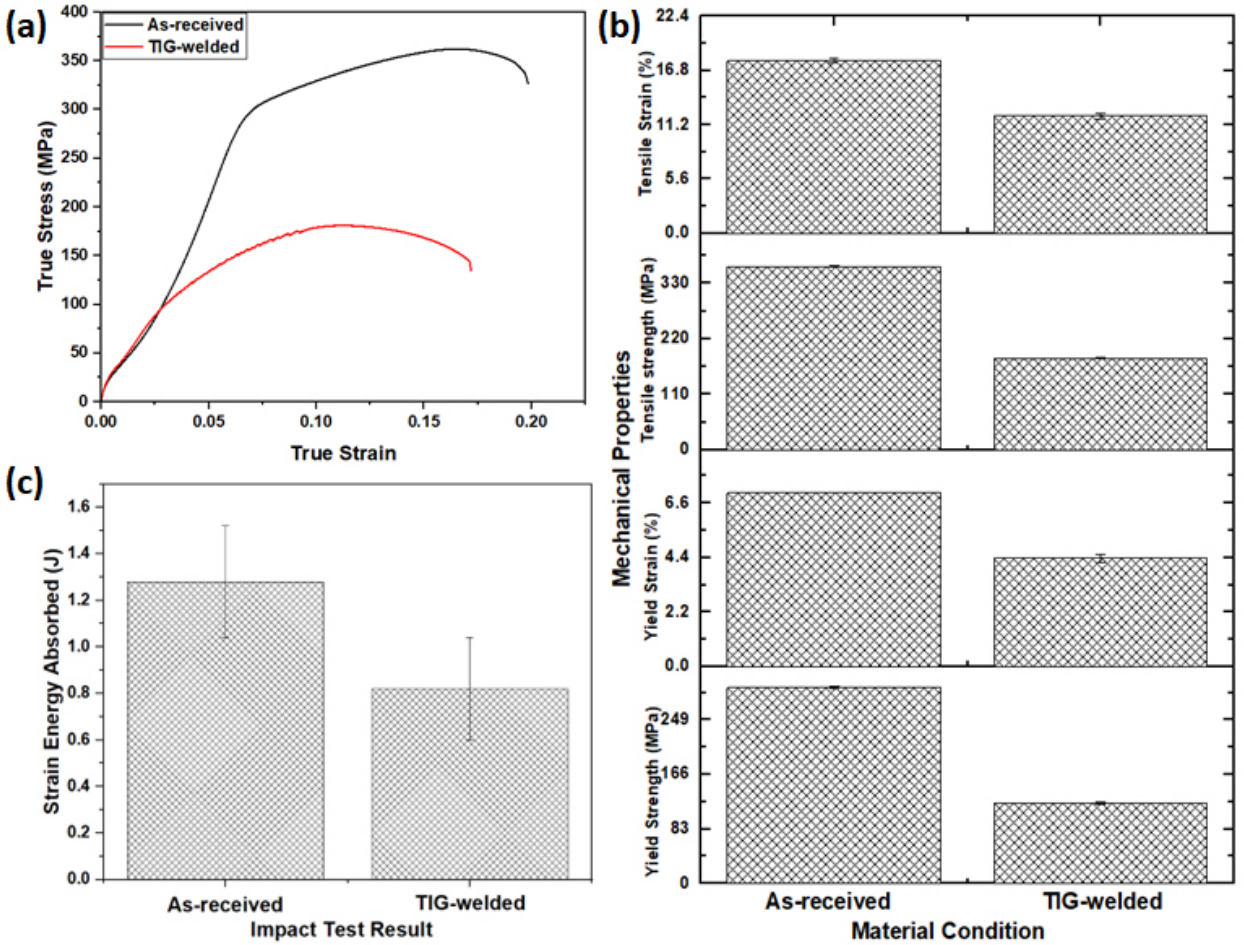

Figure 2.9: Mechanical test results for as-received and TIG welded sample: (a) True stress-strain curves, (b) extracted mechanical properties, and (c) strain energy absorbed during the impact test.

The mechanical properties are summarized in Fig. 2.9b and it shows: the yield strength and yield strain for AA 6061-T651 (298 ± 1.5 MPa and 7.02 ± 0.02 %) reduces by 59 % and 38.5 %, respectively, in comparison with its TIG-welded counterpart (122.6 ± 1.7 MPa and 4.3 ± 0.18 %). Similarly, the tensile strength and tensile strain for AA 6061-T651 (363 ± 1 MPa and 17.83 ± 0.235%) reduces by 50 % and 29 %, respectively, in comparison with its TIG-welded counterpart

(181 ± 1.2 MPa and a strain of 12.09 ± 0.26 %). The joint efficiency of the TIG welded sample, determined by the ratio of the tensile strength of the TIG welded joint to the tensile strength of the base material [59], is ~0.5. A similar effect in heat-treatable aluminum alloys welded by conventional welding processes—TIG and Metal Inert Gas welding—resulted in a joint efficiency below 50 % [100]. The Charpy Impact test results in Fig. 2.9c also show the degradation of mechanical performance of TIG-welded AA 6061-T651: the absorbed energies of the as-received and welded alloy are 1.28 ± 0.24 J and 0.82 ± 0.22 J, respectively. This indicates that the TIG welded sample exhibits approximately 36 % less impact toughness than the as-received alloy. These findings raise considerable safety concerns [64], which can limit the widespread application of heat-treatable aluminum alloys (e.g., AA 6061-T651) in welded structural applications.

In what follows, the results of XRM analysis of a welded sample measured fairly at the same orientation before and after the tensile fracture are shown in Fig. 2.10. A 3D image and slices of the welded sample before fracture re-affirms the presence of pores in the welded area in Fig. 2.10a. It also appears that there are more pores at the top surface (darker spots on 1580 μm-slice in Fig. 2.10a-i and 1460 μm-slice in Fig. 2.10a-ii) along the y-direction which corresponds to the later stage of welding pass. The XRM images of the fractured sample in Fig. 2.10b shows that pores flow along the tensile direction, and failure occurs at ~10 mm away from the weld center; this failure position coincides with the established softened HAZ2 region in Fig. 2.5. A high-resolution 3D images of the weld and HAZ (Fig. 2.10c and d), and fracture (Fig. 2.10e) areas clearly show that the eventual TIG-welded sample's failure region is the pore-free softened HAZ2. The 2D slices of the weld and HAZ areas in Fig. 2.10c(i-iii) and d(i-iii), and fractured area with micro-cracks in Fig. 2.10e(i-iii) at different selected locations further confirm that there are no pores after the weld-HAZ interface and that fracture location is mainly due to the severe softening in the HAZ.

Although many authors have reported failure at the HAZ [59,97,99,101], XRM results suggest that the presence of pores in the weld may be beneficial in delaying the onset of plasticity and in turn,

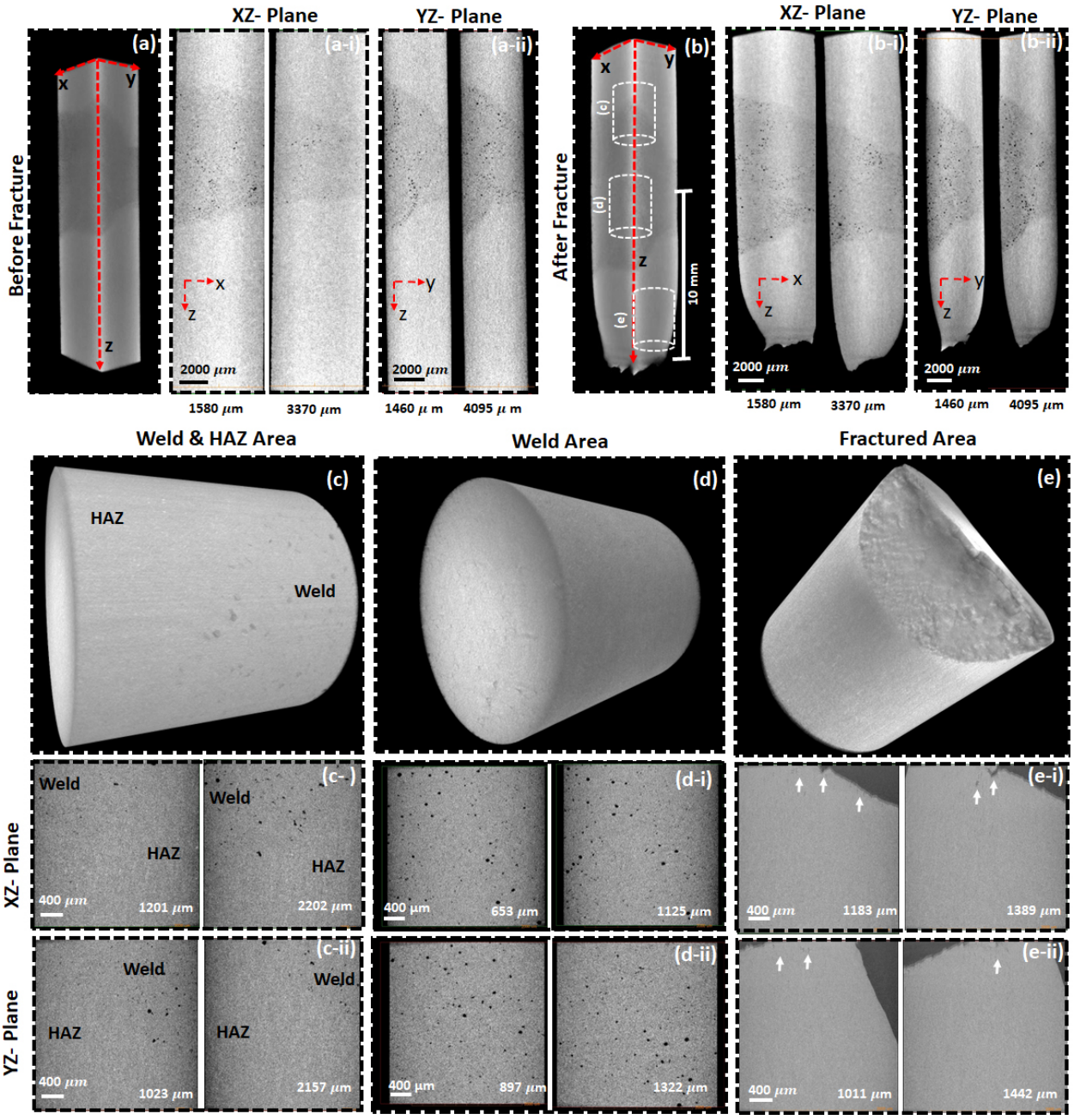

Figure 2.10: (a,b) Low and (c-e) high resolution XRM images of a tensile tested TIG-welded specimen: 3D images of the specimen and the corresponding 2D slices in XZ and YZ planes (a) before and (b) after fracture; 3D images and the corresponding 2D slices in XZ and YZ planes for the (c) weld and HAZ1 area, (d) weld area, and (e) the fractured area. (c and d) and (e) show micropores and microcracks adjacent to the fractured surface (white arrows) in the weld and HAZ2 area, respectively.

necking at the weld zone, especially for ductile aluminum alloy. This can be substantiated by comparing Fig. 2.10d (post-tensile testing) with Fig. 2.3c (pre-tensile testing), where reduction in pores size during plastic deformation is noticeable. We theorize that upon the application of load during tensile testing, the pores may require some energetic budget for closure; hence reducing the stress available to deform the weld zone, compared to other neighboring HAZs that are without pores. This also show that pores must exceed a percentage threshold for failure and fracture to occur in the weld area rather than HAZ2; this is corroborated by previous findings that porosity will drive mechanical performance if the percentage of pores exceeds a certain threshold [102–104]. Clearly, the pores in the weld zone in the current study do not result in a significant loss of strength in comparison with HAZ2. It can be concluded that in the welded AA 6061-T651, softening caused by precipitation transformation in HAZ2 is more significant to localize failure and fracture than the presence of porosity in the weld area. We, therefore, proceed to conduct fractographic analyses of the tensile tested as-received and TIG-welded specimens to discern the role of softening in fracture mode.

2.3.4 Fractographic analyses

Detailed fractographic analyses of tensile tested as-received and TIG-welded samples were conducted using SEM-EDS technique, and the results are presented in Fig. 2.11 and 2.12, respectively. Fig. 2.11a and 2.12a provide an overview of the fractured surface for as-received and TIG-welded samples, respectively. Compared with the as-received sample (width—20 % and thickness—26 %), the welded sample (width—20 % and thickness—38.5 %) experiences a more significant reduction in thickness under the applied load. The extensive thickness reduction in TIG-welded sample is due to HAZ2 softening that is established in *section 2.3.2.1*.

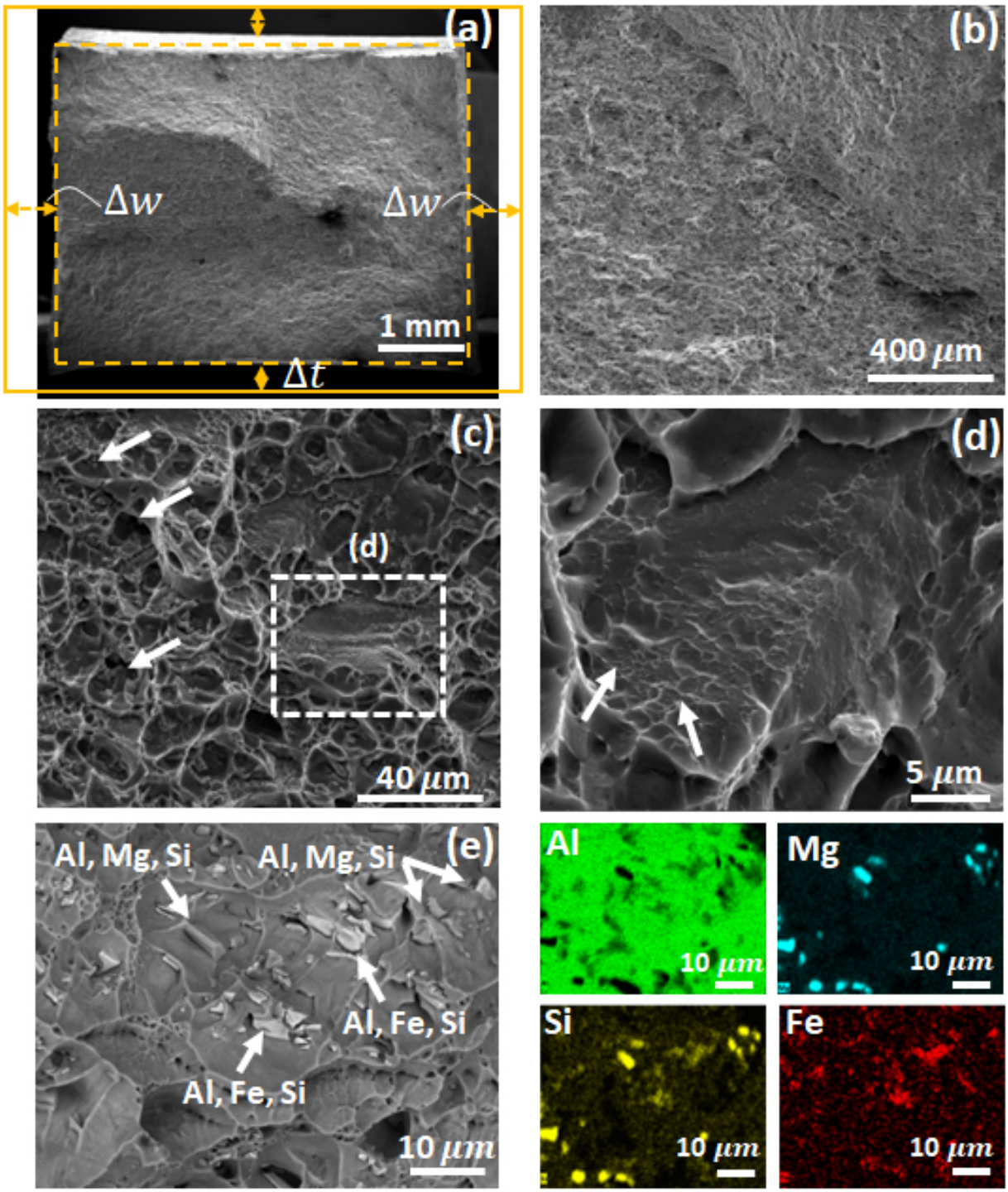

Figure 2.11: SEM images and EDS maps of fractured surface for as-received AA 6061-T651: (a) overview of fractured surface, (b, c, d) progressive high magnification images of selected fractured site, and (e)EDS map of fractured surface.

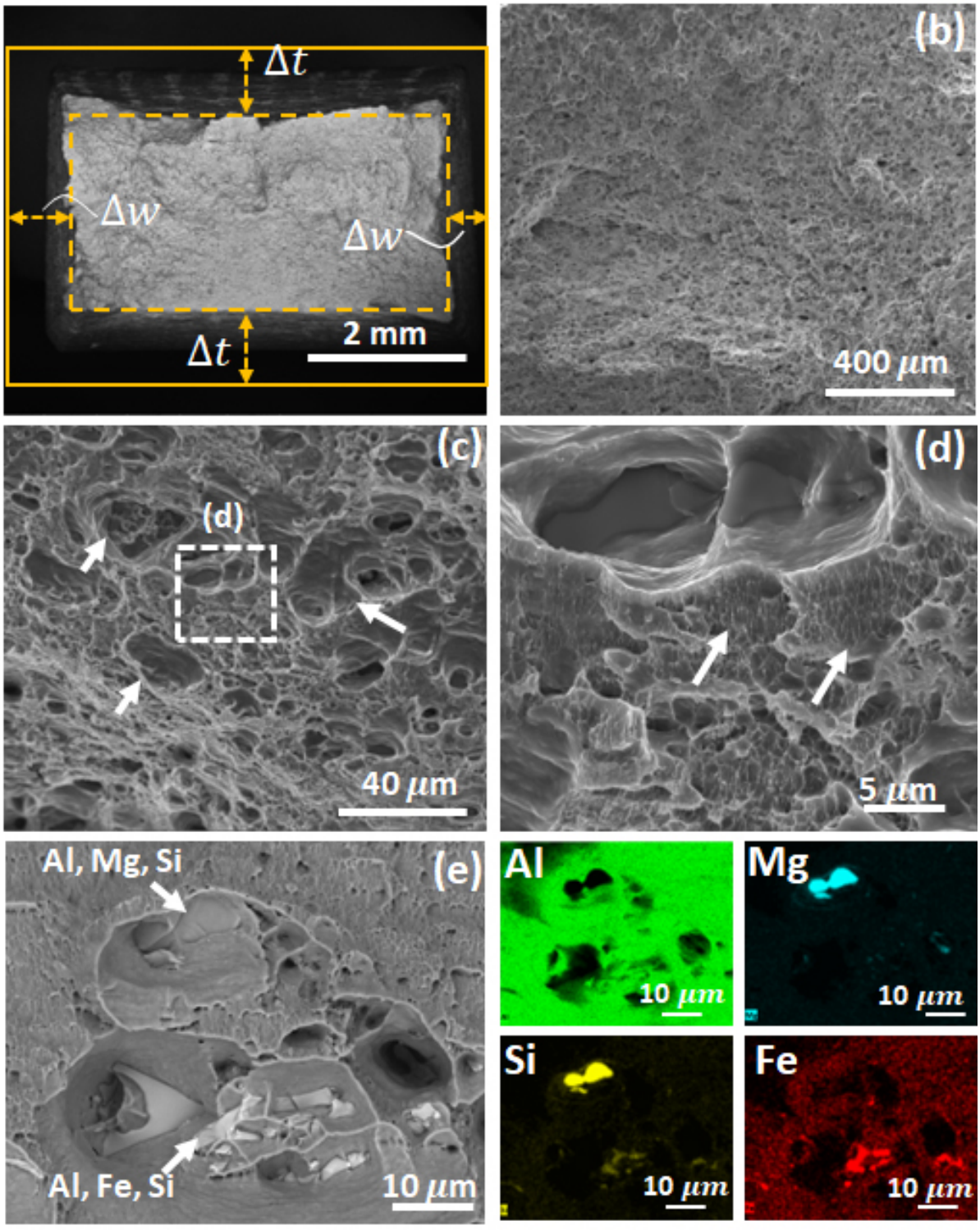

Figure 2.12: SEM images and EDS maps of fractured surface for TIG-welded AA 6061-T651: (a) overview of fractured surface, (b, c, d) progressive high magnification images of selected fractured site, and (e)EDS map of fractured surface. White arrows in (c) and (d) point at dimples and slip lines, respectively.

Figures 2.11b-d and 12b-d are progressive higher magnification micrographs of fractured surface in as-received and TIG welded samples, respectively, and they clearly show dimple rupture fracture mode which are characteristic of the ductile fracture [99]. Dimples form due to the coalescence of microvoids that nucleate at localized strain discontinuities like intermetallic, inclusions, dislocation pile-ups, and grain boundaries [105,106]. The strain discontinuities in this study are intermetallic (Al-Fe-Si and Al-Mg-Si phases), which are observed in Fig. 2.11e and 2.12e.

The equiaxed morphology of the dimples in both samples confirms the tensile load type—equiaxed dimples typically form under tensile load, in the condition of uniform plastic strain along tensile stress direction [106]. Even though fracture mode is somewhat similar in both materials, the as-received samples exhibit finer and deeper equiaxed dimples with fine ridges. On the other hand, the welded sample displays coarse and shallow dimples with a significant amount of slip lines arrowed in Fig. 2.12 c,d than in the as-received sample (Fig. 2.11 c, d). In a simplified manner, the size of these dimples can be used as a measure of ductility [107]: fine dimples are typically observed in high-strength materials, while low-strength materials exhibit coarse dimples [108]. Therefore, the high heat input of the welding process promotes the development of coarser dimples and extensive slip lines in HAZ2 of the TIG-welded sample, resulting in low yield strength.

2.4 Conclusion

In this work, we re-examined the origin of softening in TIG-welded heat-treatable AA 6061-T651 through a combination of experimental techniques, analytical modelling, and thermodynamic simulation, for a more comprehensive understanding of its (softening) evolution and impact on mechanical performance. Based on the results, the following conclusions can be drawn:

i. The weld contains a significant amount of pores, while material softening occurs in HAZ up to at least 38 mm away from the weld center.

ii. Based on peak temperature, associated hardness, and precipitate phases in these zones, HAZ partitions into four—HAZ1, HAZ2, HAZ3, and HAZ4.

iii. Average temperature and hardness compared to the unaffected base-material (120 HV) in these zones vary largely: HAZ1 (525 °C and 66-72 HV), HAZ2 (306 °C and 54-64 HV), HAZ3 (155 °C and 64-94 HV), and HAZ4 (79 °C and 95-106 HV).

iv. While the temperature rise induces solid solution and further precipitation of coherent GP zones in HAZ1, coarsening of the pre-existing precipitate occurs in HAZ2 (non-coherent/stable β-Mg2Si), HAZ3 (both semi-coherent/metastable β' and coherent/metastable β") and HAZ4 (coherent/metastable β") phase.

v. The mechanical tensile test shows that the TIG-welded sample fractures at the softest region—HAZ2, which is about 10 mm away from the weld center. The softening in TIG-welded sample (122.6 ± 1.7 MPa) in turn results in lower yield strength compared to the as-received sample (298 ± 1.5 MPa). Similarly, the impact toughness of TIG-welded alloy is 36 % lower than its as-received counterpart due to the welding-induced softening.

vi. XRM analysis confirms the presence of porosity in the welded area, and their mobility during plastic deformation so that the severity of softening has a significant influence on localized fracture than the presence of porosity in the weld area.

vii. Fractographic analyses revealed that high heat input in the conventional welding process and the induced softening of HAZ2 promotes the formation of coarser equiaxed

dimples and extensive slip lines that are signature of lower yield strength of the TIG-welded sample, compared to the as-received sample that constitutes finer dimples.

This work shows that conventional fusion welding process like TIG welding induces high heat input that causes both micro- (formation of micro-pores in the weld region) and nano- (dissolution, evolution, and over-aging of precipitates) structural changes in and around the weld area. This impact the mechanical performance of the welded components, and as such, new welding technologies that minimize these structural changes in base materials, especially precipitation-hardened alloys, should be sought.

Chapter: 3 Evaluation of cold spray for solid-state welding

Abstract

Welding is an important manufacturing process for joining complex parts. Despite their widespread use, there exist some drawbacks in the existing liquid-state (e.g., formation of undesirable heat-affected zones around weld area) and solid-state (e.g., high equipment and tooling costs, low production rates, and difficulty in joining intricate geometries) methods. These limitations continually spur the search for new joining processes to improve existing welding methods or develop new ones that circumvent these limitations. To provide a "greener" and low-cost alternative to the traditional welding processes that often produce "soft" heat affected zones (HAZs), we develop and evaluate the expansion of cold spray process—a solid-state high-velocity particle deposition process—to solid-state welding, a process we term "cold spray welding". Using well-defined processing parameters, we CSWed AA 6061-T651 plate and compared the results with Tungsten inert gas (TIG) welded counterpart. Although TIG-welded samples exhibit high tensile strength and impact toughness than CSWed samples (at least based on the CS processing parameters used in this study), our findings show that CSW indeed circumvents major drawbacks in traditional welding processes, including negligible microstructural alterations and the inhibition of deleterious phase transformation and suppression of deleterious HAZ. The examination of CSWed parts reveals lower tensile strength and impact toughness is connected to ubiquitous microvoids that are formed due to lack of metallurgical bonding; these microvoids act as microcracks initiation sites. We proceed to establish a failure mechanism in the CSWed part to provide direction for future optimization.

3.1 Introduction

Cold spray (CS) process is a solid-state layer-by-layer deposition process in which microparticles are accelerated to supersonic speed by pressurized gas; at a velocity above a critical threshold, the particles adhere to oppositely positioned substrate or previously deposited particles to form a coat or part [21,22,27,109–111]. Unlike other variants of thermal spray technology that rely on combustion and electric energies [112], the adhesion strength of launched particles in CS primarily relies on their (particles) kinetic energy. Similarly, while particles are melted in a thermal spray process, feedstock materials in CS remain at a much lower temperature than the melting temperature [113]; hence, the energy required in CS technology is significantly lower than the energy required in other thermal spray process [26]. Also, many defects associated with high-temperature thermal spraying, such as oxidation, structural and compositional changes, and tensile residual stresses can be circumvented by the CS process [21,23,112]. These advantages and the simplicity/propensity to extend of CS technology to uncharted applications in many fields have attracted the interests of scientists/researchers, and industrialists [21]. Traditionally, CS is used for *in situ* repair of cracks, tribological and antibacterial coatings, restoration/remanufacturing of unserviceable engineering/aeronautical components or corroded parts that are in service, and it can be used in a wide range of coating-substrate combinations [22,114–117]. This makes damaged parts reusable and in turn, saves the cost of buying new products [118].

The rapid development of modern manufacturing technology has recently expanded the application of CS from mainly a “coating technology” to an additive manufacturing (AM) technology [21]. While many commercial fusion-based AM technologies involve melting and final product degradation caused by high-temperature inputs [119], CS technology becomes a promising candidate in addressing these degradations [8,119]. Another common high-temperature

manufacturing process is welding—a material joining process where two or more materials are joined at their contacting surfaces using heat and/or pressure [3]. The strength of the welded joint is primarily determined by the extent of metallurgical bonding between the parts, which can be achieved through either fusion or diffusion process [44]. In fusion processes, metallurgical bonding is achieved via a liquid mechanism; the high heat involvement aids melting and fusion of the welded zone to the adjacent solid base region [120]. Like in the high-temperature thermal spray process, fusion welding accelerates oxidation, thermal defects, and distortion of welded parts [3,63]. Moreso, the thermal cycle from the weld center and away from it also induce microstructural changes, and in turn, the development of heat affected zone (HAZ) that significantly deteriorates the mechanical properties of the welded parts [3,56,86,99,121]. As such, post-processing heat treatments are often necessary to alleviate the deleterious effects of welding [51]. Meanwhile, solid-state welding processes such as friction stir welding form metallurgical bonding through the diffusion of interfacial atoms on the surfaces of contacting bodies, thereby avoiding the defects associated with material melting in a fusion-based process [122,123]. These processes can be limited by factors such as high equipment and tooling costs, low production rates, and limitations in joining intricate geometries [18]. Therefore, a significant industrial need is to develop a new welding process that is cost-effective and capable of joining complex geometry materials without undesired defects or the need for post-processing heat treatment.

CS technology may offer distinct advantages over conventional welding processes because of its (CS technology) ability to (i) deposit thick coating, (ii) develop components of complex geometry/3D shapes in a single step without high-temperature effects like oxidation, (iii) suppress unfavorable structural changes and HAZ formation, (iv) reduce production cost due to process flexibility and the absence of combustible/fume gases that also makes it a greener process, and (v)

retain properties of feedstock material after deposition [23,25,111]. Although there are very few reports on metal joining by CS technology [124–126], they are either of a double V bevel-shaped geometry that could be impractical for thin components and where there is no access for deposition from both sides of the welded components [124], or do not provide detailed report on important processing parameters such as bevel geometry [125,126]. This lack of details make repeatability difficult, and by extension, it frustrates the expansion of CS technology to welding application. As an important next step, we examine the solid-state welding process by CS technology and hereafter reserve the term—Cold Spray Welding (CSW)—for such a process. It is our goal to further explore the CSW as a potential replacement for the fusion-based welding process. As a starting point, we carefully design the welding geometry and process parameters, and conduct CSW of AA 6061-T651 plate followed by advanced materials characterization of welded samples. Finally, we made a comparative study of CSWed, and the Tungsten inert gas (TIG) welded samples to evaluate the potential and the current limitations of CSW, with the goal of future extensive optimization.

3.1 Experimental procedure

3.1.1 Materials and welding process

This study examines CSWed and TIG-welded AA 6061-T651 plates. The T651 temper condition refers to the history of the AA 6061 plate: it was solution heat-treated followed by artificial aging, and finally stress relief by stretching to 1.5 to 3 % [65]. The as-received plates were machined to the dimension of 200 x 55 x 6 mm (length x width x thickness) for each side of the samples, as shown in Fig. 3.1a and b. 6061 aluminum alloy powder purchased from VALIMET, Inc (AM 6061) was used for CSW, while a filler wire ER-4043 with a diameter of 1.6 mm was used for the TIG

welding process. The chemical composition of the as-received plate, powder, and filler wire is provided in Table 3.1.

Table 3.1: Chemical composition of AA-6061-T651 plates, CSW AM 6061 powder and TIG welding filler wire Al-4043.

Element	Si	Mg	Fe	Cu	Mn	Cr	Zn	Ti	Be	Al
AA 6061-T651 plate	0.70	1.00	0.41	0.27	0.12	0.18	0.01	0.02	-	Bal.
AM 6061 powder	0.58	0.86	0.09	0.28	0.01	0.09	0.01	0.01	-	Bal.
ER-4043	5.00	-	0.20	0.03	-	0.09	0.01	-	0.00003	Bal.

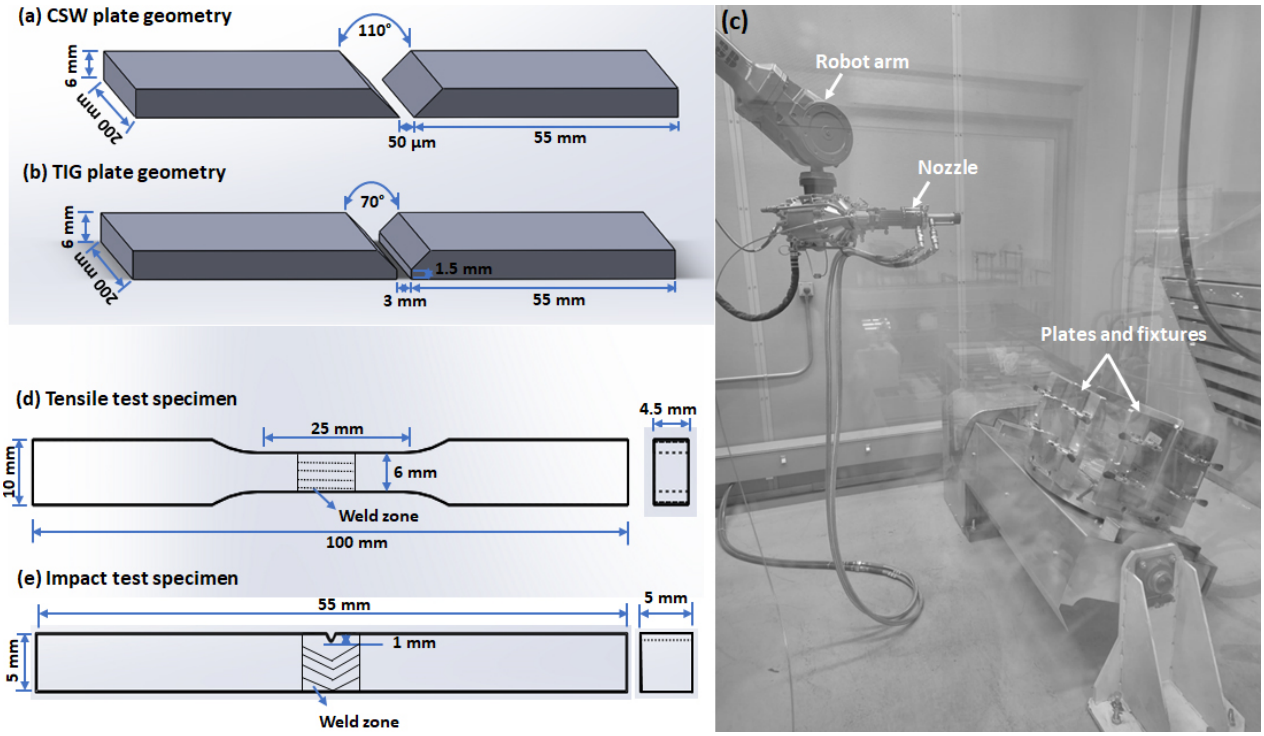

Figure 3.1: Geometry of AA 6061-T651 plates for (a) CSW, (b) TIG welding; (c) the high-pressure cold spray system and plates in fixtures, ready for CSW: and specimen geometry for (d) tensile and (e) impact tests. (b), (d), and (e) are adapted from Ref. [127].

Before welding, a single V-groove with a bevel of 55° (included angle: 110°) was machined on each plate for CSW. The bevel angle choice was determined from the work of Loke et al. [128]: they reported that the most cost-effective CS deposition of AA 6061 material occurs at spray angles larger than 50°. For TIG welding, a 35° groove (included angle: 70°) was machined on each plate. The geometry of plates for CSW and TIG welding are presented in Figs. 3.1a and b, respectively.

The root gap between CSW plates was set at 50 μm, and there was no root face. The root gap and root face for TIG welding plates were 3 mm and 1.5 mm, respectively.

The CSW was performed using a high-pressure CS system, manufactured by Impact Innovative, model ISS 5/11, the robot arm-nozzle-sample fixture setup is presented in Fig. 3.1c. The CSW parameters were selected based parameters in Ref. [129], where AA 6061 powders were successfully deposited on an AA 6061 substrate using helium as the carrier gas. In our case, we opted for higher gas pressure and temperature to achieve similar particle velocity in that work [129]. TIG welding was carried out manually using argon shielding gas and a 2 % thoriated non-consumable electrode. CSW and TIG welding parameters are presented in Table 3.2.

Table 3.2: CSW and TIG welding parameters.

CSW	**Process gas**	**Gas temperature**	**Gas pressure**	**Stand-off distance**
	N_2	450 °C	30 bars	25 mm
TIG	Current	Voltage	Travel speed	Argon flow
	220 A	15 V	152.4 mm. m^{-1}	18 cfh

3.1.2 Microstructural and mechanical characterization

The samples for microstructural analysis were prepared following the standard metallographic procedures in ASTM E3-11 (2017) [66]. This was followed by 2 hours of polishing using a Buehler VibroMet™ 2 Vibratory Polisher at a vibration amplitude of 20 %; 0.025 μm colloidal silica was used as the polishing solution. Samples were etched with Keller's reagent for 1 minute. The grain size of the as-received AA 6061-T651 plate was determined from optical images (using Lecia DM6000M microscope), and calculations followed the ASTM E112-13 standard [67]. Cross-sectional milling of the cold spray weldment was done using Leica TIC 3X Ion Beam Milling System with standard stage, argon as the working gas, an accelerating voltage of 8 kV, gun current of 3 mA, and a processing time of 4 hours. Both scanning electron microscopic (SEM) and energy

dispersive x-ray spectroscopic (EDS) examinations on un-etched samples were conducted using a Bruker Nano GmbH in Berlin, Germany, equipped with an Xflash 5030 detector. The SEM was operated at 15 keV, and two detectors were used—backscattered electron detector (BSED) and Everhart-Thornley Detector (ETD).

The microhardness test was conducted using a Buehler Wilson® Tukon™ 1202 digital Vickers hardness tester, following the guidelines of ASTM E92-17 [130]. The applied load was set to 300 gf, and the holding time was 10 seconds. The spacing between indents both horizontally and vertically was 1 mm. Tensile tests were performed on the as-received, CSWed, and TIG-welded samples using a Tinius Olsen universal testing machine (H25KS model). The test procedure and sample dimensions (Fig. 3.1d) were according to the specifications of ASTM E8/E8M-21 [68]. The tensile test was conducted with a crosshead speed of 1.25 $mm.min^{-1}$ and a corresponding strain rate of 0.05 min^{-1} (8.3×10^{-4} s^{-1}). Impact testing was conducted on the as-received, CSWed, and TIG-welded samples using an Amsler Otto Wolpert-Werke GMBH D-6700 impact tester with a capacity of 4 J. The test was performed in a Charpy mode following the guidelines of ASTM E23-18 [69]. The impact test sample dimensions are illustrated in Fig. 3.1e, and the test was performed at a velocity of 3 $m.s^{-1}$. This study reports the average values obtained from three tensile and impact test measurements. All mechanical tests were performed at room temperature.

3.1.3 Thermodynamic modelling

The CALPHAD approach using the Thermo-Calc 2023a software is used for thermodynamic modelling. In this study, the phase diagram module, along with the TCAL8: Al-alloys V8.2 database, was used to calculate the volume fraction of present phases in as-received plate, powder for CS, and filler wire for TIG welding.

3.1.4 X-ray microscopic analysis

X-ray microscopic (XRM) analysis was conducted using the Xradia Versa XRM-520 machine to examine voids and porosity in CSWed and TIG welded samples, respectively. The XRM scans were performed with the following parameters: a source voltage of 160 kV, a current of 62 μA, and a power of 10 W. To ensure maximum area coverage, the scans were carried out with a pixel size of 25.24 μm. For detailed investigations, high-resolution (HR) images were obtained with a pixel size of 3.08 μm.

3.2 Result and Discussion

3.2.1 Microstructure of starting materials

The SEM images and EDS maps of the starting materials—AA 6061-T651 plates and powders—are presented in Fig. 3.2. The SEM-EDS maps in Fig. 3.2a show the base material constitutes Al-Fe-Si- and Al-Mg-Si- rich intermetallic phases. Although the optical images are not shown here for brevity, the grain size of the as-received AA 6061-T651 plate is 53 ± 4 μm. The as-received microparticles for CSW are fairly spherical with an average size of 24 ± 9 μm, as shown in Figs. 3.2b and c; notably, Fig. 3.2c shows the cellular structures on the particle surface that are inherited from the rapid nucleation and solidification process during particle production by gas atomization. The cross-sectional images of the particles show no evidence of voids/pores or grain interior second phase (Figs. 3.2d and e). The EDS spectra for matrix and phase in Fig. 3.2e and inset further confirm the presence of Al, Mg, and Si as the main constituents of the powder material, along with other trace elements in the GB phase region. The thermodynamic phase equilibrium diagrams in Fig. 3.3 confirm the presence of stable Mg_2Si-C1 precipitates in plate and particles (Figs. 3.3a and

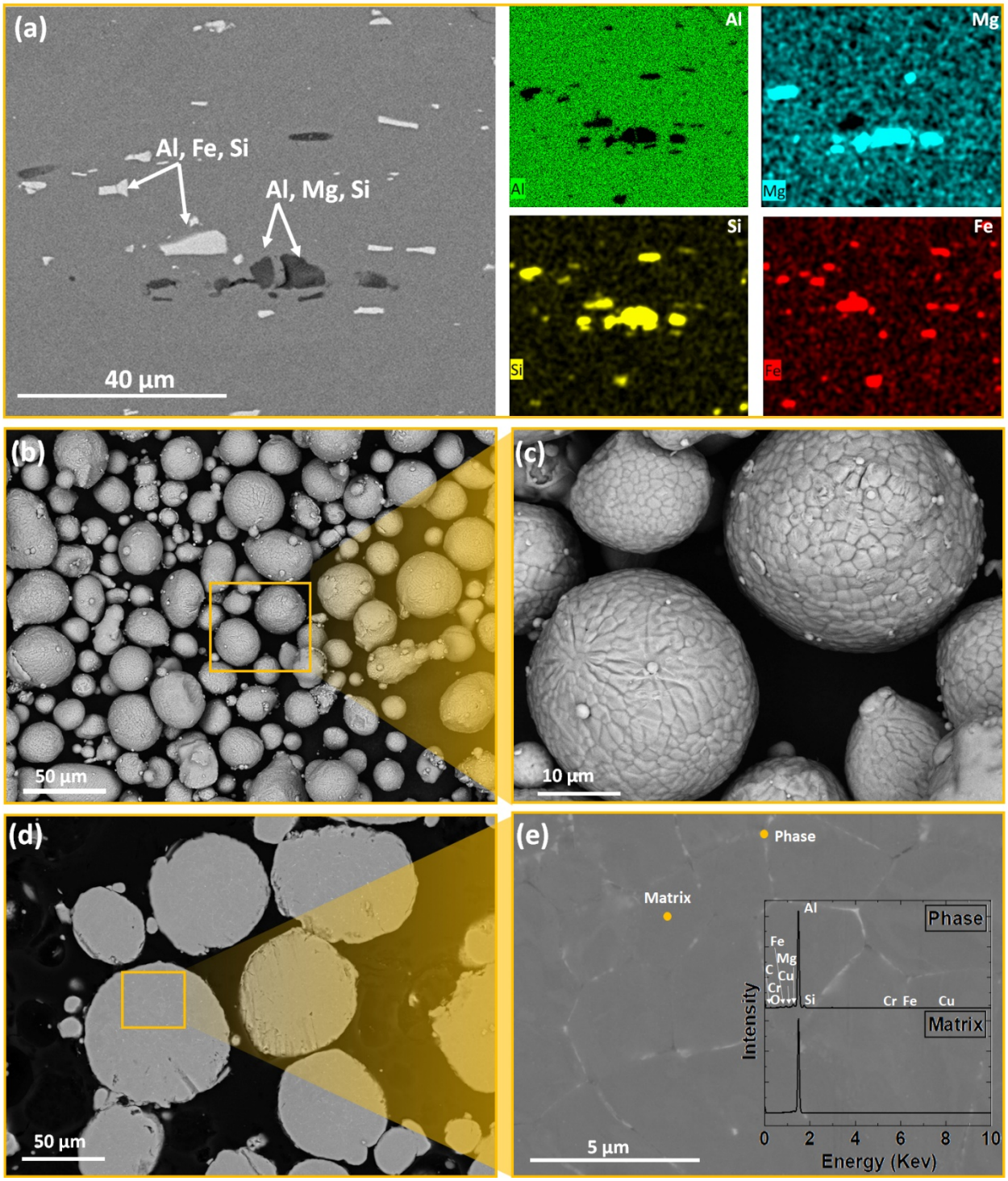

Figure 3.2: (a) EDS maps of base material; SEM BSED Images of AM 6061 powder showing (b, c) spherical morphology, and (d, e) grains and GB phases. The inset in (e) is the EDS spectra of the points in the SEM image.

b); this is a well-established precipitate in α- Al matrix of AA 6061, and the extent of strength contribution depends on their morphology and coherency with the matrix [59,131]. Similarly, the

stable $Al_9Fe_2Si_2$ intermetallic phase in the plates, as confirmed by the EDS maps, and filler wire (Figs. 3.3a and c) align with the phase reported in Ref. [78].

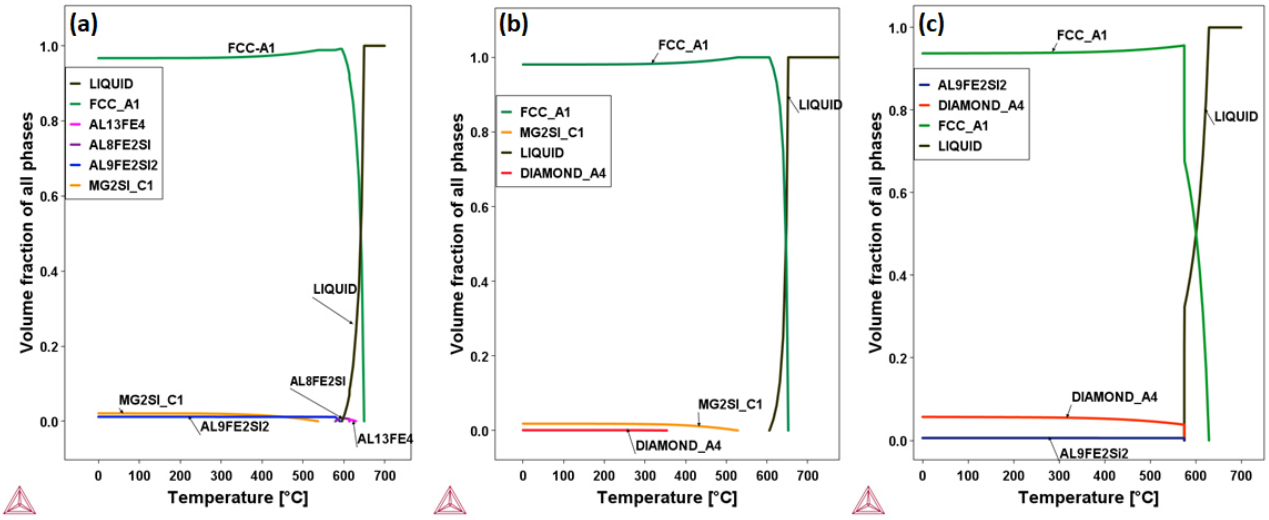

Figure 3.3: Thermo-Calc equilibrium solidification diagrams showing the volume fraction of phases at different temperatures for (a) base material with composition Mg: 1%, Si: 0.70%, Fe: 0.41%, Al: bal., (b) AM 6061 powder with composition Mg: 0.86%, Si: 0.58%, Al: bal., and (c) filler wire with composition Si: 5%, Fe: 0.20%, Al: Balance.

3.2.2 Bonding and microstructural assessment of cold spray welded samples

In CS, the bonding between particle-particle or particle-substrate is achieved by either mechanical interlocking (physical trapping of particles without interfacial chemical bond) and/or metallurgical bonding (new formation of interfacial chemical bonds) [25]. Generally, successful particle bonding which occurs at and above sufficiently high impact velocity threshold, commonly referred to as critical velocity, v_{cr}, requires localized plastic deformation and adiabatic shear instabilities [32]. On the processing side, particle impact velocity can be influenced by many factors, including; gas pressure and temperature, nozzle geometries, powder feeding rate [32], and atomic mass of driving gas [26]. However, powder and substrate characteristics such as crystal structure, yield strength, density, melting point, oxygen content, and surface oxides can affect v_{cr}, and in turn, the onset of

bonding [22,26,35]. In what follows, we evaluate bonding and microstructural changes that set on during CSW.

3.2.2.1 Scanning electron microscopic and energy dispersive x-ray spectroscopic analyses: Particle plasticity and formation of deleterious microvoids.

To assess the inter-particle and particle-substrate bonding, the overview of the CSWed sample showing the weld area and adjacent AA 6061-T651 base is presented in Fig. 3.4a. While the base shows a low grey scale of darker contrast, the CSWed region shows a high grey scale of brighter contrast, the boundaries of which denote clear base-weld interfaces. High magnification BSED images of the base-weld area in Fig. 3.4b-d shows dark lines or areas that are signature of a lack of metallurgical bonding at the base-weld boundaries (indicated by yellow arrows in Fig. 3.4c), and particle-particle boundaries (indicated by red arrows in Fig. 3.4c). Other variants of particle-particle boundaries shows no evidence of bonding; these are "triple junctions"—lack of bonding at the point where three particles, 1, 2, 3, ought to meet (right side of Figs. 3.4d and e) and "quadruple point"—lack of bonding at the point where four particles, 1, 2, 3, 4, ought to meet (inset in Fig. 3.4b and the left side of Figs. 4d and e). It is the triple junctions and quadrable points that result in voids formation in the CSWed, since there is a near-absence of voids in the pre-deposited particle interior (Figs. 3.2d and e).

The EDS maps of the base-weld areas in Fig. 3.4f show the presence of Al-Mg-Si and Al-Fi-Si phases in the base area and near homogenous phase of the weld area, which are unchanged in comparison with the starting microstructure before CSW (Fig. 3.2). This underscores the advantage of CSW over fusion-based welding where there is a mismatch between the microstructure of the weld area and the softened heat affected zone [57,98,132]. However, Al-O-rich regions are found mainly along the base-weld and inter-particle boundaries; these are native

oxide layers on the particles. In CS, this oxide layer on particles is considered as geometrical constraint to metallurgical bonding [23].

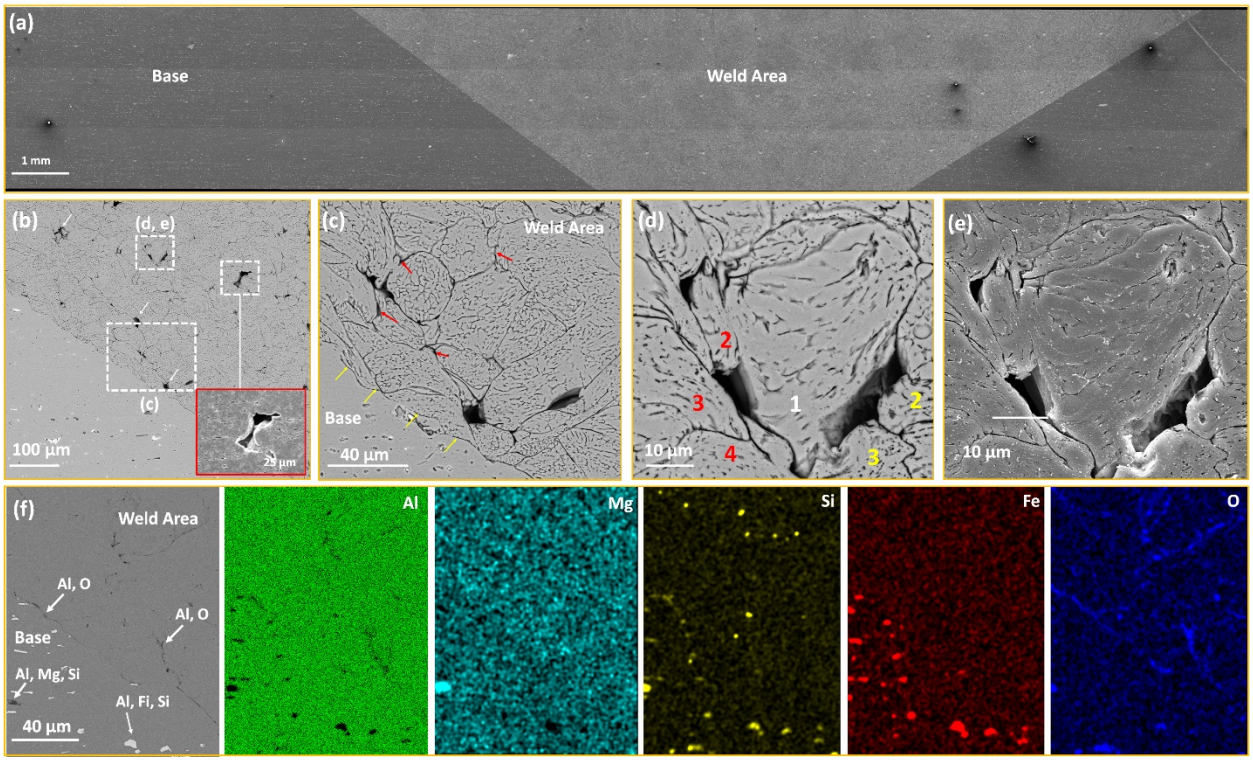

Figure 3.4: SEM images and EDS map analysis of CSWed AA 6061-T651 plate: (a) overview image of the welded sample, (b, c) images showing the weld area, weld-base interface (yellow arrows), and base area, (d, e) high magnification images of a selected weld area in (b), and (f) EDS maps of the weld and base areas. All SEM images are BSED, except in (e) that is ETD.

Previous work has shown that surface oxide delamination during the high-velocity microparticle impact process expends ~30% of the actual extra energy required for bonding so that the presence of surface oxides on particle slows the onset of jetting and metallurgical bonding [35]. The presence of an oxide layer increases the energy budget required to initiate clean metal-metal contact, therefore increasing v_{cr} [22,26]. Because of the variability of particle sizes, we posit that the kinetic energy of larger particles is sufficient to surpass their v_{cr}, i.e., the particles possess sufficient energy to break, delaminate, and expel surface oxides, and to induce jetting and bonding. Meanwhile, the kinetic energy of smaller particles may be insufficient to overcome such bonding

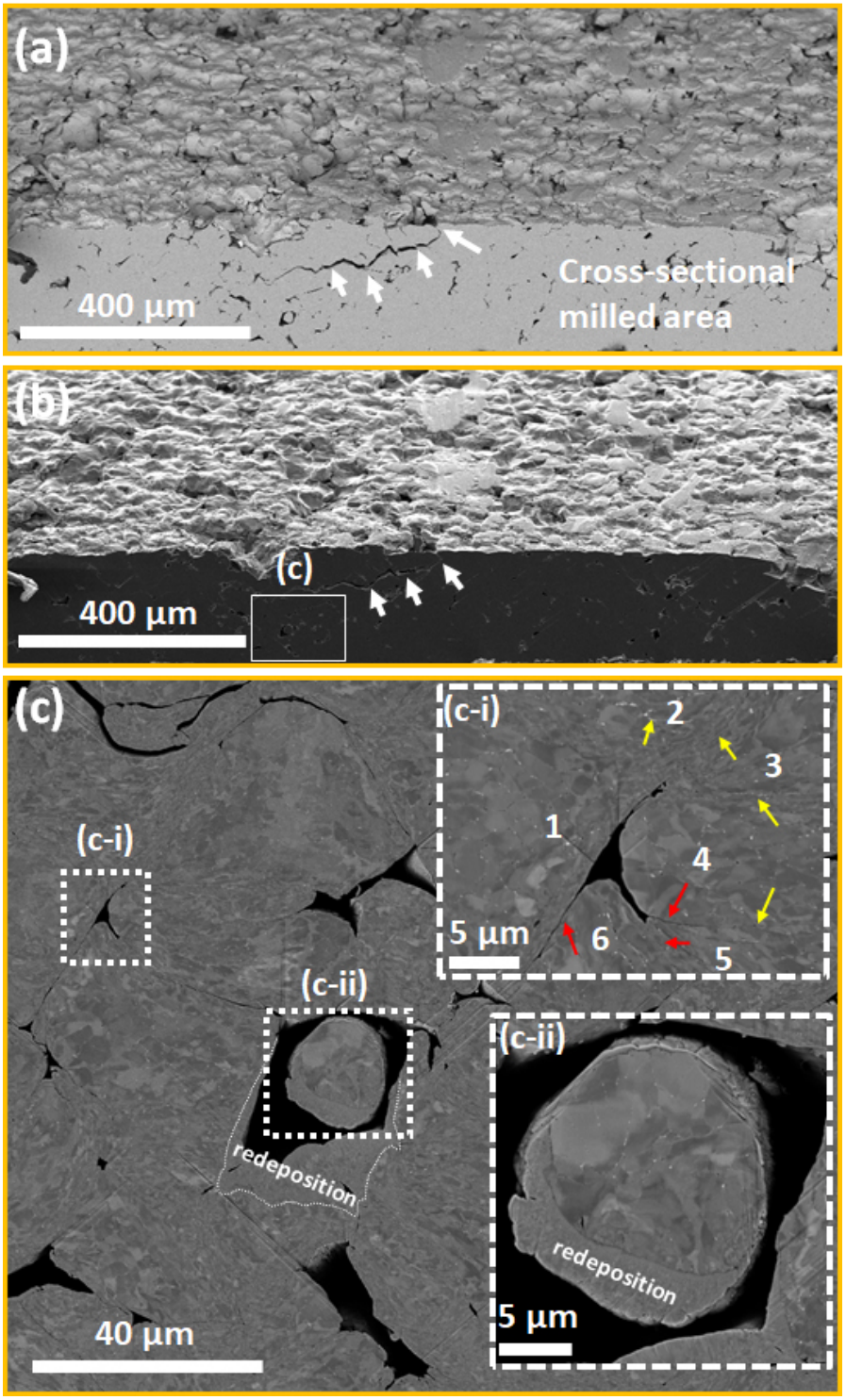

Figure 3.5: SEM images of the cross-sectional ion-milled CSWed sample at the weld area: (a, b) overview, and (c) high magnification image of the marked area in (b). (c-I and c-ii) show inter-particle bonding condition and an un-deformed void-filling microparticle, respectively. Yellow and red arrows in (c-1) point at metallurgical bonded and unbonded particle-particle interfaces, respectively. All SEM Images are BSED, except the ETD in (b).

barriers; they rather impinged and adhered with poor metallurgical bonding, as also reported in Ref. [133]. We, therefore, conclude that particle surface oxide can potentially constrain particle plastic flow to fill voids (Figs. 3.4d and e), inhibit metallurgical bonding, and in turn, increase v_{cr}.

Additionally, the SEM images of ion milled cross-section of the CSWed sample just at the weld area are presented in Fig. 3.5. Fig. 3.5(a, b) provides an overview, and it reveals the presence of a lateral crack (white arrows) that originates from a void and propagates up to a substantially long distance. This shows that the presence of voids can be a crack initiation site in CSWed parts. A progressive high-magnification BSED image of the cross-sectioned area presented in Fig. 3.5c reveals the presence of voids, bonding, and lack of bonding between particles. Fig. 3.5c-i shows metallurgical bonding exists at severely deformed particle-particle interfaces (indicated by yellow arrows at particles 1-2, 2-3, 3-4, and 4-5 interfaces), while unbonded regions that leads to the formation of voids occur at less plastically-deformed interparticle interfaces (indicated by red arrows at particles 4-5, 5-6, and 6-1 interfaces). Notably, Fig. 3.5c-ii shows a finer microparticle (~10 μm) that is largely undeformed but trapped within a large void created by larger particles. While this is undesirable, this void-filling by smaller particles can improve the stacking density of the metallic powders within the weld area as is the case in liquid-state additive manufacturing process [134-36]; this can potentially improve the mechanical performance of the CSWed parts, but it remains open for further investigation.

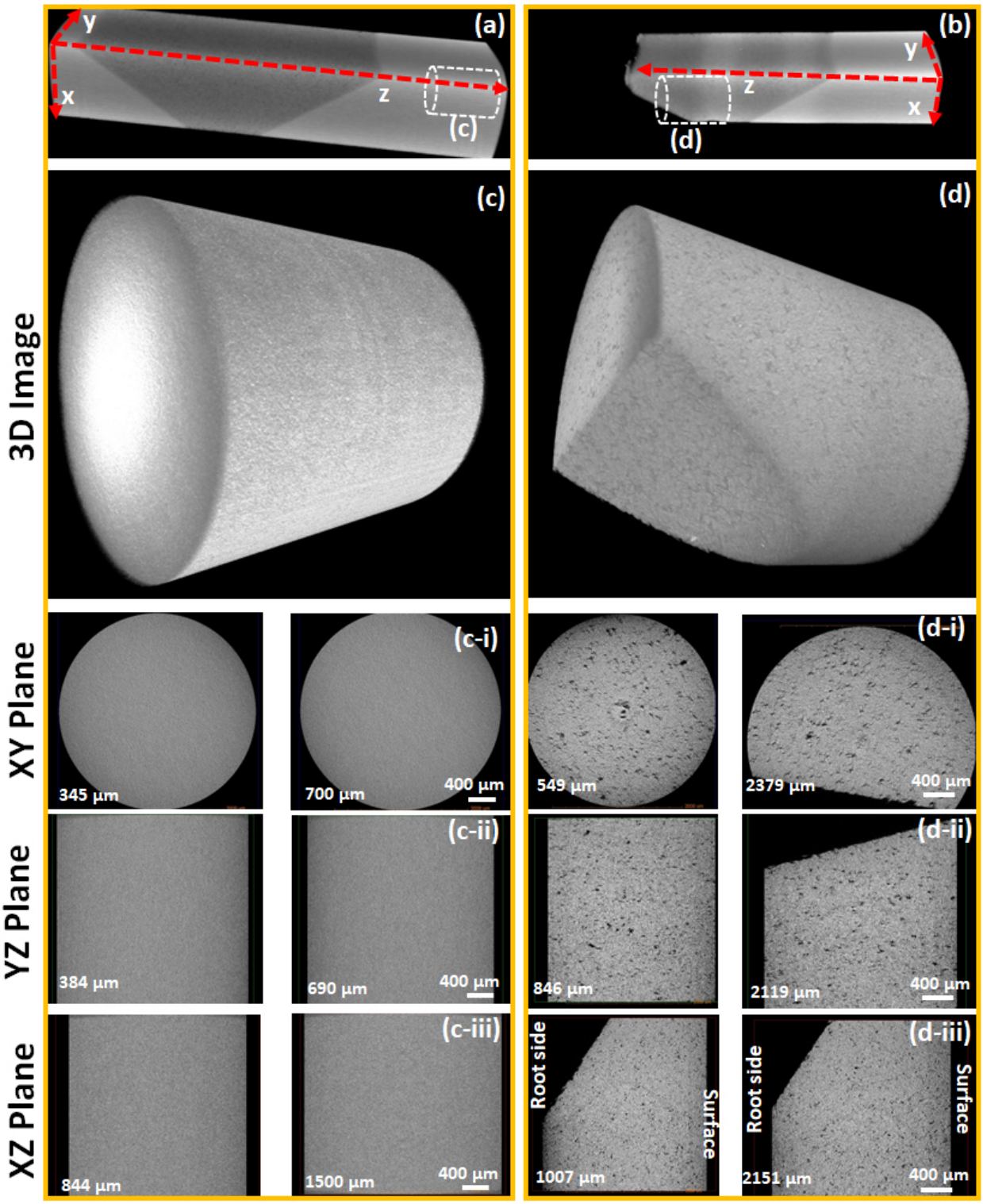

Figure 3.6: (a, b) Low and (c, d) high resolution XRM images of CSWed sample: (a, b) overview, (c) 3D image of base and corresponding 2D slices on XY, YZ, and XZ planes, (d) 3D Images of welded area and corresponding slices on XY, YZ, and XZ planes.

3.2.2.2 X-Ray microscopic analysis: Evaluation of void distribution and tamping effect in the weld area.

As earlier established, CS is a layer-by-layer deposition process [27], and there are steps to coat formation: (i) substrate cratering and first layer build-up, (ii) deformation and realignment of impinging particles, (iii) formation of metallic bond and reduction of voids, and (iv) further coating densification and compaction [137,138]. Like the factors that affect v_{cr} highlighted earlier, several factors also influence the requirements to achieve these steps, such as density, yield strength [26,34], and the presence of an oxide layer [31]. These factors can either accelerate or impede the deformation of particles, which in turn affects the extent of flattening and the filling of voids by deformed particle lips. In the current study, XRM is used to assess the presence and extent of voids in the CSWed area in comparison with the base materials, as shown in Fig. 3.6. The 3D HR-XRM image of the base area shows nearly homogenized void-free volume (Fig. 3.6c), while that of the weld area shows a rough surface that is signature of lack of particle adhesion and is throughout the volume (Fig. 3.6d). The 2D slices of the 3D HR-XRM images for the base in Fig. 3.6c (i-iii) at different locations further confirms the homogenized and pores-free volume, while ubiquitous the presence of dark low-density spots—voids—can be decerned throughout the weld area in Fig. 3.6d (i- iii). Furthermore, an observation can be made from the weld cross section in Fig. 3.6d (iii): away from the bottom weld near the root gap towards the surface, an increase in voids (dark low-density spots) can be discerned. The less compact of the top layer of CS deposit compared to the bottom layer has been reported by Silva et al. [139]: the previously deposited layer is further impacted by incoming particles, resulting in the densification of the previously deposited material [21]. This behavior is called the tamping effect [140], and it occurs in the CS weld area.

3.2.3 Comparison of solid-state CSWed and liquid-state TIG-welded parts.

The choice to compare solid-state CSW with the liquid-state TIG welding process is driven by the limitations of existing liquid-state welding techniques that accelerate oxidation, induce thermal defects, distort welded parts, and result in inhomogeneous microstructural changes, i.e., formation of soft HAZ. Despite these limitations, liquid-state fusion welding remains an indispensable joining method [57], and in fact, industries find the method to be more versatile with high productivity [63].

3.2.3.1 Microstructural assessment of TIG-welded samples

In what follows, we assess the microstructural changes in TIG-welded sample in comparison with those of CSWed parts. The overview of the TIG-welded sample in Fig. 3.7a shows the weld and the adjacent HAZ that is the weakest area where failure would typically occur under external loading conditions [86,99,97]. High magnification images in Figs. 3.7(b-d) show various microstructural features: dendritic structure at the weld area, the fusion line, and the second phase particle identified by EDS analysis as Al-Si, Al-Mg-Si, and Al-Fe-Si in Fig. 3.7e and f. In our previous work [127] and other works [88,86], we showed that the HAZ experienced high-temperature rise and phase transformation as the sample cools away from the weld area. This partitions the HAZ area into subzones as the existing coherent/metastable β" precipitates in the HAZ area respond to different peak temperatures: HAZ 1 transform into coherent GP zones, HAZ2 into non-coherent/stable β-Mg_2Si), HAZ3 into both semi-coherent/metastable β' and coherent/metastable β", and HAZ4 into coherent/metastable β" phase [127].

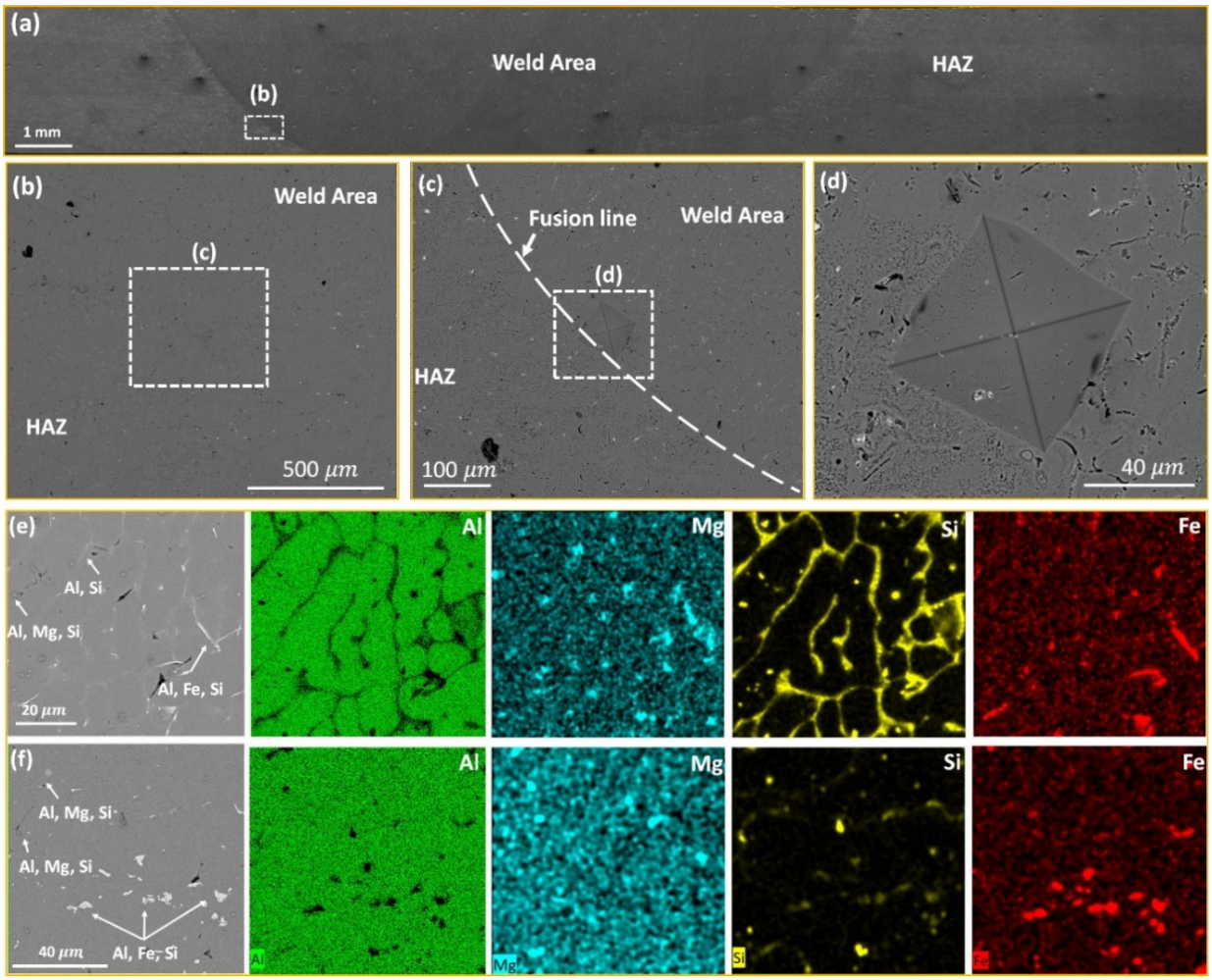

Figure 3.7: (a-d) SEM images and (e, f) EDS maps of TIG-welded AA 6061-T651 plate: (a) overview, (b-d) progressive high magnification images showing weld area, fusion line and HAZ, (e, f) EDS map of the weld area and HAZ, respectively. SEM images in (a) and (b-d) are ETD and BSED, respectively.

One promising solution to limiting such deleterious phase transformation and enhancing weld quality is the suppression of excessive heat input [13]. Low heat input joining methods have been suggested as potential candidates [141], and CSW would be a suitable option for joining such temperature-sensitive materials. Additionally, the XRM was used to analyze the TIG-welded tensile sample, and the results are presented in Fig. 3.8, in comparison with the CSWed joint in Figs. 3.6b, d. The overview of the sample in Fig. 3.8a shows the TIG-welded area has a darker contrast compared to the adjacent base. While the HR-XRM images of CSWed joint in Figs. 3.6d

show evidence of voids due to poor particle metallurgical bonding, those of the TIG weld area reveal the presence of porosity, as shown in Fig. 3.8b. The 2D image slices in Fig. 3.8c (i-iii) at different locations of the weld area further confirmed the homogenous distribution of the pores throughout the weld. The occurrence of porosity can be attributed to the elevated temperature involved in the welding process [8], resulting in the evaporation of elements with lower vapor pressure [76,62]. This behavior pores formation in TIG—highlight the advantage of the CSW process if the lack of metallurgical bonding that forms voids is suppressed: it (CSW) does not involve high temperature and melting, effectively suppressing the chances of pore formation.

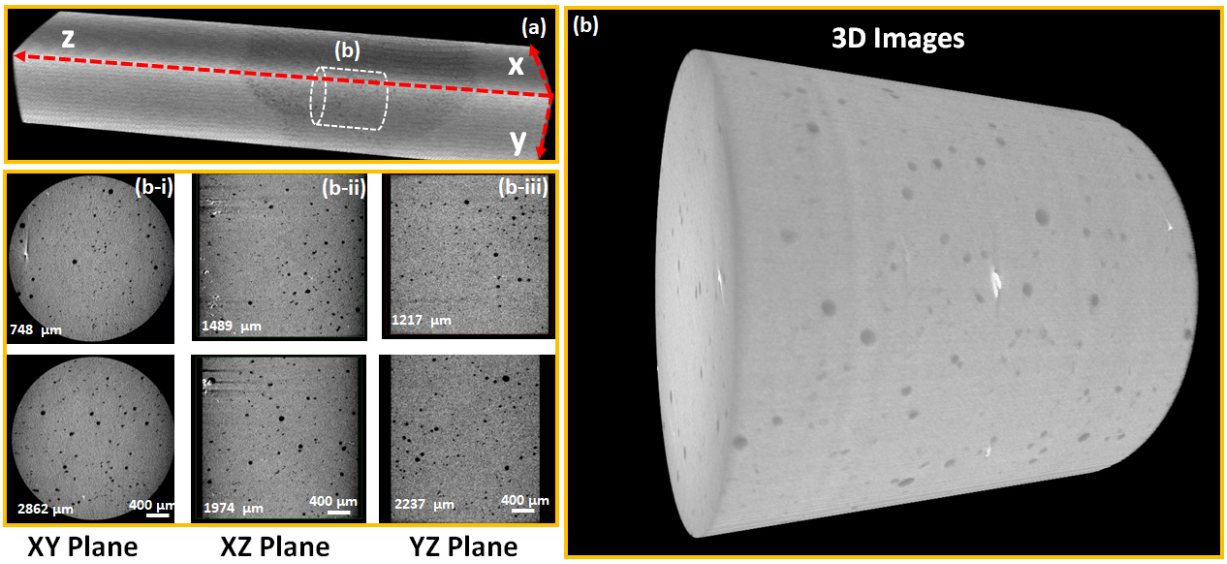

Figure 3.8: Low and high resolution XRM images of the untested TIG-welded tensile test sample: (a) overview, (b) 3D image of welded area marked area in (a) and corresponding 2D slices in XY, XZ and YZ planes. Adapted from [127], for completeness.

Therefore, improving interparticle and particle-substrate bonding will ultimately enhance the quality of the CSWed parts. Whichever joining method is used, the final microstructure after welding will impact mechanical performance, and in what follows, we evaluate and compare the mechanical performance of as-received, CSWed, and TIG-welded AA 6061-T651.

3.2.3.2 Mechanical properties of CSWed and TIG welded samples

To evaluate the mechanical behavior of as-received, CSWed, and TIG-welded parts, different tests (hardness, tensile and impact) were carried out and compared. The hardness result of the CSWed sample from weld center to both sides of the weld-base interface is presented in Fig. 3.9a: the weld area (70 - 104 HV) exhibits lower hardness than the surrounding base (113 - 122 HV) with fairly uniform hardness. These hardness values are close to what is reported for AA 6061 CS deposit (105 HV) and rolled AA 6061-T6 (107 HV) [142]. Comparatively, the hardness result of TIG-welded AA 6061-T651 sample in Fig. 3.9b indicates a very low hardness range (50 -70 HV) in the weld area, which extends towards the HAZs; the hardness range is lower than the base and the CS

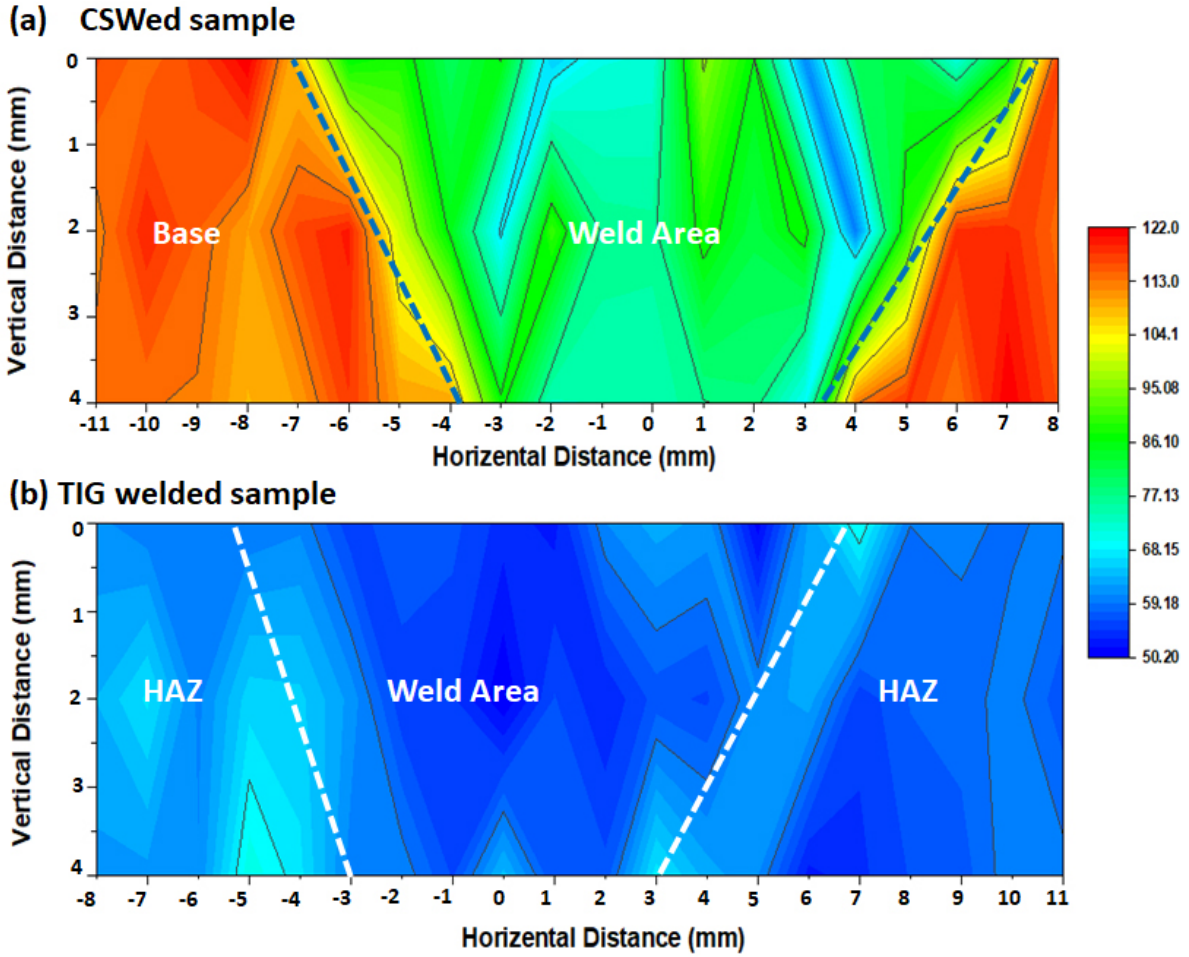

Figure 3.9: Hardness contour maps of (a) CSWed sample, (b) TIG-welded sample. The color legend values are in HV.

weld area. There is a non-uniformity of hardness in the HAZ area that also extend beyond what is seen in Fig. 3.9b, in fact, up to ~40 mm away from the weld center, thus partitioning the HAZ into subzones as highlighted in our previous work [127], and other fusion-welded components in Refs. [88,143,48]. The high heat input associated with the fusion welding process is responsible for the microstructural alteration, which directly affects the mechanical properties of the material [86].Specifically, age-hardenable alloys are more prone to these microstructural alterations during the fusion welding process [57,10]: existing coherent precipitates in base materials can coarsen and/or dissolve [62]. As a result, fusion-welded components often experience significant softening in the HAZ area. In contrast, the hardness result of the CSWed sample (Fig. 3.9a) does not show such softening phenomenon. Just after the weld-base interface, the material maintains the hardness of the as-received material (120 ± 4 HV). Alongside other advantages, the lower temperature requirement for CSW can minimize or eliminate the presence of the HAZ [144]. To analyze the behavior of CSWed parts under uniaxial load and impact, tensile and impact tests were conducted and compared with the as-received and TIG-welded samples.

Fig. 3.10a shows typical true stress-strain curves: it generally shows that the as-received and TIG-welded samples failed after a significant amount of plasticity, while the CSWed sample failed at very low stress and strain. The summarized results of the tensile tests are presented in Fig. 3.10b: the as-received sample exhibits higher yield strength of 298 ± 1.5 MPa and yield strain of 7.02 ± 0.02 % than those of TIG-welded (122.6 ± 1.7 MPa and 4.3 ± 0.18 %) and CSWed samples (24.17 ± 1.47 MPa and 0.41 ± 0.01 %), respectively. Similarly, the as-received sample exhibits a higher tensile strength of 363 ±1 MPa and tensile strain of 17.83 ± 0.23 % than those of TIG-welded (182 ± 1.2 MPa and 12.09 ± 0.26 %) and CSWed samples (30 ± 2.9 MPa and 0.82 ± 0.24 %), respectively. Furthermore, the Charpy impact test results in Fig. 3.10c show that the as-received

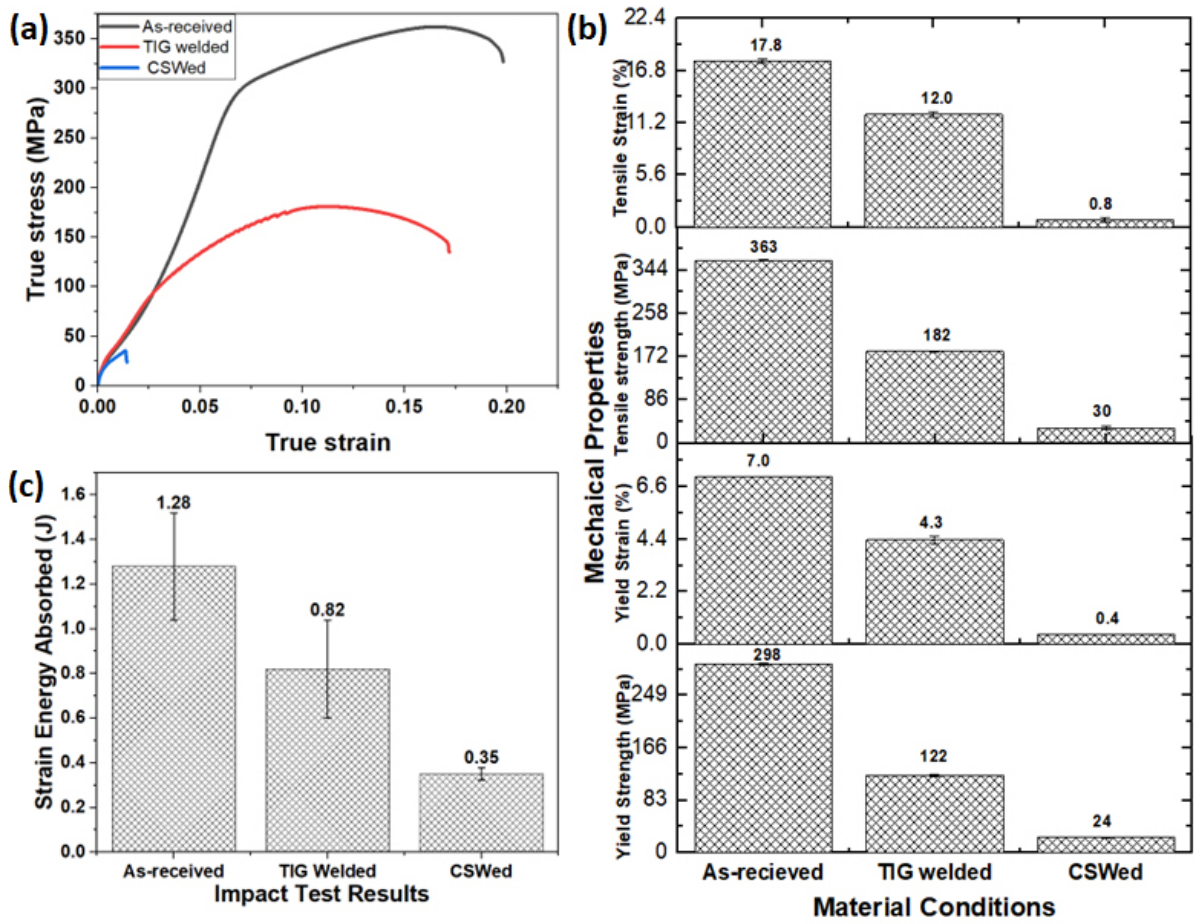

Figure 3.10: Mechanical test results for as-received, TIG-welded and CSWed sample: (a) true stress-strain curves and (b) extracted mechanical properties from the tensile test, and (c) strain energy absorbed during the impact test.

sample failed after absorbing 1.28 ±0.24 J of energy. The TIG-welded sample absorbed 0.82 ± 0.22 J, while the CSWed sample failed after absorbing 0.35 ± 0.02 J of energy. The results indicate that the impact toughness of TIG-welded and CSWed samples are 36 % and 73 % lower than the as-received sample. Consequently, the TIG-welded samples show better tensile and impact properties compared to the CSWed sample.

While the CSWed sample eventually fractured in the weld area but near the groove face (Fig. 3.6b), the XRM images of the TIG-welded tensile sample revealed failure within the HAZ area at ~10 mm away from the weld center, as shown in Fig. 3.11a; this underscores the role of the HAZ on the mechanical performance of TIG-welded samples. HR-XRM images taken from the weld area

show the signature of pore closure (Fig. 3.11b) compared to the pre-tested sample (Fig. 3.8b); as a note, the same TIG-welded sample was analyzed in Figs. 3.8 and 11. This observation (pore closure) is further supported by 2D slices in Fig. 3.11b (i-iii) taken at different locations compared to Fig. 3.8b (i-iii).

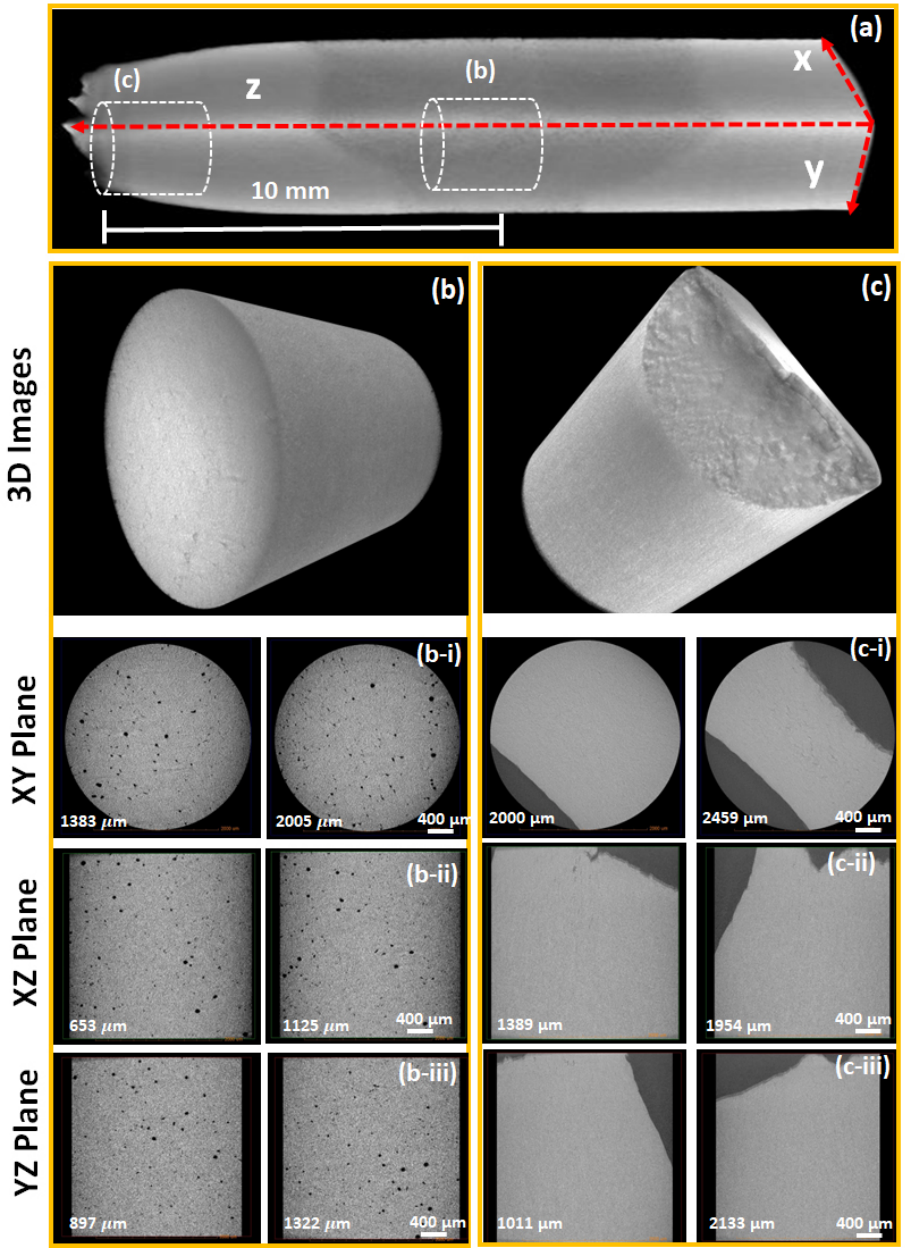

Figure 3.11: Low and high resolution XRM images of the TIG-welded tensile tested sample: (a) overview, (b)3D image of tensile tested weld area and corresponding 2D slices in XY, XZ and YZ planes, and (c) 3D images of the fractured area and corresponding 2D slices in XY, XZ and YZ planes. (c) is adapted from Ref. [127], for completeness.

We report in our previous work that during tensile testing, the presence of pores may require some energy for closure, consequently reducing the available stress to deform the weld zone compared to other neighboring HAZs [127]. This subsequently "transfers" the failure region to a pore-free softer zone—HAZ, as shown in HR-XRM 3D images in Fig. 3.11c, and corresponding 2D slices in Fig. 3.11c (i-iii).

To summarize, while the low strength and ductility in CSWed samples raise concerns and limitations for potential future expansion of the CS process to welding of engineering components and assemblies where these properties are desirable, it also provides an interesting area for future exploration. For instance, the ductility deficiency in the CSWed sample could be attributed to the severe cold working that occurs during the CS process and can be addressed by a post-CSW heat treatment that improves metallurgical bonding, as recently reported for a CS deposit [129]. Other recent works also show that higher mechanical properties can be obtained in CS 6061 deposit than the rolled plate AA 6061-T6 [129,142]. Unlike conventional CS deposits where particles are mostly normal to the substrate, we posit that the variable particle impact angle from the weld center to the groove face in a CSW case may result in low bond quality near the grove face so that it becomes the likeliest region of failure. This requires further investigation to explore and enhance the feasibility of CSW for industrial application, but as a starting point, we assess the fractured tensile samples in what follows.

3.2.3.3 Fractographic Analyses and mechanism of fracture of tensile-tested CSWed sample

Comparative fractographic analyses of the tensile-tested as-received, CSWed and TIG-welded samples were conducted to obtain a comprehensive understanding of their deformation and fracture behavior. First, we provide the fractographic images and a brief fracture mode overview

of the tensile-tested as-received and TIG-welded samples in Fig. 3.12. As seen in Figs. 3.12a and d, there is a significant thickness reduction in TIG-welded sample due to the localized softening in the HAZ where failure and fracture occur. Furthermore, both as-received (Figs. 3.12a-c) and TIG-welded (Figs. 3.12d-f) fractured samples show the equiaxed dimple signatures that are features of the ductile fracture [145]; albeit, the dimples in TIG-welded sample are coarser. It is established that finer dimple size correlates with higher mechanical strength [146] which explains the higher strength recorded for the as-received sample than that of the TIG-welded in Fig. 3.10a. These dimples evolve when microvoids (site inset in c) that nucleate at localized strain discontinuities coalescence [105,106]. More details about the fracture behavior of as-received and TIG-welded samples can be found in Ref. [127].

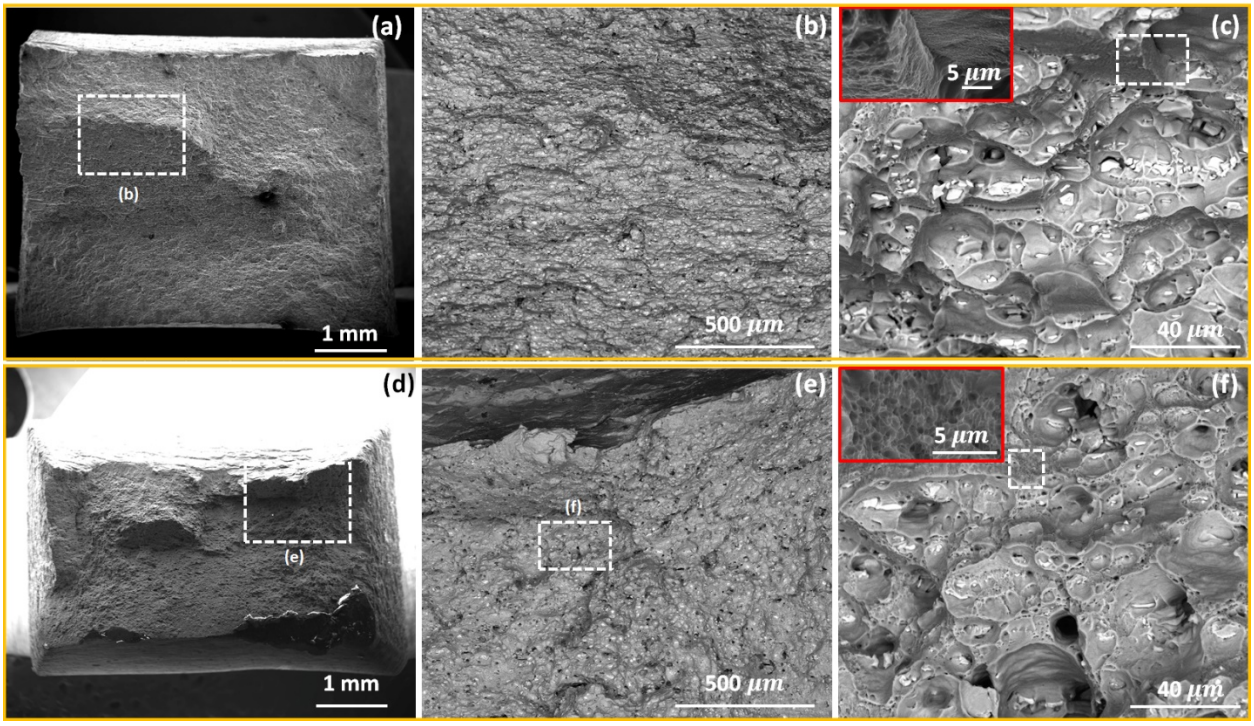

Figure 3.12: SEM images of fractured surface for (a-c) as-received and (d-f) TIG welded AA 6061-T651: (a,d) overview, and (b,c and e,f) progressive high-magnification images of selected fractured sites. Insets in (c and f) are marked area in white rectangles. All images are BSED except for those in (a, d) and inset in (c, f) that are ETD.

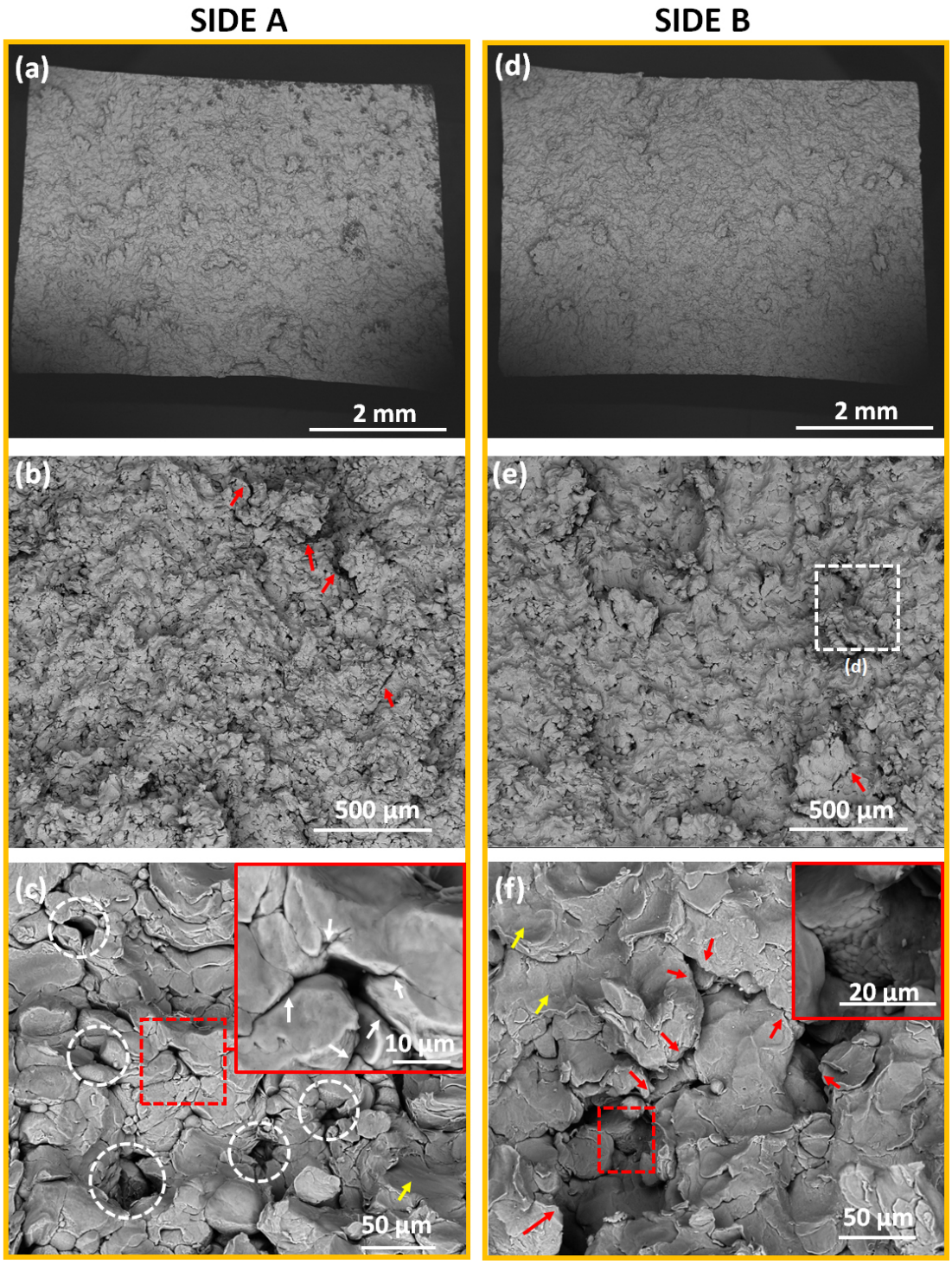

Figure 3.13: SEM BSED images of fractured surface of tensile tested CSWed AA 6061-T651 sample for sides (a-c) A and (d-f) B: (a,d) overview and (b,c and e,f) progressive high magnification images of selected locations; the insets in (c and f) are marked areas in red dashed-rectangles; yellow arrows point at splats and initially bonded area; red arrows show lack of bonding in (b and e) and crack paths connecting microvoids in (f); white arrows show crack propagation from microvoids in (c); and white circles show the location of crack-initiating microvoids in (c).

In contrast, Figs. 3.13a-c and d-f provide a surface overview of both sides, A and B, of the fractured tensile-tested CSWed sample, respectively. The fractographs show evidence of deposited microparticles on both sides: some particles bonded with each other to form agglomerates, and a lack of bonding with other neighboring bonded particles (red arrows). The higher magnification images of the fractured surfaces in Figs. 3.13c and f show quite a few voids.

Around the voids, the insets in Figs. 3.13c and f reveal unbonded particle sides with the signature of cellular structure surface similar to that of the undeformed starting particles in Fig. 3.2c. The inset also shows splat regions where particles initially bonded, as confirmed by low oxygen signal arrowed in Fig. 3.14, but subsequently fractured under the tensile load.

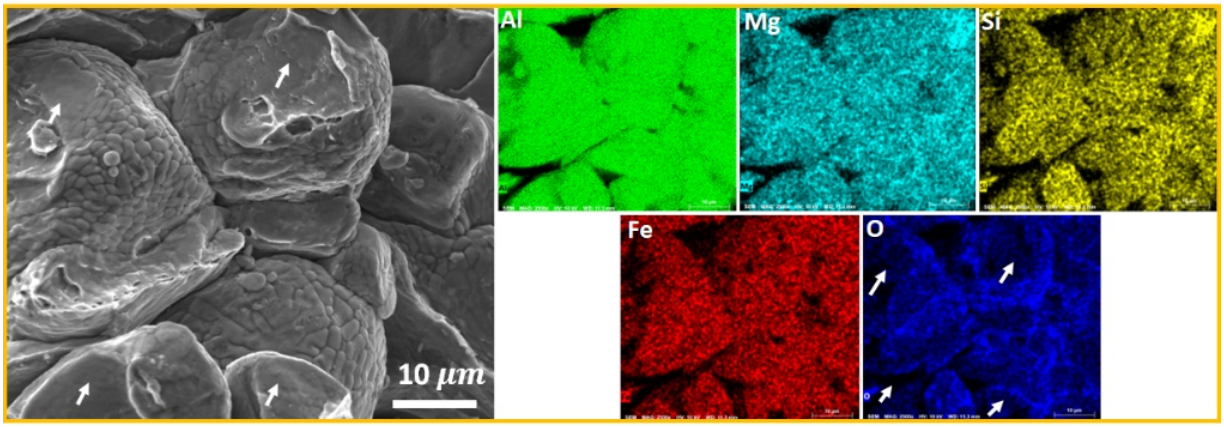

Figure 3.14: ETD- SEM image and EDS maps of fractured surface of tensile tested CSWed AA 6061-T651 sample. White arrows point at fractured surface with splash/initially bonded interface which corresponds to region of low oxygen signals in the oxygen map.

Notably, no dimple-like features are observed on the fractured surfaces, which are characteristic of ductile fracture [99]. Instead, the fracture predominantly propagates from a source—microvoids, and along the particle-particle interfaces, leading to brittle-like fracture behavior and rapid crack propagation. Cataloguing these observations and those of Fig. 3.5, the crack propagation mechanism can therefore be described in Fig. 3.15a as follows: (i) nucleation of microcracks from microvoid nodes, (ii) connection of microcracks to form a web-like crack

propagating network, (iii) advancing microcracks towards bonded interparticle splat region. These fractographic features—multiple microvoids and web-like crack propagating network—contributes to the low strength, ductility, and fracture strain recorded for CSWed sample in Fig. 3.10 and *Section 3.3.3.2.* Even though crack-initiating microvoids are ubiquitous throughout the weld area, the eventual fracture seems to occur in a poorly-bonded region—near the grove face, where oblique microparticle impact likely occur, as schematized in the upper part of Fig. 3.15b.

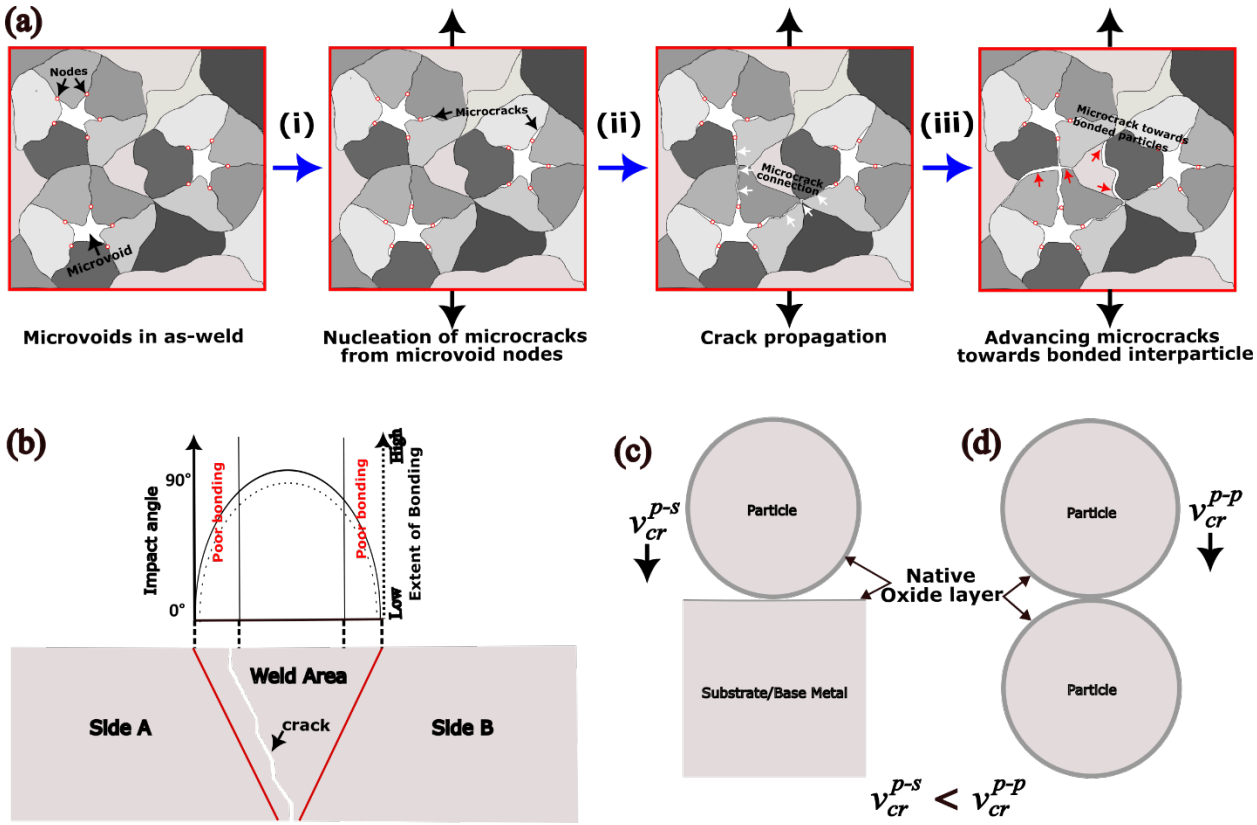

Figure 3.15: A schematic diagram for (a) failure mechanism in CSWed parts: (i) nucleation of microcracks from microvoid nodes, (ii) connection of microcracks to form a web-like crack propagating network, (iii) advancing microcracks towards bonded interparticle splat region; (b) fracture propagation location in weld area and the possible effect of particle impact angle, (c) oxide layer between particle and base material in contact, and (d) oxide layer between particles in contact.

To summarize, the observation of deposited particles on both sides of fractured CSWed sample in Fig. 3.13 shows that interparticle fracture and failure occur in the weld area, and close to the groove face (Fig. 3.6b), as schematized in Fig. 3.15b. The fractured area and path also suggest that the

particle-base (substrate) interface achieved a better metallurgical bonding than those at the particle-particle interface. This is interesting and it leads to an important conclusion necessary to help optimize the CSW process: the v_{cr} for particle-substrate (v_{cr}^{p-s}) is lower than for particle-particle (v_{cr}^{p-p}). The rationale for partitioning v_{cr} is further explained by the energetic budget for delaminating and expelling native surface oxide from the particle-substrate/particle-particle interface, as schematized in Fig. 3.15c and d. Fig. 3.15c shows a typical spherical particle ladened with a surface oxide layer and launched towards a fairly-clean substrate surface that is prepared just before CSW; this represents the case of particle-base material contact and ~30 % of the energy budget for particle plasticity is consumed to delaminate and expel oxide from the surface of the particle alone [35]. On the other hand, Fig. 3.15d represents a particle-particle contact, where each particle possesses its surface oxide layer before contact; this implies that the energetic budget to extrude surface oxides should be, to a first-order approximation, twice the particle-substrate case so that $v_{cr}^{p-p} > v_{cr}^{p-s}$. The bonding in CS deposits is influenced by the extent of plastic deformation of the particles and the presence of oxide scale at the particle interface [29,147]. It is well-established that an oxide-free interface is crucial to achieving clean metal-to-metal contact for successful particle-substrate and interparticle metallic bonding [42]. This conclusion (partitioning of v_{cr}) is corroborated by previous work by Wu et al. [137] who reported different v_{cr} for the first layer build-up (substrate-particle) and the particle-particle bonding case in the CS of Al–Si powders on a mild steel substrate, with the later requiring a higher v_{cr} [137]. Hence, to optimize a CSW process, the targeted particle velocity should be high enough, above v_{cr}^{p-p}.

3.2.3.4 Advantages of CSW over TIG welding, and future direction for CSW optimization.

So far, we have demonstrated that the application of the cold spray process can be expanded beyond its conventional use as a coating and in-situ repair technology. Although, the TIG-welded

sample (Fig. 3.7) possesses better fusion of weld to base and in turn, improved tensile strength and impact toughness (Fig. 3.10) than the CSWed sample (Fig. 3.4a-c), if optimized, CSW will offer the following advantages:

- Retention of feedstock properties before and after CS, and negligible micro- and nano-structural alterations. This is due to the short contact time between the particles and pre-heated gas, and the rapid cooling of the gas as it expands through the diverging section of the nozzle [22,148].
- Lower total energy consumption for solid-state welding process, since particle bonding primarily relies on kinetic energy rather than thermal energy.
- Unlike the conventional welding process that emits fumes which are responsible for both acute chronic and health issues, CSW uses no combustible or fuel gases, making it a green technology suitable for combating environmental issues like global warming, acidification, and eutrophication.

  Inhibition of deleterious phase transformation to enhance weld quality due to the suppression of excessive heat input: In addition to HAZ, the typical weld area in TIG welded sample (see impact tested TIG sample in Fig. 3.16) shows the presence of deleterious porosities and dendritic microstructure (mostly Al-Si eutectic phase, with other Al-Fe-Si and Al-Mg-Si rich phases), which is a result of the fast cooling from the molten metal [52]. Such complex phase transformation/formation is not found in the CSWed sample. This also favors CSW as an advantageous solid-state welding process for suppressing deleterious HAZs, especially in precipitation-hardened or temperature-sensitive alloys.

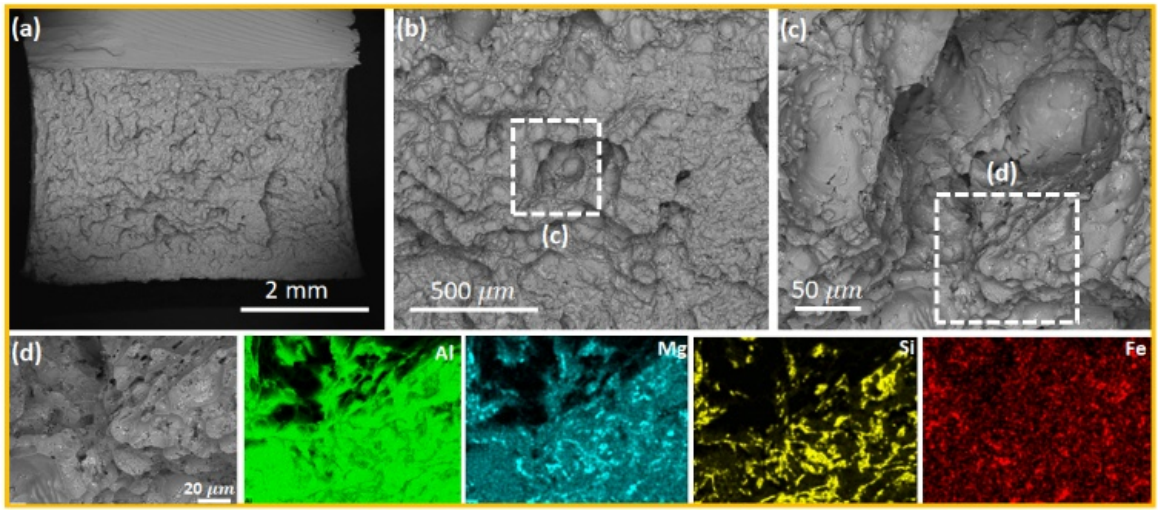

Figure 3.16: SEM BSED images and EDS map analysis of the fractured surface of impact tested TIG welded AA 6061-T651 sample showing deleterious phases in the weld area: (a) overview, (b, c) progressive high magnification images of selected fractured site within the weld area, and (d) EDS maps of the fractured surface.

Although post-weld heat treatment can be introduced as an additional step to improving the CSW process, pursuing a one-step solid-state welding process (i.e., without post-weld heat treatment) is more desirable which is an important future direction for this solid-state welding technology. From our current result, it is possible that further accessing higher particle velocity (but below 1.6 v_{cr} where hydrodynamic particle penetration sets on [133]) can improve bonding and weld quality. From the processing parameters provided in *Section* 3.2.1, we determine the particle velocity for CSW to be 843 m/s, using the following equations [137,149]:

$$v_p = \frac{1}{\frac{1}{M}\sqrt{\frac{M_{N_2}}{\gamma RT}}+0.85\sqrt{\frac{D}{x}\sqrt{\frac{\rho_p}{P_0}}}} \quad \ldots (3.1a)$$

$$\frac{A_e}{A^*} = \frac{1}{M}\left\{\left(\frac{2}{\gamma+1}\right)\left[1+\left(\frac{\gamma-1}{2}\right).M^2\right]\right\}^{\frac{\gamma+1}{2(\gamma-1)}} \quad \ldots (3.1b)$$

where v_p is the particle velocity; M is the Mach number A_e is the nozzle exit area; A^* is the nozzle throat area and $\frac{A_e}{A^*}$ is 5.6; γ is the ratio of specific heat, typically 1.4 for diatomic gases [137]; M_{N_2} is molecular weight of nitrogen gas; R is the gas constant (8.314 J.mol^{-1}.K^{-1}), T is the gas

temperature, D is the particle diameter, x is the axial position, ρ_p is the particle density, P_0 is the nitrogen supply pressure. This velocity is just close to the v_{cr} of AA 6061 [150], and further increase to ~1.3 v_{cr} where maximum metallurgical bonding is expected [133], would greatly improve the weld quality.

3.3 Summary and Conclusion

This study investigates the potential expansion of CS process as an alternative to existing welding methods. Using AA 6061-T651 plate as the welded component material and characterization techniques, including scanning electron microscopy, energy dispersive x-ray spectroscopy, and x-ray microscopy, we evaluate CSWed samples and compared them with TIG welded samples. Based on the results, the following conclusions can be drawn:

i. Unlike TIG welding, CSW impedes the coevolution of deleterious phases: CSWed sample maintains a homogenous phase in the weld area and also preserves the starting material microstructure in both the particle feedstock (weld area) and the adjacent base.

ii. SEM and XRM analyses reveal the formation of voids in CSWed area and porosities within the TIG-welded area. Lack of metallurgical bonding at the particle-particle interface results in the formation of microvoids at “triple or quadruple junctions” in CSWed samples.

iii. The CSWed sample’s weld area (70-104 HV) and surrounding base (113-122 HV) show higher hardness than those in the TIG welded sample that exhibits very low hardness (50-70 HV) that extended non-uniformly towards the base. In the CSWed sample, no HAZ is observed in the adjacent base, which presents a significant advantage over fusion welding process.

iv. Both TIG welded and CSWed sample exhibit lower mechanical properties compared to the as-received sample: The yield strength and impact toughness in TIG welded sample is 59 % and 36 % lower than the as-received, respectively, while those of the CSWed samples are also lower than the as-received by 94 % (yield strength) and 73 % (impact toughness), respectively.

v. The TIG welded sample fails within the HAZ (~10 mm away from the weld center) and fracture analysis show dimples that are characteristic of ductile fracture mode. On the other hand, CSWed samples fail within the weld area along the particle-particle interface, in a manner characteristic of a brittle-like fracture.

vi. Microvoids are identified as the source of crack initiation sites in CSWed samples, and a crack propagation mechanism is proposed as follows: (i) nucleation of microcracks from microvoid nodes, (ii) connection of microcracks to form a web-like crack propagating network, (iii) Propagation of advancing microcracks towards bonded interparticle splat region.

vii. The fracture path in CSWed sample shows that the particle-substrate achieves better metallurgical bonding than the particle-particle case. This suggests that the v_{cr} required to achieve particle-particle bonding (v_{cr}^{p-p}) is higher than that for particle-substrate bonding (v_{cr}^{p-s}); as such particle impact velocity must be sufficiently high to achieve maximum metallurgical bonding in a particle-particle bonding case.

This study shows that CSW has the capability to address some long-standing challenges in conventional welding techniques. Most importantly, it (the study) identifies the necessary CSW challenges that must be addressed to push the expansion of CS process to solid-state welding. Besides increasing particle impact velocities well above v_{cr} or adding additional steps like post-

weld heat treatment, this study also gives researchers in the cold spray community what area needs further investigation that can be embarked upon to push the application of CSW to fruition.

Chapter: 4 Conclusion

4.1 Summary

This thesis develops and evaluates cold spray (CS) process as a new alternative welding technique, to circumvent the drawbacks in existing solid-state and liquid-state welding methods; a process called cold spray welding (CSW). Using AA 6061-T651 aluminum alloy as the model precipitation-hardened alloy and different characterization techniques—scanning electron microscopy, energy dispersive x-ray spectroscopy, and x-ray microscopy—the origin of softening and mechanical performance of a Tungsten inert gas (TIG) welded plates are comprehensively investigated and compared with CSWed samples.

The results confirm microstructural changes (phase transformation) and localized softening (or HAZ) as the major drawback in TIG-welded AA 6061-T651 samples due to high heat input involved in the welding process; this softening extends up to ~40 mm from the weld center. In contrast, such HAZ is not observed in CSWed samples, rather the weld and neighboring base areas have the same properties before and after CSW. This characteristic presents a significant advantage of proposed CSW over existing welding processes because CSW can:

- retain properties of feedstock material after deposition
- suppress unfavorable structural changes and HAZ formation,
- reduce production cost due to process flexibility and the absence of combustible/fume gases that also makes the CSW process greener.

Although both CSWed and TIG-welded samples exhibit lower mechanical properties compared to the as-received material, the lowest tensile strength and impact toughness are recorded in the CSWed samples than in TIG-welded samples.

On the tensile failure mode, the TIG welded samples failed at the softest HAZ region which is ~10 mm away from the porosity-ladened weld center. This indicates that the severity of phase transformation in the HAZ has a more significant impact on the mechanical performance of TIG-welded samples than the presence of pores in the weld area. On the other hand, CSWed samples constitute microvoids that are homogeneously distributed in the weld area, and their (microvoids) formation is attributed to inadequate metallurgical bonding formed at triple and quadruple particle junctions. Consequently, tensile-tested CSWed samples rather failed within the weld area, with the microvoids acting as crack-initiating sites; this results in lower mechanical performance than TIG-welded samples. The fracture propagation within the CSWed area indicates better bonding between particle-substrate than particle-particle interfaces, suggesting lower v_{cr} to achieve maximum metallurgical bonding in the former than the latter.

Overall, the findings in this thesis suggest that CSW offers advantages over traditional welding, but the issue of poor metallurgical bonding in CSWed samples will continue to hinder its projected expansion for industrial applications. Further investigation is needed to optimize CSW for practical use, hence, the recommended next steps are highlighted in the “Future works” section.

4.2 Future works

The findings from this work show that CSW presents some advantages over traditional welding processes. However, its current limitations can impede its widespread use as a viable solid-state

welding process. To enhance the feasibility of CSW for industrial applications, the following research areas are suggested for future exploration:

- **Optimization of base material**: Investigate the effect of welding geometries of base plates and surface roughness of bevel face on bonding and deposition efficiency of CSW.
- **Optimization of feedstock (powder)**: The morphology and surface condition of feedstock powder play a major role in the quality of bonds in CS process. The following parameters can be tuned to optimize the mechanical properties of CSWed parts [27];
    - Particle size: It is well known that the smaller the particle size the higher the v_{cr}. This is because smaller particles have a higher surface area-to-volume ratio, resulting in lower kinetic energy, faster heat conduction from the bonding interface, and higher amount of oxides that impede bonding.
    - Particle distribution: Mixed particle distribution is known to be advantageous for optimizing deposit density. The finer particles can fill the voids/gaps those formed between the coarser particles [134].
    - Particle geometry: Particle geometry is challenging to control, yet it affects the flowability, cold sprayability and in turn, the deposition efficiency and coating porosity. Generally, irregular shaped particles are more difficult to feed due to their tendency to pack more closely together compared to spherical particles [22].
    - Native surface oxide layer: The presence of native oxide layer acts as geometrical constraints to extensive particle plasticity, increasing the energy needed to initiate metal-to-metal contact. As a result, the v_{cr} increases with the presence of native oxides. Particles with little to no native oxide layer are therefore advantageous for achieving quality bonding.

- **Optimization of process parameters**: Several process parameters play a significant role in the onset of bonding and bond quality, and they can be optimized as well to improve the quality of weld in CSW process.
    - **Propulsive gas**: Compressed gas in the CS process performs two key roles, to transport the powder particles, and propelling the gas powder mixture. Careful selection of gas type (air, helium, and nitrogen), temperature and pressure can enhance bonding quality.
    - **Powder feeding rate**: The feed rate—powder amount metered into the spray nozzle per time—directly impacts the nature of gas-particle stream from the nozzle, which affects particle velocity. Higher feed rates can decrease the particle velocity due to intense gas-particle interaction. A careful selection of powder feed rate will therefore improve the quality of CS deposits, and in turn, the mechanical properties of CSWed parts.
    - **Nozzle parameters**: Key nozzle parameters, include nozzle transverse speed (higher speeds are recommended to avoid high residual stress at the interface of deposit and substrate), stand-off distance (deposition efficiency, DE, increases with stand-off distance up to a critical value), and spray angle (optimum at 90° for higher DE, deviation leads to lowers DE), play an important role in deposition efficiency.
- **Weld optimization by post weld heat treatment:** Investigate the effect of post-weld heat treatment on metallurgical bonding and mechanical performance of CSWed parts.

By optimizing the aforementioned parameters, it is possible to minimize void formation and in turn, enhance the mechanical properties of CSWed parts.

References

[1] S. Rathee, M. Srivastava, S. Maheshwari, T. K. Kundra, and A. N. Siddiquee, *Friction Based Additive Manufacturing Technologies*. 2018. doi: 10.1201/9781351190879.

[2] D. Varshney and K. Kumar, "Structured review of papers on the use of different activating flux and welding techniques," *Ain Shams Eng. J.*, vol. 12, no. 3, pp. 3339–3351, 2021, doi: 10.1016/j.asej.2020.11.013.

[3] D. K. Dwivedi, "Metal joining: Need, Approaches and Mechanisms," in *Fundamentals of Metal Joining*, Roorkee, India: Springer Nature Singapore Pte Ltd., 2022, pp. 3–31. doi: 10.1007/978-981-16-4819-9_29.

[4] H. Z. Yu and R. S. Mishra, "Additive friction stir deposition: a deformation processing route to metal additive manufacturing," *Mater. Res. Lett.*, vol. 9, no. 2, pp. 71–83, 2021, doi: 10.1080/21663831.2020.1847211.

[5] W. Borek, B. Tomiczek, and SCA Alfaro (Eds.), Welding- Modern Topics. London, UK: IntechOpen Limited, 2021. doi: http://dx.doi.org/10.5772/intechopen.83204.

[6] R. Kumar, N. Ramesh Mevada, S. Rathore, N. Agarwal, V. Rajput, and A. S. Barad, "Experimental Investigation and Optimization of TIG Welding Parameters on Aluminum 6061 Alloy Using Firefly Algorithm," *IOP Conf. Ser. Mater. Sci. Eng.*, vol. 225, p. 012153, 2017, doi: 10.1088/1757-899x/225/1/012153.

[7] T. Tadavi, B. Jogi, S. Dhende, S. Banait, and P. Wagh, "Microscopic Analysis of Heat Affected Zone (HAZ) of Submerged Arc Welding (saw) Joint for 1018 Mild Steel Sheet," vol. 137, pp. 194–199, 2017, doi: 10.2991/iccasp-16.2017.32.

[8] R. D. Ardika, T. Triyono, N. Muhayat, and Triyono, “A review porosity in aluminum welding,” *Procedia Struct. Integr.*, vol. 33, no. C, pp. 171–180, 2021, doi: 10.1016/j.prostr.2021.10.021.

[9] M. Norouzian, M. Amne Elahi, and P. Plapper, “A review: Suppression of the solidification cracks in the laser welding process by controlling the grain structure and chemical compositions,” *J. Adv. Join. Process.*, vol. 7, no. January, p. 100139, 2023, doi: 10.1016/j.jajp.2023.100139.

[10] G. Fu, F. Tian, and H. Wang, “Studies on softening of heat-affected zone of pulsed-current GMA welded Al-Zn-Mg alloy,” *J. Mater. Process. Technol.*, vol. 180, no. 1–3, pp. 216–220, 2006, doi: 10.1016/j.jmatprotec.2006.06.008.

[11] M. N. Muigai, E. T. Akinlabi, and F. M. Mwema, “Influence of direct current (DC) on hardness of weld stainless steel coating - A model for mild steel repair,” *Mater. Today Proc.*, vol. 44, pp. 1133–1135, 2021, doi: 10.1016/j.matpr.2020.11.230.

[12] A. C. Munoz *et al.*, “Comparison of TIG welded and friction stir welded Al-4 . 5Mg-0 . 26Sc alloy To cite this version : HAL Id : hal-01005980 Comparison of TIG welded and friction stir welded,” pp. 0–7, 2017.

[13] K. P. Mehta, P. Carlone, A. Astarita, F. Scherillo, F. Rubino, and P. Vora, “Conventional and cooling assisted friction stir welding of AA6061 and AZ31B alloys,” *Mater. Sci. Eng. A*, vol. 759, no. January, pp. 252–261, 2019, doi: 10.1016/j.msea.2019.04.120.

[14] R. S. Mishra and Z. Y. Ma, “Friction stir welding and processing,” *Mater. Sci. Eng. R Reports*, vol. 50, no. 1–2, pp. 1–78, 2005, doi: 10.1016/j.mser.2005.07.001.

[15] M. T.S.M. Sai *et al.*, “Experimental Study on Effect of Welding Parameters of Friction Stir Welding (FSW) on Aluminium AA5083 T-joint,” *Inf. Technol. J.*, vol. 15, no. 4, pp. 99–107, 2016, doi: 10.3923/itj.2016.99.107.

[16] B. Meyghani and C. Wu, “Progress in Thermomechanical Analysis of Friction Stir Welding,” *Chinese J. Mech. Eng. (English Ed.*, vol. 33, no. 1, 2020, doi: 10.1186/s10033-020-0434-7.

[17] G. N. ShivaKumar and G. Rajamurugan, “Friction stir welding of dissimilar alloy combinations—A Review,” *Proc. Inst. Mech. Eng. Part C J. Mech. Eng. Sci.*, vol. 236, no. 12, pp. 6688–6705, 2022, doi: 10.1177/09544062211069292.

[18] B. B. Lerman, R. B. Devereux, and P. M. Okin, *Welding Engineering*, vol. 45, no. 11 SUPPL. 2005. doi: 10.1016/j.jacc.2005.05.004.

[19] F. Gärtner, T. Stoltenhoff, T. Schmidt, and H. Kreye, “The cold spray process and its potential for industrial applications,” *J. Therm. Spray Technol.*, vol. 15, no. 2, pp. 223–232, 2006, doi: 10.1361/105996306X108110.

[20] H. T. Wang, C. J. Li, G. J. Yang, and C. X. Li, “Cold spraying of Fe/Al powder mixture: Coating characteristics and influence of heat treatment on the phase structure,” *Appl. Surf. Sci.*, vol. 255, no. 5 PART 1, pp. 2538–2544, 2008, doi: 10.1016/j.apsusc.2008.07.127.

[21] D. Guo *et al.*, “Cold Spray: Over 30 Years of Development Toward a Hot Future,” *J. Therm. Spray Technol.*, vol. 31, no. 4, pp. 866–907, 2022, doi: 10.1007/s11666-022-01366-4.

[22] I. Botef and J. Villafuerte, “Modern Cold Spray, Overview,” Julio Vill., Windsor: Springer International Publishing, 2015, pp. 1–29. doi: 10.1007/978-3-319-16772-5_1.

[23] H. Assadi, H. Kreye, F. Gärtner, and T. Klassen, “Cold spraying – A materials perspective,” *Acta Mater.*, vol. 116, pp. 382–407, 2016, doi: 10.1016/j.actamat.2016.06.034.

[24] W. Li, K. Yang, S. Yin, X. Yang, Y. Xu, and R. Lupoi, “Solid-state additive manufacturing and repairing by cold spraying: A review,” *J. Mater. Sci. Technol.*, vol. 34, no. 3, pp. 440–457, 2018, doi: 10.1016/j.jmst.2017.09.015.

[25] S. Yin *et al.*, “Cold spray additive manufacturing and repair: Fundamentals and applications,” *Addit. Manuf.*, vol. 21, no. August 2017, pp. 628–650, 2018, doi: 10.1016/j.addma.2018.04.017.

[26] H. Singh, T. S. Sidhu, and S. B. S. Kalsi, “Cold spray technology: Future of coating deposition processes,” *Frat. ed Integrita Strutt.*, vol. 22, pp. 69–84, 2012, doi: 10.3221/IGF-ESIS.22.08.

[27] M. A. Adaan-Nyiak and A. A. Tiamiyu, “Recent advances on bonding mechanism in cold spray process: A review of single-particle impact methods,” *J. Mater. Res.*, vol. 38, no. 1, pp. 69–95, 2023, doi: 10.1557/s43578-022-00764-2.

[28] A. Moridi, S. M. Hassani-Gangaraj, M. Guagliano, and M. Dao, “Cold spray coating: Review of material systems and future perspectives,” *Surf. Eng.*, vol. 30, no. 6, pp. 369–395, 2014, doi: 10.1179/1743294414Y.0000000270.

[29] Y. J. Li, X. T. Luo, and C. J. Li, “Improving deposition efficiency and inter-particle bonding of cold sprayed Cu through removing the surficial oxide scale of the feedstock powder,” *Surf. Coatings Technol.*, vol. 407, no. September 2020, p. 126709, 2021, doi: 10.1016/j.surfcoat.2020.126709.

[30] M. V. Vidaller, A. List, F. Gaertner, T. Klassen, S. Dosta, and J. M. Guilemany, “Single Impact Bonding of Cold Sprayed Ti-6Al-4V Powders on Different Substrates,” *J. Therm. Spray Technol.*, vol. 24, no. 4, pp. 644–658, 2015, doi: 10.1007/s11666-014-0200-4.

[31] S. Singh, R. K. S. Raman, C. C. Berndt, and H. Singh, “Influence of cold spray parameters on bonding mechanisms: A review,” *Metals (Basel).*, vol. 11, no. 12, 2021, doi: 10.3390/met11122016.

[32] H. Koivuluoto, J. Larjo, D. Marini, G. Pulci, and F. Marra, “Cold-Sprayed Al6061 Coatings : Online Spray,” *Coatings*, vol. 10, p. 348, 2020.

[33] W. Y. Li and W. Gao, “Some aspects on 3D numerical modeling of high velocity impact of particles in cold spraying by explicit finite element analysis,” *Appl. Surf. Sci.*, vol. 255, no. 18, pp. 7878–7892, 2009, doi: 10.1016/j.apsusc.2009.04.135.

[34] T. Schmidt, F. Gärtner, H. Assadi, and H. Kreye, “Development of a generalized parameter window for cold spray deposition,” *Acta Mater.*, vol. 54, no. 3, pp. 729–742, 2006, doi: 10.1016/j.actamat.2005.10.005.

[35] A. A. Tiamiyu *et al.*, “Oxide layer delamination: An energy dissipation mechanism during high-velocity microparticle impacts,” *Appl. Surf. Sci.*, vol. 574, no. May 2021, p. 151673, 2022, doi: 10.1016/j.apsusc.2021.151673.

[36] Y. Ichikawa, R. Tokoro, M. Tanno, and K. Ogawa, “Elucidation of cold-spray deposition mechanism by auger electron spectroscopic evaluation of bonding interface oxide film,” *Acta Mater.*, vol. 164, pp. 39–49, 2019, doi: 10.1016/j.actamat.2018.09.041.

[37] G. Bae, Y. Xiong, S. Kumar, K. Kang, and C. Lee, “General aspects of interface bonding

in kinetic sprayed coatings," *Acta Mater.*, vol. 56, no. 17, pp. 4858–4868, 2008, doi: 10.1016/j.actamat.2008.06.003.

[38] W. Y. Li *et al.*, "Ti and Ti-6Al-4V coatings by cold spraying and microstructure modification by heat treatment," *Adv. Eng. Mater.*, vol. 9, no. 5, pp. 418–423, 2007, doi: 10.1002/adem.200700022.

[39] C. D. Reddy, Z. Q. Zhang, S. Msolli, J. Guo, and N. Sridhar, "Impact induced metallurgical and mechanical interlocking in metals," *Comput. Mater. Sci.*, vol. 192, no. January, p. 110363, 2021, doi: 10.1016/j.commatsci.2021.110363.

[40] T. Liu, J. D. Leazer, and L. N. Brewer, "Particle deformation and microstructure evolution during cold spray of individual Al-Cu alloy powder particles," *Acta Mater.*, vol. 168, pp. 13–23, 2019, doi: 10.1016/j.actamat.2019.01.054.

[41] K. H. Ko, J. O. Choi, H. Lee, Y. K. Seo, S. P. Jung, and S. S. Yu, "Cold spray induced amorphization at the interface between Fe coatings and Al substrate," *Mater. Lett.*, vol. 149, pp. 40–42, 2015, doi: 10.1016/j.matlet.2015.02.118.

[42] S. Yin, X. Wang, W. Li, H. Liao, and H. Jie, "Deformation behavior of the oxide film on the surface of cold sprayed powder particle," *Appl. Surf. Sci.*, vol. 259, pp. 294–300, 2012, doi: 10.1016/j.apsusc.2012.07.036.

[43] T. M. Davison, G. S. Collins, and F. J. Ciesla, "Numerical modelling of heating in porous planetesimal collisions," *Icarus*, vol. 208, no. 1, pp. 468–481, 2010, doi: 10.1016/j.icarus.2010.01.034.

[44] J. Norrish, *Advanced welding process*, 2006th ed., vol. 2, no. 5. Cambridge: Woodhead

Publishing Ltd, 2009.

[45] P. Kah and J. Martikainen, “Current trends in welding processes and materials: Improve in effectiveness,” *Rev. Adv. Mater. Sci.*, vol. 30, no. 2, pp. 189–200, 2012.

[46] A. Kumar and S. Sundarrajan, “Selection of welding process parameters for the optimum butt-joint strength of an aluminum alloy,” *Mater. Manuf. Process.*, vol. 21, no. 8, pp. 779–782, 2006, doi: 10.1080/03602550600728117.

[47] L. P. Connor, “Welding Metallurgy,” *Weld. Handb.*, pp. 89–124, 1987, doi: 10.1007/978-1-349-10624-0_4.

[48] B. Cevik and B. GülenC, “The effect of welding speed on mechanical and microstructural properties of 5754 Al (AlMg3) alloy joined by laser welding,” *Mater. Res. Express*, vol. 5, no. 8, pp. 0–11, 2018, doi: 10.1088/2053-1591/aad3b0.

[49] N. Rao and D. G. M. Midhani, “Paper on Comparision of Conventional Welding Methods With Solid-State Welding Techniques,” *Int. Res. J. Eng. Technol.*, pp. 315–318, 2016, [Online]. Available: www.irjet.net

[50] S. J. Doshi, A. V Gohil, N. Mehta, and S. Vaghasiya, “Challenges in Fusion Welding of Al alloy for Body in White,” *Mater. Today Proc.*, vol. 5, no. 2, pp. 6370–6375, 2018, doi: 10.1016/j.matpr.2017.12.247.

[51] J. YI, G. WANG, S. kang LI, Z. wen LIU, and Y. li GONG, “Effect of post-weld heat treatment on microstructure and mechanical properties of welded joints of 6061-T6 aluminum alloy,” *Trans. Nonferrous Met. Soc. China (English Ed.*, vol. 29, no. 10, pp. 2035–2046, 2019, doi: 10.1016/S1003-6326(19)65110-1.

[52] H. Rojas *et al.*, "The impact of heat input on the microstructures, fatigue behaviors, and stress lives of TIG-welded 6061-T6 alloy joints," *Mater. Res. Express*, vol. 7, no. 12, 2020, doi: 10.1088/2053-1591/abd136.

[53] Z. Wan *et al.*, "Improvement in tensile properties of 2219-T8 aluminum alloy TIG welding joint by PMZ local properties and stress distribution," *Mater. Sci. Eng. A*, vol. 839, no. November 2021, p. 142863, 2022, doi: 10.1016/j.msea.2022.142863.

[54] Y. Xu, Z. Zhang, Z. Gao, Y. Bai, P. Zhao, and W. Mao, "Effect of sc on the hot cracking properties of 7xxx aluminum alloy and the microstructure of squeeze castings," *Materials (Basel).*, vol. 14, no. 22, pp. 1–11, 2021, doi: 10.3390/ma14226881.

[55] J. P. Bergmann, F. Petzoldt, R. Schürer, and S. Schneider, "Solid-state welding of aluminum to copper - Case studies," *Weld. World*, vol. 57, no. 4, pp. 541–550, 2013, doi: 10.1007/s40194-013-0049-z.

[56] J. A. Vargas, J. E. Torres, J. A. Pacheco, and R. J. Hernandez, "Analysis of heat input effect on the mechanical properties of Al-6061-T6 alloy weld joints," *Mater. Des.*, vol. 52, pp. 556–564, 2013, doi: 10.1016/j.matdes.2013.05.081.

[57] Z. Lu, J. Xu, L. Yu, H. Zhang, and Y. Jiang, "Studies on softening behavior and mechanism of heat-affected zone of spray formed 7055 aluminum alloy under TIG welding," *J. Mater. Res. Technol.*, vol. 18, pp. 1180–1190, 2022, doi: 10.1016/j.jmrt.2022.03.074.

[58] F. Gulshan and Q. Ahsan, "Effect of Heat Input on the Structure and Properties of Aluminium Weldment TIG Welded with 4043 Filler Rod," *Chem. Mater. Eng.*, vol. 2, no. 2, pp. 25–32, 2014, doi: 10.13189/cme.2014.020201.

[59] M. Hakem, S. Lebaili, S. Mathieu, D. Miroud, A. Lebaili, and B. Cheniti, “Effect of microstructure and precipitation phenomena on the mechanical behavior of AA6061-T6 aluminum alloy weld,” *Int. J. Adv. Manuf. Technol.*, vol. 102, no. 9–12, pp. 2907–2918, 2019, doi: 10.1007/s00170-019-03401-1.

[60] Y. Hu, S. Wu, Z. Shen, H. Cao, X. Zhong, and P. J. Withers, “Fine equiaxed zone induced softening and failure behavior of 7050 aluminum alloy hybrid laser welds,” *Mater. Sci. Eng. A*, vol. 821, no. February, p. 141597, 2021, doi: 10.1016/j.msea.2021.141597.

[61] Z. Liu, H. Zhang, Z. Hou, H. Feng, P. Dong, and P. K. Liaw, “Microstructural origins of mechanical and electrochemical heterogeneities of friction stir welded heat-treatable aluminum alloy,” *Mater. Today Commun.*, vol. 24, no. April, p. 101229, 2020, doi: 10.1016/j.mtcomm.2020.101229.

[62] J. Cheng, G. Song, X. Zhang, C. Liu, and L. Liu, *Review of techniques for improvement of softening behavior of age-hardening aluminum alloy welded joints*, vol. 14, no. 19. 2021. doi: 10.3390/ma14195804.

[63] Q. Zhu, H. Yu, J. Zhang, M. Li, and X. Hu, “Experimental study on tig welding properties of 6061 and 7003 aluminum alloys,” *IOP Conf. Ser. Earth Environ. Sci.*, vol. 621, no. 1, 2021, doi: 10.1088/1755-1315/621/1/012060.

[64] J. Cheng, G. Song, Z. Zhang, M. S. Khan, Z. Liu, and L. Liu, “Improving heat-affected zone softening of aluminum alloys by in-situ cooling and post-weld rolling,” *J. Mater. Process. Technol.*, vol. 306, no. May, p. 117639, 2022, doi: 10.1016/j.jmatprotec.2022.117639.

[65] Joseph C. Benedyk, “International Temper Designation Systems for Wrought Aluminum Alloys:,” 2010.

[66] ASTM, “E3-11 Standard Guide for Preparation of Metallographic Specimens 1,” *ASTM Int.*, vol. i, no. Reapproved, pp. 1–12, 2011, doi: 10.1520/E0003-11.2.

[67] ASTM, “E112 − 13 Standard Test Methods for Determining Average Grain Size,” *ASTM Int.*, vol. 13, no. Reapproved, pp. 1–27, 2021, doi: 10.1520/E0112-13R21.1.4.

[68] ASTM E8, “ASTM E8/E8M standard test methods for tension testing of metallic materials 1,” *Annu. B. ASTM Stand. 4*, no. C, pp. 1–27, 2010, doi: 10.1520/E0008.

[69] ASTM E 23-12c, “Standard test methods for notched bar impact testing of metallic materials,” *Standards*, pp. 1–25, 2012, doi: 10.1520/E0023-18.

[70] U. R. Kattner, “the Calphad Method and Its Role in Material and Process Development,” *Tecnol. em Metal. Mater. e Mineração*, vol. 13, no. 1, pp. 3–15, 2016, doi: 10.4322/2176-1523.1059.

[71] D. Peng, J. Shen, Q. Tang, C. P. Wu, and Y. B. Zhou, “Effects of aging treatment and heat input on the microstructures and mechanical properties of TIG-welded 6061-T6 alloy joints,” *Int. J. Miner. Metall. Mater.*, vol. 20, no. 3, pp. 259–265, 2013, doi: 10.1007/s12613-013-0721-8.

[72] R. E. R.-H. Reza Abbaschain, Lara Abbaschain, “Solidification of Metals,” in *Physical Metallurgy Principal*, Fourth., J. D. Hilda Gowans, Ed. Stamford, USA: Cengage learning, 2009, pp. 408–462.

[73] H. Yu, Y. Xu, J. Song, J. Pu, X. Zhao, and G. Yao, “On-line monitor of hydrogen porosity based on arc spectral information in Al-Mg alloy pulsed gas tungsten arc welding,” *Opt. Laser Technol.*, vol. 70, pp. 30–38, 2015, doi: 10.1016/j.optlastec.2015.01.010.

[74] R. Trivedi *et al.*, “In situ observations of weld pool solidification using transparent metal-analog systems,” *J. Appl. Phys.*, vol. 93, no. 8, pp. 4885–4895, 2003, doi: 10.1063/1.1559934.

[75] M. Brůna and A. Sládek, “Hydrogen analysis and effect of filtration on final quality of castings from aluminium alloy AlSi7Mg0,3,” *Arch. Foundry Eng.*, vol. 11, no. 1, pp. 5–10, 2011.

[76] K. Vasu, H. Chelladurai, A. Ramaswamy, S. Malarvizhi, and V. Balasubramanian, “Effect of fusion welding processes on tensile properties of armor grade, high thickness, non-heat treatable aluminium alloy joints,” *Def. Technol.*, vol. 15, no. 3, pp. 353–362, 2019, doi: 10.1016/j.dt.2018.11.004.

[77] M. Samiuddin, J. long Li, M. Taimoor, M. N. Siddiqui, S. U. Siddiqui, and J. tao Xiong, “Investigation on the process parameters of TIG-welded aluminum alloy through mechanical and microstructural characterization,” *Def. Technol.*, vol. 17, no. 4, pp. 1234–1248, 2021, doi: 10.1016/j.dt.2020.06.012.

[78] M. Hosseinifar and D. V. Malakhov, “The sequence of intermetallics formation during the solidification of an Al-Mg-Si alloy containing la,” *Metall. Mater. Trans. A Phys. Metall. Mater. Sci.*, vol. 42, no. 3, pp. 825–833, 2011, doi: 10.1007/s11661-010-0453-6.

[79] W. D. Callister, “Mechanical Properties of Metals,” in *Materials science and engineering: An introduction*, 8th ed., John Wiley & Sons Inc.

[80] G. Song, Z. Wang, Z. Liu, and L. Liu, “Effect of partial rolling on the microstructure and mechanical properties of laser-TIG hybrid welded joints of 7075-T6 aluminum alloy,” *Int. J. Adv. Manuf. Technol.*, vol. 121, no. 1–2, pp. 589–599, 2022, doi: 10.1007/s00170-022-

09287-w.

[81] P. P. Seth, O. Parkash, and D. Kumar, “Structure and mechanical behavior ofin situdeveloped Mg2Si phase in magnesium and aluminum alloys - a review,” *RSC Adv.*, vol. 10, no. 61, pp. 37327–37345, 2020, doi: 10.1039/d0ra02744h.

[82] S. Pogatscher, H. Antrekowitsch, H. Leitner, A. S. Sologubenko, and P. J. Uggowitzer, “Influence of the thermal route on the peak-aged microstructures in an Al-Mg-Si aluminum alloy,” *Scr. Mater.*, vol. 68, no. 2, pp. 158–161, 2013, doi: 10.1016/j.scriptamat.2012.10.006.

[83] R. E. R.-H. Reza Abbaschain, Lara Abbaschain, “Precipitation Hardening,” in *Physical Metallurgy Principal*, Fourth., J. D. Hilda Gowans, Ed. Stamford, USA: Cengage learning, 2009, pp. 498–520.

[84] R. Vissers, M. A. van Huis, J. Jansen, H. W. Zandbergen, C. D. Marioara, and S. J. Andersen, “The crystal structure of the β′ phase in Al-Mg-Si alloys,” *Acta Mater.*, vol. 55, no. 11, pp. 3815–3823, 2007, doi: 10.1016/j.actamat.2007.02.032.

[85] C. Chen, G. Sun, W. Du, Y. Li, C. Fan, and H. Zhang, “Influence of heat input on the appearance, microstructure and microhardness of pulsed gas metal arc welded Al alloy weldment,” *J. Mater. Res. Technol.*, vol. 21, pp. 121–130, 2022, doi: 10.1016/j.jmrt.2022.09.028.

[86] K. Poorhaydari, B. M. Patchett, and D. G. Ivey, “Estimation of cooling rate in the welding of plates with intermediate thickness,” *Weld. J. (Miami, Fla)*, vol. 84, no. 10, 2005.

[87] L. MatWeb, “Materials property data,” 2023. https://www.matweb.com/index.aspx

[88] C. M. Gómora, R. R. Ambriz, J. Zuno-Silva, and D. Jaramillo, “Heat Sink Effect on 6061 Aluminum Alloy Welds with Different Partial Aging Conditions,” *J. Mater. Eng. Perform.*, vol. 29, no. 7, pp. 4339–4350, 2020, doi: 10.1007/s11665-020-04982-9.

[89] C. Ravi and C. Wolverton, “First-principles study of crystal structure and stability of Al-Mg-Si-(Cu) precipitates,” *Acta Mater.*, vol. 52, no. 14, pp. 4213–4227, 2004, doi: 10.1016/j.actamat.2004.05.037.

[90] D. Maisonnette, M. Suery, D. Nelias, P. Chaudet, and T. Epicier, “Effects of heat treatments on the microstructure and mechanical properties of a 6061 aluminium alloy,” *Mater. Sci. Eng. A*, vol. 528, no. 6, pp. 2718–2724, 2011, doi: 10.1016/j.msea.2010.12.011.

[91] M. W. Zandbergen, A. Cerezo, and G. D. W. Smith, “Study of precipitation in Al-Mg-Si Alloys by atom probe tomography II. Influence of Cu additions,” *Acta Mater.*, vol. 101, pp. 149–158, 2015, doi: 10.1016/j.actamat.2015.08.018.

[92] I. Basori, W. D. Pratiwi, and S. T. Dwiyati, “Effect of Salt quenching on the microstructures and mechanical properties of AISI 1045 steel,” *J. Phys. Conf. Ser.*, vol. 1402, no. 5, 2019, doi: 10.1088/1742-6596/1402/5/055102.

[93] Z. Xu, Y. Zhang, Z. Xu, and Y. Zhang, “Quantification of Quench Rates in Water, Air, and Liquid Nitrogen,” *Nag*, vol. 60, p. 7345, 1999, [Online]. Available: https://ui.adsabs.harvard.edu/abs/1999nag..conf.7345X/abstract

[94] S. Pogatscher, H. Antrekowitsch, H. Leitner, T. Ebner, and P. J. Uggowitzer, “Mechanisms controlling the artificial aging of Al-Mg-Si Alloys,” *Acta Mater.*, vol. 59, no. 9, pp. 3352–3363, 2011, doi: 10.1016/j.actamat.2011.02.010.

[95] H. Wu, Q. Zhang, L. Li, M. Huang, Z. Zheng, and S. Wen, “Thermal Stability of the Precipitates in Dilute Al-Er-Zr/Hf Alloys at Elevated Temperature,” *Metals (Basel).*, vol. 12, no. 8, 2022, doi: 10.3390/met12081242.

[96] M. Cai, D. P. Field, and G. W. Lorimer, “A systematic comparison of static and dynamic ageing of two Al-Mg-Si alloys,” *Mater. Sci. Eng. A*, vol. 373, no. 1–2, pp. 65–71, 2004, doi: 10.1016/j.msea.2003.12.035.

[97] R. R. Ambriz, G. Barrera, R. García, and V. H. López, “Effect of the weld thermal cycles of the modified indirect electric arc on the mechanical properties of the AA6061-T6 alloy,” *Weld. Int.*, vol. 24, no. 4, pp. 321–328, 2010, doi: 10.1080/09507110903568778.

[98] A. Hirose, H. Todaka, H. Yamaoka, N. Kurosawa, and K. F. Kobayashi, “Quantitative evaluation of softened regions in weld heat-affected zones of 6061-T6 aluminum alloy - characterizing of the laser beam welding process,” *Metall. Mater. Trans. A Phys. Metall. Mater. Sci.*, vol. 30, no. 8, pp. 2115–2120, 1999, doi: 10.1007/s11661-999-0022-z.

[99] Y. Liang, J. Shen, S. Hu, H. Wang, and J. Pang, “Effect of TIG current on microstructural and mechanical properties of 6061-T6 aluminium alloy joints by TIG–CMT hybrid welding,” *J. Mater. Process. Technol.*, vol. 255, no. November 2017, pp. 161–174, 2018, doi: 10.1016/j.jmatprotec.2017.12.006.

[100] B. Gungor, E. Kaluc, E. Taban, and A. SIK Ş.Ş, “Mechanical and microstructural properties of robotic Cold Metal Transfer (CMT) welded 5083-H111 and 6082-T651 aluminum alloys,” *Mater. Des.*, vol. 54, pp. 207–211, 2014, doi: 10.1016/j.matdes.2013.08.018.

[101] A. Ramaswamy, S. Malarvizhi, and V. Balasubramanian, “Effect of variants of gas metal arc welding process on tensile properties of AA6061-T6 aluminium alloy joints,” *Int. J.*

Adv. Manuf. Technol., vol. 108, no. 9–10, pp. 2967–2983, 2020, doi: 10.1007/s00170-020-05602-5.

[102] E. T. Furton, A. E. Wilson-Heid, and A. M. Beese, "Effect of stress triaxiality and penny-shaped pores on tensile properties of laser powder bed fusion Ti-6Al-4V," *Addit. Manuf.*, vol. 48, no. PB, p. 102414, 2021, doi: 10.1016/j.addma.2021.102414.

[103] W. H. Kan *et al.*, "A critical review on the effects of process-induced porosity on the mechanical properties of alloys fabricated by laser powder bed fusion," *J. Mater. Sci.*, vol. 57, no. 21, pp. 9818–9865, 2022, doi: 10.1007/s10853-022-06990-7.

[104] W. H. Kan *et al.*, "The influence of porosity on Ti-6Al-4V parts fabricated by laser powder bed fusion in the pursuit of process efficiency," *Int. J. Adv. Manuf. Technol.*, vol. 119, no. 7–8, pp. 5417–5438, 2022, doi: 10.1007/s00170-021-08374-8.

[105] E. Dudrová and M. Kabátová, "Fractography of sintered steels," *Powder Metall. Prog.*, vol. 8, no. 2, pp. 59–74, 2004.

[106] R. M. N. Pelloux, "Fractography.," *NATO Conf. Ser. 6 Mater. Sci.*, vol. 5, pp. 241–251, 1983, doi: 10.31399/asm.hb.v21.a0003466.

[107] J. Bethge, H, Heydenreich, "Fractography with the SEM (Failure Analysis)," no. January, Amsterdam, 1987.

[108] A. R. Koushki, M. Goodarzi, and M. Paidar, "Influence of shielding gas on the mechanical and metallurgical properties of DP-GMA-welded 5083-H321 aluminum alloy," *Int. J. Miner. Metall. Mater.*, vol. 23, no. 12, pp. 1416–1426, 2016, doi: 10.1007/s12613-016-1365-2.

[109] C. J. Li, W. Y. Li, and H. Liao, “Examination of the critical velocity for deposition of particles in cold spraying,” *J. Therm. Spray Technol.*, vol. 15, no. 2, pp. 212–222, 2006, doi: 10.1361/105996306X108093.

[110] S. Yin *et al.*, “Deposition behavior of thermally softened copper particles in cold spraying,” *Acta Mater.*, vol. 61, no. 14, pp. 5105–5118, 2013, doi: 10.1016/j.actamat.2013.04.041.

[111] S. Pathak and G. C. Saha, “Development of sustainable cold spray coatings and 3D additive manufacturing components for repair/manufacturing applications: A critical review,” *Coatings*, vol. 7, no. 8, 2017, doi: 10.3390/coatings7080122.

[112] W. Li, C. Cao, G. Wang, F. Wang, Y. Xu, and X. Yang, “‘Cold spray +’ as a new hybrid additive manufacturing technology: a literature review,” *Sci. Technol. Weld. Join.*, vol. 24, no. 5, pp. 420–445, 2019, doi: 10.1080/13621718.2019.1603851.

[113] H. Assadi *et al.*, “On parameter selection in cold spraying,” *J. Therm. Spray Technol.*, vol. 20, no. 6, pp. 1161–1176, 2011, doi: 10.1007/s11666-011-9662-9.

[114] G. Bérubé, M. Yandouzi, A. Zúñiga, L. Ajdelsztajn, J. Villafuerte, and B. Jodoin, “Phase stability of Al-5Fe-V-Si coatings produced by cold gas dynamic spray process using rapidly solidified feedstock materials,” *J. Therm. Spray Technol.*, vol. 21, no. 2, pp. 240–254, 2012, doi: 10.1007/s11666-011-9716-z.

[115] X. J. Ning, J. H. Jang, H. J. Kim, C. J. Li, and Changhee Lee, “Cold spraying of Al-Sn binary alloy: Coating characteristics and particle bonding features,” *Surf. Coatings Technol.*, vol. 202, no. 9, pp. 1681–1687, 2008, doi: 10.1016/j.surfcoat.2007.07.026.

[116] H. Lee, H. Shin, S. Lee, and K. Ko, “Effect of gas pressure on Al coatings by cold gas

dynamic spray," *Mater. Lett.*, vol. 62, no. 10–11, pp. 1579–1581, 2008, doi: 10.1016/j.matlet.2007.09.026.

[117] X. L. Zhou, A. F. Chen, J. C. Liu, X. K. Wu, and J. S. Zhang, "Preparation of metallic coatings on polymer matrix composites by cold spray," *Surf. Coatings Technol.*, vol. 206, no. 1, pp. 132–136, 2011, doi: 10.1016/j.surfcoat.2011.07.005.

[118] N. H. Tariq *et al.*, "Cold spray additive manufacturing: A viable strategy to fabricate thick B 4 C/Al composite coatings for neutron shielding applications," *Surf. Coatings Technol.*, vol. 339, no. October 2017, pp. 224–236, 2018, doi: 10.1016/j.surfcoat.2018.02.007.

[119] J. C. Lee, H. J. Kang, W. S. Chu, and S. H. Ahn, "Repair of Damaged Mold Surface by Cold-Spray Method," *CIRP Ann. - Manuf. Technol.*, vol. 56, no. 1, pp. 577–580, 2007, doi: 10.1016/j.cirp.2007.05.138.

[120] H. Bhadeshia and R. Honeycombe, "Weld Microstructures," in *Steels: Microstructure and Properties*, 4th ed., Elsevier Ltd, 2017, pp. 377–400. doi: 10.1016/b978-0-08-100270-4.00013-5.

[121] P. Kah, R. Rajan, J. Martikainen, and R. Suoranta, "Investigation of weld defects in friction-stir welding and fusion welding of aluminium alloys," *Int. J. Mech. Mater. Eng.*, vol. 10, no. 1, 2015, doi: 10.1186/s40712-015-0053-8.

[122] P. Sahlot, A. K. Singh, V. J. Badheka, and A. Arora, "Friction Stir Welding of Copper: Numerical Modeling and Validation," *Trans. Indian Inst. Met.*, vol. 72, no. 5, pp. 1339–1347, 2019, doi: 10.1007/s12666-019-01629-9.

[123] N. Manuel, I. Galvão, R. M. Leal, J. D. Costa, and A. Loureiro, "Nugget formation and

mechanical behaviour of friction stirwelds of three dissimilar aluminum alloys," *Materials (Basel).*, vol. 13, no. 11, 2020, doi: 10.3390/ma13112664.

[124] S. Cadney, M. Brochu, P. Richer, and B. Jodoin, "Cold gas dynamic spraying as a method for freeforming and joining materials," *Surf. Coatings Technol.*, vol. 202, no. 12, pp. 2801–2806, 2008, doi: 10.1016/j.surfcoat.2007.10.010.

[125] S. L. Fu *et al.*, "Novel Method of Aluminum to Copper Bonding by Cold Spray," *J. Therm. Spray Technol.*, vol. 27, no. 4, pp. 624–640, 2018, doi: 10.1007/s11666-018-0707-1.

[126] V. Champagne *et al.*, "Dissimilar metal joining and structural repair of ZE41A-T5 cast magnesium by the cold spray (CS) process," *Mater. Manuf. Process.*, vol. 33, no. 2, pp. 130–139, 2018, doi: 10.1080/10426914.2016.1257137.

[127] Muhammad Zia ud din Urf Umer and Ahmed A. Tiamiyu, "X-ray microscopic and thermodynamic model assessments of softening in TIG welded AA 6061-T651," *Under Rev.*, 2023.

[128] K. Loke *et al.*, "Residual Stress Analysis of Cold Spray Coatings Sprayed at Angles Using Through-thickness Neutron Diffraction Measurement," *J. Therm. Spray Technol.*, vol. 30, no. 7, pp. 1810–1826, 2021, doi: 10.1007/s11666-021-01252-5.

[129] M. R. Rokni, C. A. Widener, O. C. Ozdemir, and G. A. Crawford, "Microstructure and mechanical properties of cold sprayed 6061 Al in As-sprayed and heat treated condition," *Surf. Coatings Technol.*, vol. 309, pp. 641–650, 2017, doi: 10.1016/j.surfcoat.2016.12.035.

[130] K. Hardness *et al.*, "Standard Test Methods for Vickers Hardness and Knoop Hardness of Metallic Materials BT - Standard Test Methods for Vickers Hardness and Knoop Hardness

of Metallic Materials," vol. i, pp. 1–27, 17AD, doi: 10.1520/E0092-17.2.

[131] M. S. Remøe, K. Marthinsen, I. Westermann, K. Pedersen, J. Røyset, and C. Marioara, "The effect of alloying elements on the ductility of Al-Mg-Si alloys," *Mater. Sci. Eng. A*, vol. 693, no. January, pp. 60–72, 2017, doi: 10.1016/j.msea.2017.03.078.

[132] Z. Jiang *et al.*, "Microstructure and mechanical properties of the TIG welded joints of fusion CLAM steel," *Fusion Eng. Des.*, vol. 85, no. 10–12, pp. 1903–1908, 2010, doi: 10.1016/j.fusengdes.2010.06.019.

[133] A. A. Tiamiyu, Y. Sun, K. A. Nelson, and C. A. Schuh, "Site-specific study of jetting, bonding, and local deformation during high-velocity metallic microparticle impact," *Acta Mater.*, vol. 202, pp. 159–169, 2021, doi: 10.1016/j.actamat.2020.10.057.

[134] G. Egger, P. E. Gygax, R. Glardon, and N. P. Karapatis, "Optimization of powder layer density in selective laser sintering," *10th Solid Free. Fabr. Symp.*, no. January 1999, pp. 255–263, 1999, [Online]. Available: http://infoscience.epfl.ch/record/153069

[135] A. C. Hoffmann and H. J. Finkers, "A relation for the void fraction of randomly packed particle beds," *Powder Technol.*, vol. 82, no. 2, pp. 197–203, 1995, doi: 10.1016/0032-5910(94)02910-G.

[136] A. T. Sutton, C. S. Kriewall, M. C. Leu, and J. W. Newkirk, "Powders for additive manufacturing processes: Characterization techniques and effects on part properties," *Solid Free. Fabr. 2016 Proc. 27th Annu. Int. Solid Free. Fabr. Symp. - An Addit. Manuf. Conf. SFF 2016*, pp. 1004–1030, 2016.

[137] J. Wu, H. Fang, S. Yoon, H. Kim, and C. Lee, "Measurement of particle velocity and

characterization of deposition in aluminum alloy kinetic spraying process," *Appl. Surf. Sci.*, vol. 252, no. 5, pp. 1368–1377, 2005, doi: 10.1016/j.apsusc.2005.02.108.

[138] T. H. V. Steenkiste, J. R. Smith, and R. E. Teets, "Aluminum coatings via kinetic spray with relatively large powder particles," *Surface and Coatings Technology*, vol. 154, no. 2–3. pp. 237–252, 2002. doi: 10.1016/S0257-8972(02)00018-X.

[139] F. S. da Silva, N. Cinca, S. Dosta, I. G. Cano, J. M. Guilemany, and A. V. Benedetti, "Effect of the Outer Layer of Al Coatings Deposited by Cold Gas Spray on the Microstructure, Mechanical Properties and Corrosion Resistance of the AA 7075-T6 Aluminum Alloy," *J. Therm. Spray Technol.*, vol. 29, no. 5, pp. 1040–1053, 2020, doi: 10.1007/s11666-020-01023-8.

[140] P. Gao, C. Zhang, R. Wang, G. Deng, J. Li, and L. Su, "Tamping effect during additive manufacturing of copper coating by cold spray: A comprehensive molecular dynamics study," *Addit. Manuf.*, vol. 66, no. November 2022, p. 103448, 2023, doi: 10.1016/j.addma.2023.103448.

[141] V. P. Singh, D. Kumar, R. P. Mahto, and B. Kuriachen, "Microstructural and Mechanical Behavior of Friction-Stir-Welded AA6061-T6 and AZ31 Alloys with Improved Electrochemical Corrosion," *J. Mater. Eng. Perform.*, vol. 32, no. 9, pp. 4185–4204, 2022, doi: 10.1007/s11665-022-07380-5.

[142] A. G. Gavras, D. A. Lados, V. K. Champagne, and R. J. Warren, "Effects of processing on microstructure evolution and fatigue crack growth mechanisms in cold-spray 6061 aluminum alloy," *Int. J. Fatigue*, vol. 110, no. October 2017, pp. 49–62, 2018, doi: 10.1016/j.ijfatigue.2018.01.006.

[143] K. Mutombo and M. Du Toit, “Corrosion fatigue behaviour of aluminium alloy 6061-T651 welded using fully automatic gas metal arc welding and ER5183 filler alloy,” *Int. J. Fatigue*, vol. 33, no. 12, pp. 1539–1547, 2011, doi: 10.1016/j.ijfatigue.2011.06.012.

[144] D. Boruah *et al.*, “Evaluation of residual stresses induced by cold spraying of Ti-6Al-4V on Ti-6Al-4V substrates,” *Surf. Coatings Technol.*, vol. 374, no. February, pp. 591–602, 2019, doi: 10.1016/j.surfcoat.2019.06.028.

[145] J. Li, J. Shen, S. Hu, Y. Liang, and Q. Wang, “Microstructure and mechanical properties of 6061/7N01 CMT+P joints,” *J. Mater. Process. Technol.*, vol. 264, no. April 2018, pp. 134–144, 2019, doi: 10.1016/j.jmatprotec.2018.09.011.

[146] W. Qin *et al.*, “Effects of grain size on tensile property and fracture morphology of 316L stainless steel,” *Mater. Lett.*, vol. 254, pp. 116–119, 2019, doi: 10.1016/j.matlet.2019.07.058.

[147] Y. Li, Y. Wei, X. Luo, C. Li, and N. Ma, “Correlating particle impact condition with microstructure and properties of the cold-sprayed metallic deposits,” *J. Mater. Sci. Technol.*, vol. 40, pp. 185–195, 2020, doi: 10.1016/j.jmst.2019.09.023.

[148] M. Grujicic, C. L. Zhao, W. S. DeRosset, and D. Helfritch, “Adiabatic shear instability based mechanism for particles/substrate bonding in the cold-gas dynamic-spray process,” *Mater. Des.*, vol. 25, no. 8, pp. 681–688, 2004, doi: 10.1016/j.matdes.2004.03.008.

[149] B. Jodoin, “Cold spray nozzle mach number limitation,” *J. Therm. Spray Technol.*, vol. 11, no. 4, pp. 496–507, 2002, doi: 10.1361/105996302770348628.

[150] M. Hassani-Gangaraj, D. Veysset, V. K. Champagne, K. A. Nelson, and C. A. Schuh,

"Response to Comment on 'Adiabatic shear instability is not necessary for adhesion in cold spray,'" *Scr. Mater.*, vol. 162, pp. 515–519, 2019, doi: 10.1016/j.scriptamat.2018.12.015.

Appendix

Copyright permission

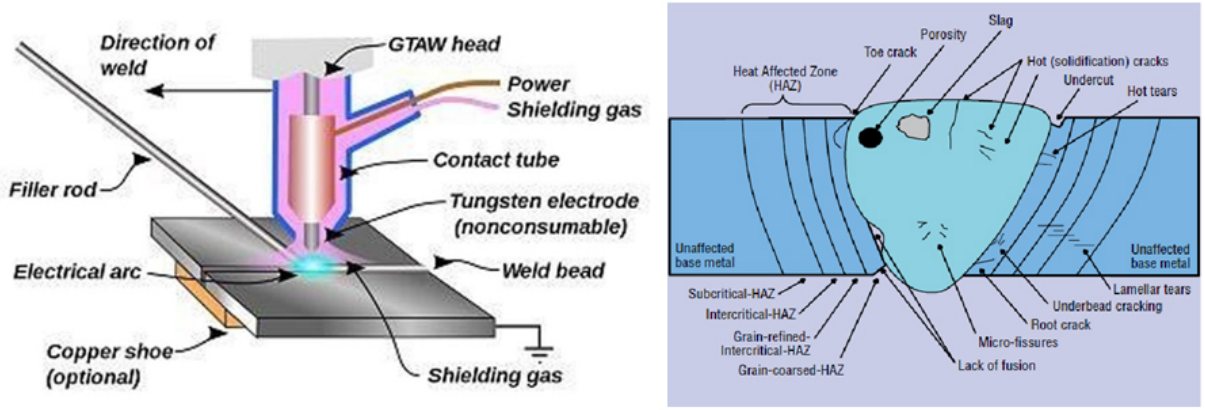

Fig. 1.1: Schematics of (a) TIG welding process), (b) common welding defects and different zones in welded components.

Fig. 1.1a reproduced from R. Kumar, N. Ramesh Mevada, S. Rathore, N. Agarwal, V. Rajput, and A. S. Barad, "Experimental Investigation and Optimization of TIG Welding Parameters on Aluminum 6061 Alloy Using Firefly Algorithm," IOP Conf. Ser. Mater. Sci. Eng., vol. 225, p. 012153, 2017, doi: 10.1088/1757-899x/225/1/012153. The publisher has a Creative Commons policy, and users can use the content with attribution.

Fig1.1b reproduced from T. Tadavi, B. Jogi, S. Dhende, S. Banait, and P. Wagh, "Microscopic Analysis of Heat Affected Zone (HAZ) of Submerged Arc Welding (saw) Joint for 1018 Mild Steel Sheet," vol. 137, pp. 194–199, 2017, doi: 10.2991/iccasp-16.2017.32. The publisher has a Creative Commons policy, and users can use the content for non-commercial purpose with attribution.

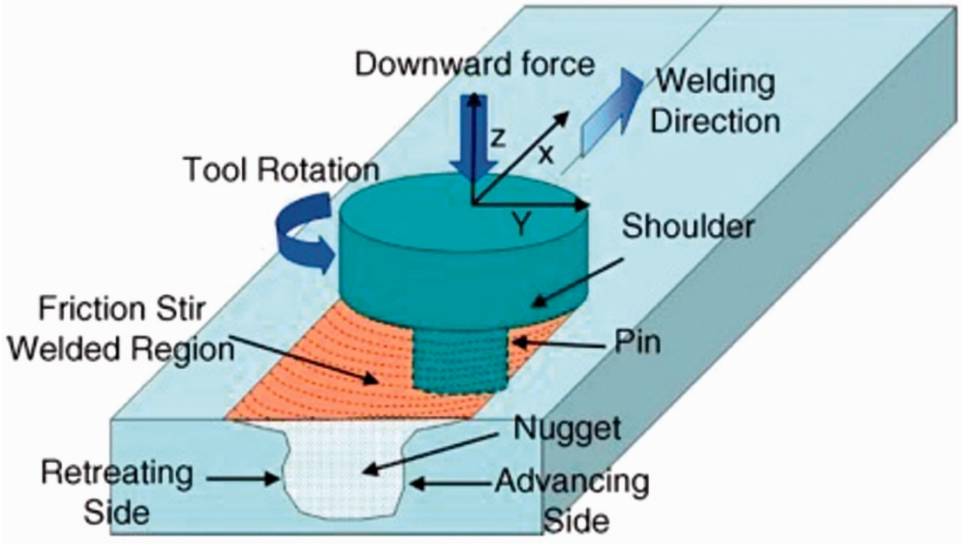

Fig. 1.2a: Schematic of friction stir welding process.

Fig 1.2a reproduced from R. S. Mishra and Z. Y. Ma, "Friction stir welding and processing," *Mater. Sci. Eng. R Reports*, vol. 50, no. 1–2, pp. 1–78, 2005, doi: 10.1016/j.mser.2005.07.001.

Copywrite permission

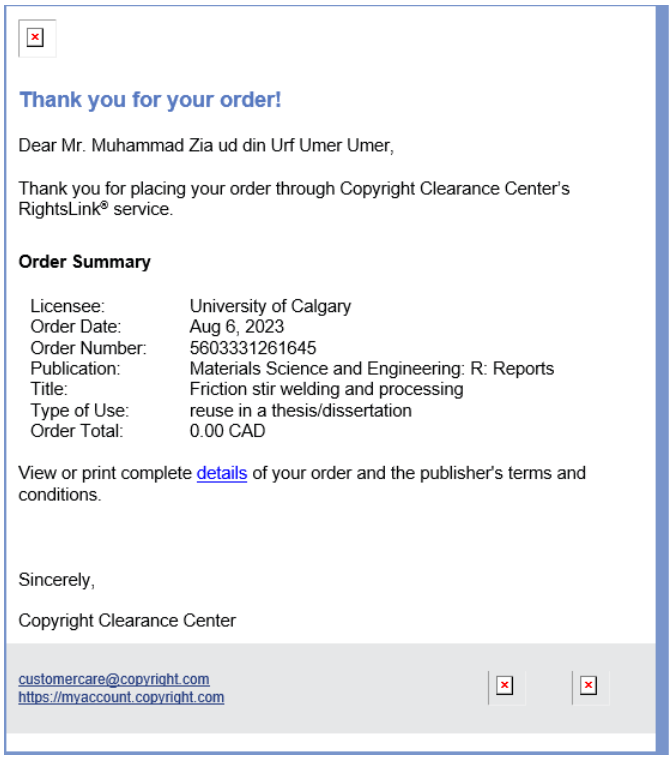

Thank you for your order!

Dear Mr. Muhammad Zia ud din Urf Umer Umer,

Thank you for placing your order through Copyright Clearance Center's RightsLink® service.

Order Summary

Licensee:	University of Calgary
Order Date:	Aug 6, 2023
Order Number:	5603331261645
Publication:	Materials Science and Engineering: R: Reports
Title:	Friction stir welding and processing
Type of Use:	reuse in a thesis/dissertation
Order Total:	0.00 CAD

View or print complete details of your order and the publisher's terms and conditions.

Sincerely,

Copyright Clearance Center

customercare@copyright.com
https://myaccount.copyright.com

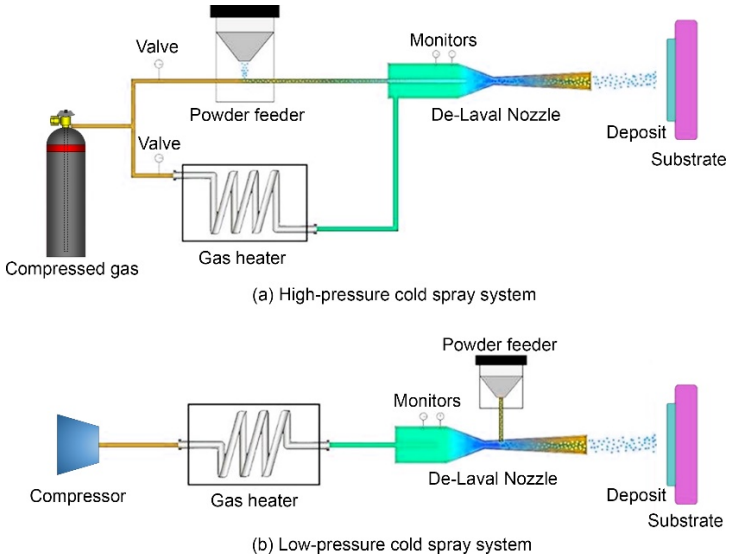

Fig.4.1: Schematic diagram of (a) high-pressure cold spray (HPCS) system, and (b) low-pressure cold spray (LPCS) system.

Fig. 1.3a and b adapted from S. Yin et al., "Cold spray additive manufacturing and repair: Fundamentals and applications," Addit. Manuf., vol. 21, no. August 2017, pp. 628–650, 2018, doi: 10.1016/j.addma.2018.04.017.

Copywrite permission

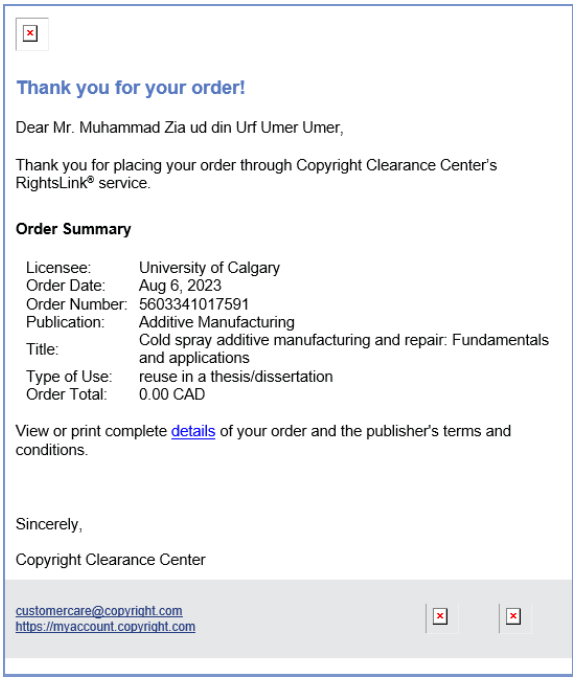

Thank you for your order!

Dear Mr. Muhammad Zia ud din Urf Umer Umer,

Thank you for placing your order through Copyright Clearance Center's RightsLink® service.

Order Summary

Licensee:	University of Calgary
Order Date:	Aug 6, 2023
Order Number:	5603341017591
Publication:	Additive Manufacturing
Title:	Cold spray additive manufacturing and repair: Fundamentals and applications
Type of Use:	reuse in a thesis/dissertation
Order Total:	0.00 CAD

View or print complete details of your order and the publisher's terms and conditions.

Sincerely,

Copyright Clearance Center

customercare@copyright.com
https://myaccount.copyright.com

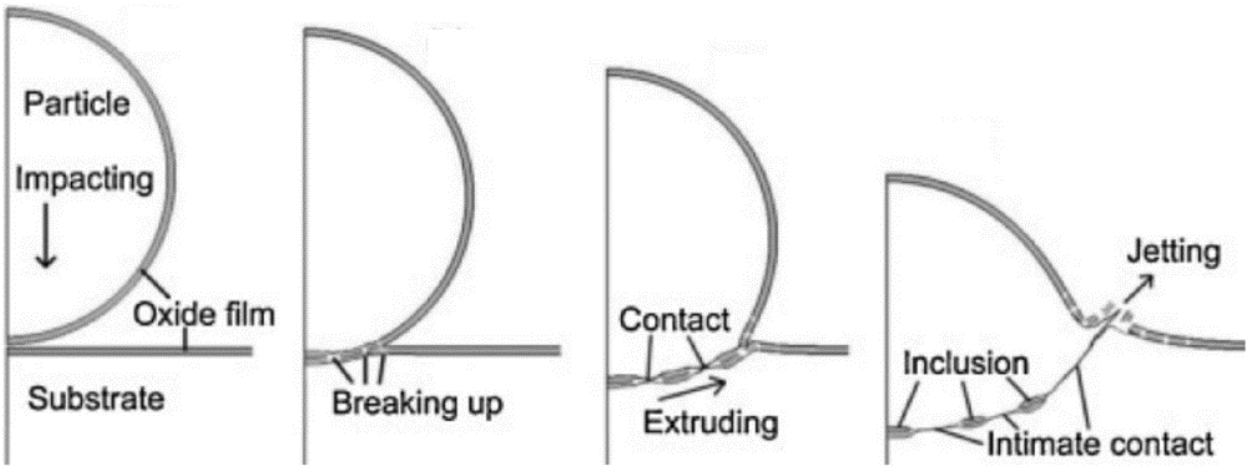

Fig. 1.4: Deformation of cold sprayed particle upon impact, and the break-up of oxide films.

Fig. 1.4 reproduced from W. Y. Li and W. Gao, "Some aspects on 3D numerical modeling of high velocity impact of particles in cold spraying by explicit finite element analysis," Appl. Surf. Sci., vol. 255, no. 18, pp. 7878–7892, 2009, doi: 10.1016/j.apsusc.2009.04.135.

Copywrite permission

Thank you for your order!

Dear Mr. Muhammad Zia ud din Urf Umer Umer,

Thank you for placing your order through Copyright Clearance Center's RightsLink® service.

Order Summary

Licensee:	University of Calgary
Order Date:	Aug 8, 2023
Order Number:	5604340946763
Publication:	Applied Surface Science
Title:	Some aspects on 3D numerical modeling of high velocity impact of particles in cold spraying by explicit finite element analysis
Type of Use:	reuse in a thesis/dissertation
Order Total:	0.00 CAD

View or print complete details of your order and the publisher's terms and conditions.

Sincerely,

Copyright Clearance Center

customercare@copyright.com
https://myaccount.copyright.com

Copyright permission status: Obtained for Fig. 1.2 and Fig. 1.3. Pending for Fig. 1.4.

Date	Article Title	Publication	Type Of Use	Price	Status	Expiration Date	Order Number
8-Aug-2023	Some aspects on 3D numerical modeling of high velocity impact of particles in cold spraying by explicit finite element analysis	Applied Surface Science	reuse in a thesis/dissertation	0.00 C$	Completed		5604340946763
6-Aug-2023	Cold spray additive manufacturing and repair: Fundamentals and applications	Additive Manufacturing	reuse in a thesis/dissertation	0.00 C$	Completed		5603341017591
6-Aug-2023	Friction stir welding and processing	Materials Science and Engineering: R: Reports	reuse in a thesis/dissertation	0.00 C$	Completed		5603331261645

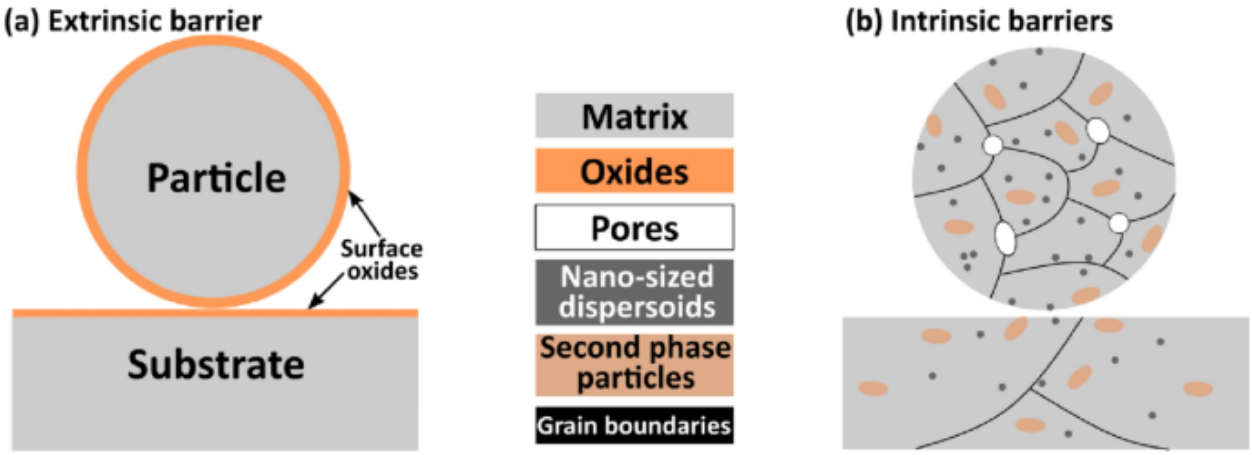

Fig. 1.5: Schematic diagrams show common (a) extrinsic and (b) intrinsic barriers to bonding during cold spray process.

Fig. 1.5 a and b reproduced from M. A. Adaan-Nyiak and A. A. Tiamiyu, "Recent advances on bonding mechanism in cold spray process: A review of single-particle impact methods," *J. Mater. Res.*, vol. 38, no. 1, pp. 69–95, 2023, doi: 10.1557/s43578-022-00764-2. The publisher has a Creative Commons policy, and users can use the content with attribution.

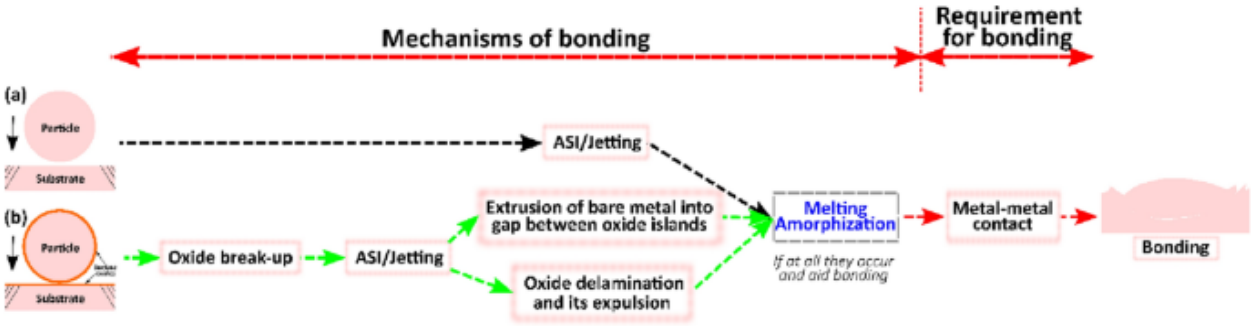

Fig. 1.6: Possible sequence of the bonding mechanism in cold spray can be illustrated through two case samples: (a) without an oxide layer and (b) with a native oxide layer.

Fig. 1.6 reproduced from M. A. Adaan-Nyiak and A. A. Tiamiyu, "Recent advances on bonding mechanism in cold spray process: A review of single-particle impact methods," J. Mater. Res., vol. 38, no. 1, pp. 69–95, 2023, doi: 10.1557/s43578-022-00764-2. The publisher has a Creative Commons policy, and users can use the content with attribution.